ALMA MATER STUDIORUM - Università di Bologna

DOTTORATO DI RICERCA IN

ASTROFISICA

Ciclo XXXIV

The J1030 field: a new window on early large scale structures and faint radio-galaxy populations

Presentata da:
Quirino D'Amato

Coordinatore di Dottorato:
Prof. **Andrea Miglio**

Supervisore:
Dr. **Isabella Prandoni**

Co-supervisore:
Prof. **Cristian Vignali**

Co-relatori:
Dr. **Roberto Gilli**
Dr. **Marcella Massardi**

Esame finale anno 2022

Settore Concorsuale: 02/C1 – ASTRONOMIA, ASTROFISICA, FISICA DELLA TERRA E DEI PIANETI
Settore Scientifico Disciplinare: FIS/05 – ASTRONOMIA E ASTROFISICA

Abstract

The formation of massive galaxies and their evolution across cosmic time is one of the key research fields of modern Astrophysics. The correlations exhibited by numerous observables in these systems are clear signatures of a tight interaction between their several components, mutually affecting their physical properties. In particular, the observed correlation between the Super Massive Black Hole (SMBH) and the host galaxy bulge masses suggests that the SMBH accretion mechanism on sub-pc scales (possibly producing an active galactic nuclei, AGN) is somewhat linked to the building process of the galaxy over much larger (kpc) scales, perhaps through so called AGN feedback, responsible for either quenching (negative feedback) or enhancing (positive feedback) star formation. In the early Universe, most of the galaxy assembly occurs in overdense regions (proto-clusters) that are going to collapse into gravitationally-bound, virialized systems (local clusters). In recent years, there has been growing evidence of a tight interaction between star formation, AGN, and the hot intra-cluster medium (ICM); in this scenario, the AGN residing in the most powerful sources, such as the proto-brightest cluster galaxy (BCG) located at the center of proto-clusters, can possibly affect the evolution of the surrounding ICM and nearby galaxies. Among distant AGN, high-redshift radio-galaxies (HzRGs) are found to be excellent BCG progenitor candidates, and hence they can be used as a proxy for proto-cluster identification up to $z \sim 4$. In these systems, the AGN radio-jets inject enormous amounts of energy in the ICM and, according to simulations, possibly promote star-formation even in the surrounding galaxies.

In this Thesis we analyze novel interferometric observations of the so-called "J1030" equatorial field, carried out with the Atacama large (sub-)millimetre array (ALMA) and the Jansky very large array (JVLA). This field (centered around the $z = 6.3$ SDSS Quasar J1030+0524) hosts two large-scale structures: *i*) one assembling around the QSO at $z = 6.3$ and *ii*) one around a powerful HzRG at $z = 1.7$. The latter presents evidence for positive AGN feedback in heating the surrounding ICM and promoting star-formation in multiple galaxies at hundreds kpc distances. The main goal of this Thesis is to exploit the new ALMA and JVLA observations to characterize the properties of the HzRG and the surrounding structure at $z = 1.7$. In addition, we exploit the JVLA observations to build one of the deepest 1.5 GHz extragalactic source samples available to date (5σ flux limit $\sim$12.5 μJy). We derive the source counts and discuss the properties of notable objects detected for the first time at radio frequencies. By exploiting the exceptional multiwavelength coverage of the J1030 field, we study the relation between the X-ray and radio emission for a sub-sample of X-ray selected AGN/galaxies, for which either a spectroscopic or photometric redshift is available, and compare it with those available in the literature in order to investigate the nature of the radio emission in these objects.

This thesis work is presented in six Chapters, as described below:

– in Chapter 1 we provide the scientific background and the state-of-art overview of AGN, AGN host galaxies, and large scale structure evolution, focusing on the properties of HzRGs in distant proto-clusters and on current evidence for positive AGN feedback.

– In Chapter 2 we provide a brief summary of the work carried out so far in the J1030 field. We report about the discovery of the QSO at $z = 6.3$ at the center of the field, where a Gunn-Peterson trough was firstly observed. We describe the subsequent wide-band multi-wavelength observational campaign undertaken in the J1030 field, thanks to which the first galaxy overdensity around a SMBH in the first billion years of the Universe was detected, along with the serendipitous discover of the $z = 1.7$ overdensity. We provide a comprehensive summary of the existing results about the $z = 1.7$ structure, obtained thanks to deep X-ray and optical/IR observations.

– In Chapter 3 we present ALMA Band 3 (Cycle 6) observations of the CO(2→1) transition of the region around the structure at $z = 1.7$, aimed at searching for new members of the galaxy overdensity. To this aim, we developed a blind-detection code that automatically finds emission lines in data-cubes on the basis of spectral, spatial and reliability criteria. We fit the spectra of three newly discovered gas-rich members of the structure, and derive their molecular gas masses ($M_{H2} \sim 1.5 - 4.8 \times 10^{10}$ $M_\odot$). Moreover, we report the detection of a large gas reservoir around the core of the HzRG ($M_{H2} \sim 2 \times 10^{11}$ $M_\odot$), showing that this source is going to evolve into the future brightest cluster galaxy. We performed a SED fitting of the HzRG host galaxy and showed that it is caught in its brief (few $\times 10^8$ yr) starburst phase, featuring a star formation rate of ~600 $M_\odot$/yr and a stellar mass of $M_* \sim 3.7 \times 10^{11}$ $M_\odot$. We derive the total mass of the structure ($\geq 3 - 6 \times 10^{13}$ $M_\odot$) and show that it is likely going to collapse into a $> 10^{14}$ $M_\odot$ cluster in the local Universe.

– In Chapter 4 we present the JVLA observations at 1.5 GHz of the J1030 field and we discuss the properties of the $z = 1.7$ HzRG, based on these new very deep radio observations. We unveil the presence of complex extended radio emission around both lobes of the HzRG, likely linked to X-ray diffuse emission spots detected in the same regions. From the analysis of the polarized emission, we show that the polarized fraction and magnetic field in both lobes of the HzRG have a morphology suggestive of a possible interaction with the external ICM, likely a signature of positive AGN feedback.

– In Chapter 5 we exploit the JVLA deep observations to extract a catalogue of 1283 extragalactic radio-sources. We estimate the catalogue completeness and reliability, and derive the source counts. We compare the source counts with those available in the literature, finding a very good agreement with recent deep wide-area surveys and recent evolutionary models. We cross-match our radio catalogue with a sub-sample of X-ray selected galaxies having photometric/spectroscopic redshifts (Nanni et al., 2018; Marchesi et al., 2021), finding 96 sources with radio-detected counterparts. Among them, fifty-six sources have spectroscopic redshift and spectral classification, allowing us to investigate the relation between the X-ray and radio emission for different types of galaxies/AGN up to $z \sim 3$. We find that X-ray sources whose radio emission is driven by nuclear activity (AGN and early-type galaxies) follow a $\log(L_R)/\log(L_X)$ linear correlation with a slope of 0.79 ± 0.12, in agreement with previous results related to low-luminosity AGN. A small number of objects (13) are spectroscopically classified as star-forming galaxies; their radio emission does not show a significant correlation with the X-ray emission, indicating that they originate from different processes: star-formation-related (radio) and AGN-related (X-ray). The rest of the sources without spectroscopic classification show no significant correlation and are likely composed by mixed populations. Finally, we find that most of the AGN-driven radio-sources (~80%) show a radio-to-X-ray radio-loudness $\log(L_R/L_X) \lesssim -3.5$, which classifies these objects as radio-quiet AGN. We also report about the detection in the radio band of some notable sources: *i*) the QSO at $z = 6.3$ at the center of the J1030 field, which is the faintest $z > 6$ radio-quiet AGN detected so far; *ii*) two gas-rich members of the $z = 1.7$ structure, located at a projected distance of ~80 kpc from the HzRG core; *iii*) a candidate obscured AGN at $z > 5.7$.

– In Chapter 6 we provide a summary of the work, highlighting the main results, conclusions, and future perspectives for deep radio surveys.

Throughout this work we adopt a concordance ΛCDM cosmology with $H_0 = 70$ km s^{-1} Mpc^{-1}, $\Omega_M = 0.3$, and $\Omega_\Lambda = 0.7$, in agreement with the *Planck 2015* results (Planck Collaboration et al., 2016). The angular scale and luminosity distance at z=1.7 are 8.46 kpc/arcsec and 12.7 Gpc, respectively.

Contents

Contents i

1 Scientific background **1**

1.1 Active Galactic Nuclei . . . 1

1.1.1 Main AGN components and the Unified Models Paradigm . . . 1

1.1.2 Broad-band AGN emission . . . 3

1.1.3 Type I and Type II AGN . . . 7

1.1.4 High-Excitation and Low-Excitation AGN . . . 8

1.1.5 Radio Loudness . . . 9

1.1.6 Radio-loud AGN: morphology and accretion mechanism . . . 10

1.1.7 The origin of radio emission in RQ AGN . . . 11

1.1.8 AGN radio – X-ray luminosity correlations . . . 13

1.2 The AGN – host galaxy connection . . . 14

1.2.1 Molecular gas properties . . . 15

1.2.2 Dust properties . . . 17

1.2.3 The role of the host galaxy in AGN obscuration . . . 18

1.3 The role of AGN feedback in galaxy evolution . . . 20

1.3.1 Proto-clusters: the cradles of galaxy assembly . . . 21

1.3.2 High-z powerful radio-galaxies . . . 23

1.3.3 Large-scale feedback of HzRGs . . . 24

2 The J1030 equatorial field: the benefits of the bias **28**

2.1 The $z = 1.7$ HzRG in the J1030 field . . . 31

2.2 The $z = 1.7$ HzRG associated overdensity . . . 34

2.2.1 Origin of the diffuse X-ray emission . . . 36

2.2.2 HzRG-induced feedback on multiple galaxies . . . 38

3 The ALMA view of the the $z = 1.7$ overdensity: evidence for a massive proto-cluster assembly **40**

3.1 ALMA observations and calibration 40
3.2 Image cube analysis 41
3.2.1 Line imaging 41
3.2.2 Noise and S/N cubes 41
3.2.3 Source detection 42
3.2.4 Spectral analysis and moments 43
3.2.5 The molecular gas properties of the overdensity members 46
3.2.6 Proto-cluster mass and evolution 50
3.3 A proto-BCG caught at the peak of its stellar mass building 52
3.3.1 Broadband Optical/IR photometry 52
3.3.2 ALMA continuum emission 52
3.3.3 SED fitting of the proto-BGC 53
3.3.4 Origin of the continuum emission at 3.3 mm 56

4 The 1.5 GHz observations of the $z = 1.7$ HzRG: evidence for large scale feedback 57
4.1 JVLA observations and calibration of the J1030 field 57
4.1.1 Total intensity calibration and imaging 57
4.1.2 Polarized emission calibration and fractional polarization imaging 58
4.2 The $z = 1.7$ HzRG: radio–continuum properties 61
4.3 The $z = 1.7$ HzRG polarization properties: signatures of AGN feedback? . 63

5 The J1030 JVLA field: a legacy for the future 66
5.1 The JVLA field 66
5.1.1 Time and bandwidth smearing 67
5.2 Source detection and catalogue extraction 67
5.2.1 Catalogue Reliability 69
5.2.2 Catalogue completeness 69
5.3 Final source catalogue 71
5.3.1 Flux scale 72
5.3.2 Source Sizes 72
5.4 Systematic effects 73
5.4.1 Resolution bias 73
5.4.2 Eddington bias 76
5.5 Source counts 77
5.6 Notable sources 79
5.6.1 SDSS J1030+0524 QSO at $z = 6.3$ 79

5.6.2 Radio-detected $z = 1.7$ proto-cluster members 81
5.6.3 An obscured AGN candidate at cosmic dawn 82
5.7 Radio-X-ray luminosity relation 82

6 Conclusions and future perspectives 88
6.1 Summary and conclusions 88
6.2 Future perspectives of deep radio surveys 93
6.2.1 Obscured AGN at the cosmic dawn 94
6.2.2 Deep radio surveys as probes of the distant proto-cluster population 94

Bibliography 96

Chapter 1

Scientific background

1.1 Active Galactic Nuclei

Active Galactic Nuclei (AGN) are the shiniest and one of the most complex mechanisms that contribute to the global galaxy-system assembly; their inner compact region, constituted by various sub-components, hosts the central super massive black hole (SMBH) accretion process that powers AGN emission over about twenty decades in frequency. AGN radiation is detected in approximately 1% – 10% of all galaxies, showing different continuum and line emission features depending on the observational band (see § 1.1.2). The AGN structure is concentrated within few tens of parsec, and is difficult to be directly probed due to current observational limitations both in terms of angular resolution and sensitivity. Huge steps forward have been made in the last 5-10 years thanks to Very Long Baseline Interferometry (VLBI) observations, including those that detected for the first time the SMBH shadow at the center of the M87 galaxy (Event Horizon Telescope Collaboration et al., 2019). However, to date there is not a unique model that perfectly describes the central engine and its surrounding regions in all of their physical and observational aspects.

1.1.1 Main AGN components and the Unified Models Paradigm

The most widely accepted AGN paradigms are known as "Unified Models" and postulate that nuclear absorption is due to a parsec-scale medium distributed in a toroidal geometry around the central engine (Antonucci, 1993; Urry & Padovani, 1995). These models predict the presence of at least the following components at the center of galaxies:

– **SMBH**: it is the central massive object that accretes matter from a surrounding disk. Its mass typically ranges from 10^6 and $10^9 M_\odot$ and is concentrated within a region defined by the Gravitational radius r_g which is directly proportional to the BH mass M_{BH}: $r_g = GM_{BH}/c^2$ where G is the gravitational constant and c is the speed of light. The efficiency of the accretion process in converting the gravitational energy into radiation defined as $\eta = L/(M_{\odot}\, c^2)$, where L is the AGN bolometric luminosity. The luminosity of the accretion process is often expressed in terms of the Eddington ratio $\lambda = L/L_{edd}$, where $L_{edd} \simeq 1.5 \times 10^{38}(M_{BH}/M_{\odot})$ erg s^{-1} is the Eddington luminosity, that is the expected radiation at the equilibrium between the gravitational and radiative forces, above which the radiation pressure overwhelms gravity. Typical values of η and λ are in the range 0.06 – 0.4 and 0.01 – 0.1, respectively.

– **Accretion disk**: the accretion onto the BH converts the gravitational energy into radiation, heating the material in a dissipative and viscous accretion disk, distributed in a structure rotating at Keplerian velocities around the SMBH at typical distances of 10^{-6} – 10^{-3} pc. The most commonly assumed model consists of an optically thick and geometrically thin disk with high-efficiency (Shakura & Sunyaev, 1973), where the disk features a gradient of density and temperature rising from the outer to the inner regions. However, a different optically thin geometrically thick accretion disk model (advection–dominated accretion flow, ADAF; Ichimaru, 1977) has been proposed to explain the low-luminosity (low-efficiency) accretion process observed in some AGN, possibly related to the presence of the radio-jets (see jets' description in the following).

– **Hot corona (electron plasma)**: it is thought to be a very hot ($T \sim 10^{8-9}$ K), extremely dense ($n \sim 10^8$ cm^{-3}) and highly ionized gas component extended up to $\sim$10 r_G in proximity of the accretion disk, possibly distributed in a clumpy optically thin structure (Fabian et al., 2015). The formation mechanism of the hot corona is mostly debated, possibly ascribed to either expansion of the accretion disk outer layers (Netzer, 2013) or to instabilities in weakly magnetized accretion flows (Di Matteo et al., 2000).

– **Broad Line Region (BLR) and Narrow line region (NLR)**: these regions correspond to the largest scale structures in AGN where the central emission can still ionize and excite the medium. The innermost BLR (0.1 – 1 pc from the SMBH) is characterized by the emission of broad ($\Delta v = 10^{3-4}$ km/s) permitted lines and is composed by warm ($T \sim 10^4$ K) and extremely dense ($n \sim 10^{9-10}$ cm^{-3}) clouds (Peterson, 1997). The NLR can extend up to few hundreds of parsecs and is composed by gas with lower density ($n \sim 10^4$ cm^{-3}) than the BLR, which allows forbidden transitions to occur. The NLR is distributed in a axisymmetrical double opposite cones' shape with respect to the SMBH.

– **Torus (dusty absorber)**: this component is thought to be the main responsible of the central emission obscuration within the Unified Models frame, at the basis of the Type I/Type II dichotomy that is explained in terms of different inclination angle with respect to the line of sight (see § 1.1.3 for more details). It is mainly composed by warm dust (up to few × 100 K) that absorbs the outgoing optical and X-ray radiation and thermally re–emits in the infrared (IR) band, peaking at ~10–20 μm (Pier & Krolik, 1992, 1993). It is co-spatial with an atomic and molecular gas ($n \sim 10^{4-7}$ cm^{-3}) component rotating at velocity of $\sim 10^3$ km/s, and is approximately distributed in a clumpy structure with clouds of variable size, as argued in the last two decades from time variability and high-resolution IR observations (Haas, 2003; Jaffe, Marsh & Tokunaga, 2004; Risaliti, 2008; Stalevski et al., 2012; Burtscher et al., 2013). The formation mechanism of the torus is still debated, it may be assembled through accretion disk outflows (Gallagher et al., 2013) or may be the result of material ejected from nearby Supernovae (Schartmann et al., 2009).

– **Jets**: these are the largest visible structures directly associated to AGN activity and are mostly observed to shine in the radio-band. Their radio emission is synchrotron radiation from relativistic electrons spiralling in the source magnetic field (see § 1.1.2 and § 1.1.6). Radio jets extend from the innermost region close to the SMBH, where they originate, up to hundreds of kpc or even few Mpc into the external environment that surrounds the host galaxy. Large-scale radio jets are observed only in a fraction of so called 'radio-loud' (RL) AGN. Non-jetted AGN are usually referred to as 'radio-quiet' (RQ) AGN (for more details on the RL/RQ AGN classification we refer to § 1.1.5).

The main AGN components described above are represented in the schematic view of the Unified Models paradigm reported in Fig. 1.1, which postulates that AGN are axis-symmetric systems, with the accretion disk and the obscuring material being aligned on the equatorial plane. Radio jets, when present, are aligned along the main axis of the system.

Understanding each of the complex AGN physical components is a challenge *per se*, as they are responsible of a large variety of observational features, which can be traced back to different emission mechanisms. In the following we provide an overview of the main AGN features across the various observing bands.

1.1.2 Broad-band AGN emission

The AGN emission arises from various mechanisms which are preferentially observed in different regions of the electro-magnetic spectrum, from the γ–rays to the radio-band. In Fig. 1.2 we show the Spectral Energy Distribution (SED) of AGN across the observable frequency range (top panel), as well as the typical X-ray spectrum with the main emission components (central panel), and several IR-SED for different grades of obscuration (bottom panel). The shape of the emission in each band can significantly differ due to either intrinsic source characteristics or orientation with respect to the line of sight, that determines the level of obscuration and hence the AGN classification. In the following we report a brief description of the spectral properties in each band:

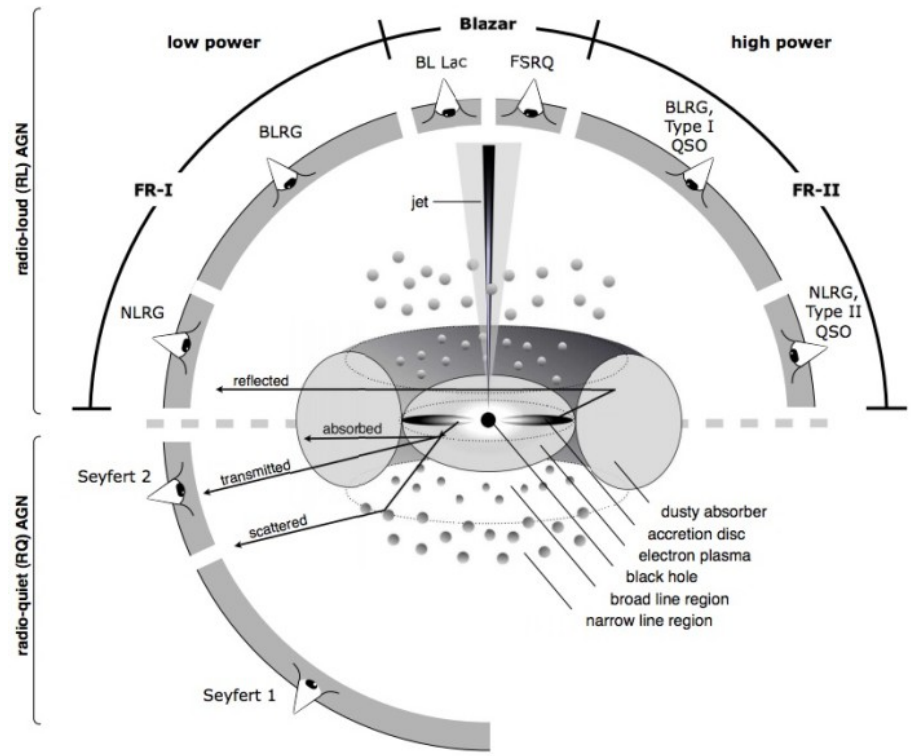

Figure 1.1: Schematic representation of the Unified Models paradigm, where the principal components of the AGN are indicated. The various types of AGN result from different orientation angles with respect to the line of sight. Image adapted from Beckmann & Shrader (2012).

– **X-rays**: this is the best-suited band to investigate the physics of the innermost part of the central engine. The primary X-ray emission mechanism is thought to be associated with optical/ultra-violet (UV) photons originated in the accretion disk, being scattered by the hot-corona electrons via inverse Compton (IC) process. The IC photons energy distribution is described by a power-law $N(E) = N_0 E^{-\Gamma}$, where Γ is the so-called photon index. Typical values of Γ are in the range 1.8 – 2.0 (Piconcelli et al., 2005). Other two main X-ray components are the so-called soft excess peaking in the 0.2 – 2 keV energy range and the reflection hump peaking in the 20 – 30 keV range (showing a high-energy cut-off at ~200 keV), respectively. The origin of the soft excess is still debated; formerly believed to be the high-energy tail of the accretion disk thermal emission, it may arise also from blurred reflection by the disk of the hot-corona X-ray photons or due to a "warm corona" Comptonization (Petrucci et al., 2018). The reflection hump, instead, is produced by reprocessed photons directed back to the disk from the hot corona. Another important feature observable in the X-ray band is the iron Kα line emission at the rest-frame energy 6.4 keV, occurring from the fluorescence induced in iron atoms by the ejection of one electron in the K-shell ($n = 1$), as a result of the photo-electric absorption of one photon originated in the hot corona. The energy threshold of the absorption is 7.1 keV, which produces a prominent drop-out in the reflection hump called absorption edge (see Risaliti & Elvis, 2004). The emission components in a typical AGN X-ray spectrum are better identified in the central panel of Fig. 1.2. The X-ray spectrum shape can be strongly affected by obscuration, which is produced by the metals photo-electric absorption at low energies ($\lesssim$10 keV) and by Compton scattering at high energies ($\gtrsim$10 keV), and that is parameterized in terms of column density N_H. The main observable obscuration features are the suppression of the soft-band emission and the enhancement of the iron Kα Equivalent Width (i.e. a measure of the line emission against the continuum). Typical widely-used obscuration classification criteria divide obscured AGN in three regimes: unabsorbed ($\log(N_H/\mathrm{cm}^2) < 21$), Compton-thin ($21 < (\log N_H/\mathrm{cm}^2) < 24$) and Compton-thick ($\log(N_H/\mathrm{cm}^2) > 24$, considered "heavily" obscured if $\log(N_H/\mathrm{cm}^2) > 25$).

- **Optical-UV**: these bands are largely dominated by the thermal component originating from the accretion disk, usually referred to as "Big-Blue Bump" (BBB). The BBB dominates the overall emission of un-obscured AGN where the accretion disk is directly observable. Thanks to the numerous emission lines observable in these bands, the Optical-UV Spectrum is an extraordinary tool to investigate the physical properties of the innermost AGN regions, especially in un-obscured AGN, where the BLR is directly probed.

- **Mid-Infrared**: The mid-infrared (MIR) radiation is particularly prominent in obscured AGN, as the dusty-torus reprocessed emission of the UV-light coming from the accretion disk emits as a thermal component peaking at $\sim$10 – 20 μm. In addition obscured AGN show absorption features due to dust complex compounds such as silicates. (see bottom panels of Fig. 1.2).

- **Radio**: RL AGN show strong emission at MHz – GHz frequencies associated with synchrotron radiation. This implies the existence of relativistic particles immersed in a magnetic field. These electrons are accelerated through the ejection of plasma in the region near the SMBH, resulting in relativistic jets. For a given ensemble of particles following a non-thermal energy distribution described by a power-law $N(E) \propto E^{-\delta}$, the total flux density resulting from the superimposition of each particle emission is a function of the magnetic field B and observed frequency ν: $S_\nu \propto B^{\alpha+1}\nu^{-\alpha}$, where $\alpha = (\delta - 1)/2$ is the radio spectral index. Such synchrotron emission is self-absorbed at low frequencies where the optical depth strongly increases ($\tau \gg 1$), and the flux density can be written as $S_\nu \propto B^{-1/2}\nu^{5/2}$. Nuclear emission (corresponding to the jet base region in AGN) shows a nearly flat (α~0) spectrum, while the spectral index increases along the jet with typical values of ~0.6 and reaches values around 0.7-0.8 at the bright end (Giovannini et al., 1998, 2001). This is consistent with partially optically-thick (self-absorbed) synchrotron emission in the core, and optically-thin synchrotron emission in the jets. The spec-

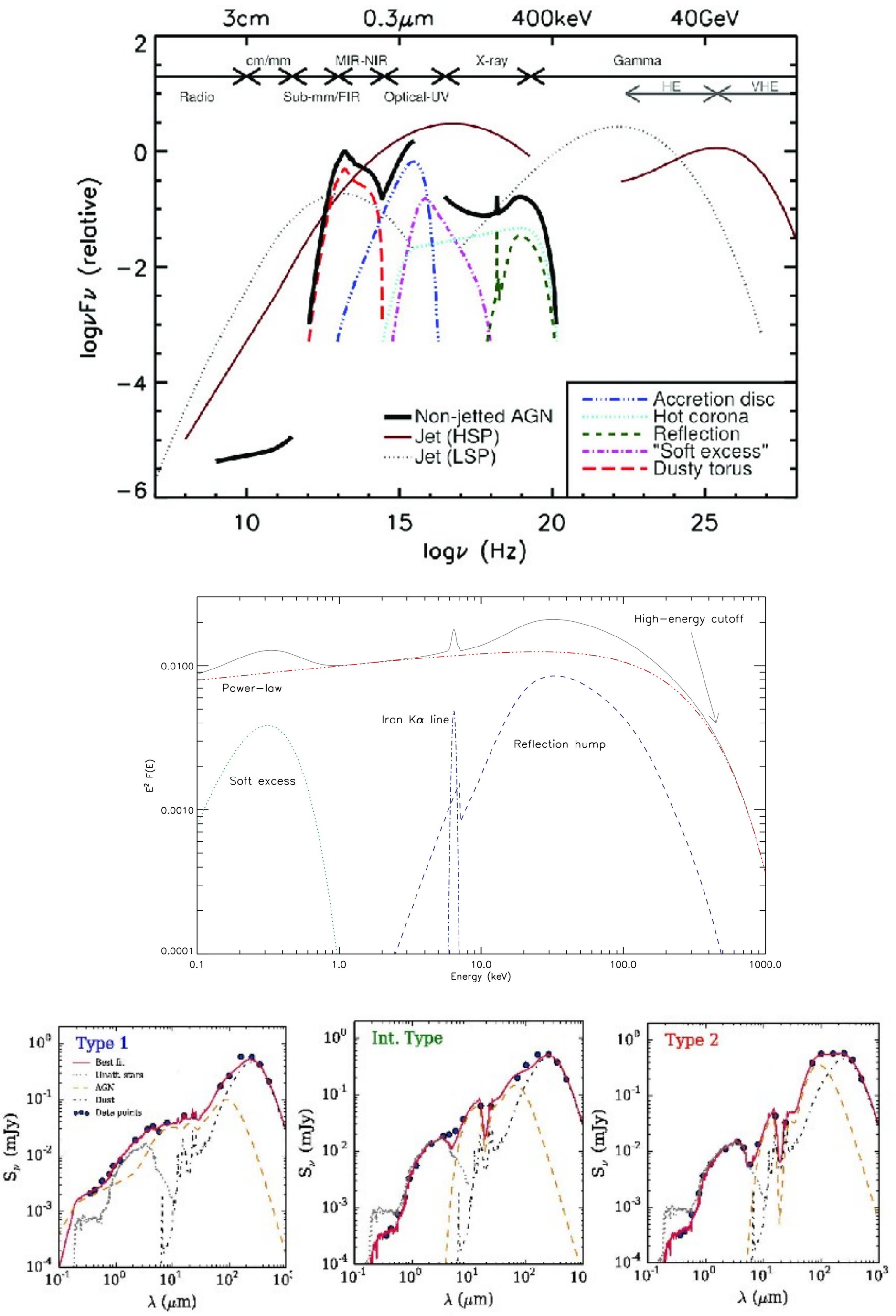

Figure 1.2: *Top*: a schematic view of the spectral energy distribution of AGN, showing the emission of the various components as labeled. The black solid curve represents the total emission of "non-jetted" AGN, while the "jetted" emission is reported for the HSP and LSP Blazar subclasses (see § 1.1.5). From Padovani et al. (2017), adapted from Harrison (2014). *Center:* X-rays spectrum of an AGN with labeled main components presented in the text (image taken from http://www.isdc.unige.ch/~ricci/Website/AGN_in_the_X-ray_band.html). *Bottom:* Examples of AGN mock SED in the IR band, for Type I, intermediate Type and Type II classes (left to right, blue points), and best fits obtained by Code Investigating GALaxy Emission (CIGALE Noll et al., 2009). The main components of the IR emission are also reported. Adapted from Ciesla et al. (2015).

tral index is directly linked to the ageing of the electrons population, since they lose energy through mechanical and radiative processes, shifting the population to lower energy and causing δ (and then, α) to increase at higher frequencies. Finally, we recall that the radio-emission in AGN is often (linearly) polarized due to the synchrotron nature. The maximum intrinsic fractional polarization (i.e., the ratio between the polarized emission and the total intensity) is inherently dependent on the energy distribution of the electron population, being $(3\delta + 3)/(3\delta + 7)$ (Laing, 1980). Typical values of the fractional polarization are few percents (e.g., Stockman & Angel, 1978).

– **γ–rays**: Gamma-ray emission is observed only in RL AGN. This band is dominated by photons originally produced as part of the synchrotron radiation of the relativistic jets, that have been scattered to higher energy via the Inverse Compton (IC) radiative process. When the synchrotron photons produced by the jets experience an energy boosting through scattering against the same jet particles (Self Synchrotron Compton, SSC), the IC emission is described by a power-law with the same spectral index of the synchrotron emission, and is characterized by a high-energy cut-off corresponding to the maximum energy reached by the scattered photons. A clear signature of SSC is observed in Blazars (see § 1.1.3), the most powerful γ–ray sources, and is represented by a "double–peaked" spectral feature characterised by two distinct peaks in the radio (synchrotron) and γ–ray (SSC) bands. However, the up-scattered photons may also be originated elsewhere, such as the BLR and torus (external Compton, EC). Depending on the position and relative intensity of the radio and γ–ray peaks, Blazars are divided into High Synchrotron Peaked (HSP) and Low Synchrotron Peaked (LSP). The jet-dominated emission of these two subclasses is shown in Fig. 1.2 (top panel), by the solid brown and dotted black lines for HSP and LSP, respectively.

During the past decades the observed variety of AGN spectral features led to the classification of these objects in a wide number of classes (based on the intensity in a given band, morphology, etc.). We stress, however, that this classification is only partially related to physical differences, as it mainly results from the selection criteria adopted, and/or from the observational band considered. In the following we provide an overview of the main AGN classes and of their key characteristics.

1.1.3 Type I and Type II AGN

A major classification of AGN divides them in two main categories, named Type I and Type II, and postulates that the observed differences between them are due to the way the axis-symmetric system is oriented with respect to the line of sight (Unified Models, Antonucci, 1993). In particular, when the central region is seen through the obscuring torus due to an edge-on orientation we have a Type II AGN; when the system is observed face-on, and the the central region can be directly observed, we have a Type I AGN. According to this dichotomy, a major classification of local AGN that show strong high-ionization emission lines in their optical spectra, originally presented by Seyfert (1943), divides these objects in Seyfert 1, characterized by narrow and broad permitted emission lines, and Seyfert 2 which show narrow lines only. In addition, the continuum of Seyfert 2 is more depressed with respect to Seyfert 1, especially at short wavelengths, indicating dust extinction. According to the Unified Models, Seyfert 1 systems are observed at a small angle from the main axis, and hence both BLR and NLR are visible; Seyfert 2 systems are seen at a larger angle and partially obscured by the dust torus. Hence only the NLR is visible. Based on the aforementioned spectral properties, Type I and Type II AGN are also referred to as Broad Line (BL) and Narrow Line (NL) AGN respectively.

Another well-known class of bright AGN is represented by Quasars (or Quasi-Stellar Objects, QSOs). These objects are considered to be the more luminous counterparts of Seyfert galaxies and share with them the dual Type I/Type II classification with analogous spectral features and physical properties of the central engine. Historically, the separation between QSOs and Seyfert galaxies mainly involved the optical magnitude, with varying separation values found in literature.

A similar distinction exists for RL (or jetted) AGN, which are classified into Broad Line Radio Galaxies (BLRG) or Narrow Line Radio Galaxies (NLRG). In addition, RL AGN with radio jets pointing directly in the direction of the observer and characterized by short time–scale variability (hours/days) are known as Blazars, and constitute the most powerful class of objects. As mentioned above, they show a double–peaked spectrum that extends from the radio to the γ–rays bands (see § 1.1.2). Blazars are divided in two main sub–classes: BL Lacs, with weak or absent broad emission lines (typically belonging to the HSP class), and Flat Spectrum Radio Quasars (FSRQ), with strong broad emission lines (typically belonging to the LSP class).

1.1.4 High-Excitation and Low-Excitation AGN

An important AGN classification refers to the black-hole accretion mechanism occurring in these objects. In this case the classification is based on the presence/lack of high-excitation emission lines in the AGN optical spectra (e.g., Baldwin, Phillips & Terlevich, 1981; Veilleux & Osterbrock, 1987), and is related to the efficiency of the accretion process. In so-called high-excitation AGN (Seyfert galaxies and QSO) the SMBH is thought to be fed by a radiative efficient mechanism (through a geometrically thin and optically thick accretion disk; Shakura & Sunyaev 1973), whereas low-excitation AGN are associated with a radiative inefficient accretion process (through e.g. an Advection Dominated Accretion Flow, or ADAF; Narayan & Yi e.g. 1994). The switch between the two regimes happens when the Eddington ratio drops below a certain threshold ($L/L_{edd} \approx 0.01$; Rees et al., 1982; Heckman & Best, 2014). Generally, efficiently accreting systems also show high X-ray luminosities ($> 10^{42}$ erg s^{-1}), while inefficient accretors are often RL AGN (i.e. the only manifestation of the presence of an accreting SMBH is through the production of relativistic jets).

1.1.5 Radio Loudness

Another main classification of AGN is the one that divides them into RL and RQ AGN. This is done on the basis of their "radio loudness": the definition of this parameter significantly varies in the literature and relies either on the intensity of the radio emission (e.g., Peacock, Miller & Longair, 1986) or on the emission ratio between the radio and another band (Schmidt, 1970). Two widely used radio loudness definitions are the ones those using either the optical flux ($R_O = f_{5\,\mathrm{GHz}}/f_{4400\,\text{Å}} = 10$, Kellermann et al., 1989; Jiang et al., 2007) or the X-ray luminosity ($R_X = \log(L_{radio}/L_X) = -3.5\,/\,-4$, Terashima & Wilson, 2003). A more general parameterization of the radio loudness has been proposed by Baloković et al. (2012) as $R_K = \log(L_{radio}) - K\log(L_\lambda)$, where $\log(L_{radio})$ is the radio luminosity measured at frequencies $\sim 1-6$ GHz and $\log(L_\lambda)$ is the luminosity measured in another band, for instance X-ray or optical. In this case, by setting $K = 0$ a simple radio luminosity threshold is assumed; if instead $K = 1$ the classification is based on the luminosity ratio between two bands. It is worth mentioning that obscuration can play a role in the determination of radio loudness, and thus in the classification of RL AGN. Padovani (2011) and Bonzini et al. (2013) pointed out that, despite the many definitions available in literature, the radio loudness criterion can be applied only to Type I AGN, since in Type II AGN obscuration can strongly affect the bands usually adopted to estimate the radio loudness, such as the optical or X-ray bands. Lambrides et al. (2020) exploited the broad-band coverage and exceptional depth of the Chandra Deep Field South (CDF-S) field to investigate the low-luminosity population of X-ray selected AGN, finding that they appear as faint X-ray emitters due to the obscuration, while they show from moderate to powerful emission in the IR and radio bands; this observational bias leads to the misclassification of these objects as RL AGN and to an overestimate of the RL AGN fraction in the AGN population (see Fig. 1.3). This is especially important at high-redshifts, where the obscured AGN fraction increases (Vito et al., 2016, 2018, see also § 1.2.3), and considering that there is strong observational evidence that a portion of the population of obscured AGN is being missed by existing X-ray surveys (Gilli, Comastri & Hasinger, 2007).

Recently, Padovani (2016, 2017) proposed to substitute the classification of AGN on the basis of radio-loudness with a new "jetted/non-jetted" classification, arguing that RL and RQ AGN represent two intrinsically different types of radio sources: RL AGN feature powerful relativistic jets up to Mpc scales (see § 1.1.1, § 1.1.2 and Fig: 1.2), while RQ AGN do not show the presence of strong relativistic radio-jets and their radio emission is likely dominated by other processes (Padovani et al., 2017). The issue of the origin of radio emission in RQ AGN will be further discussed in in § 1.1.7.

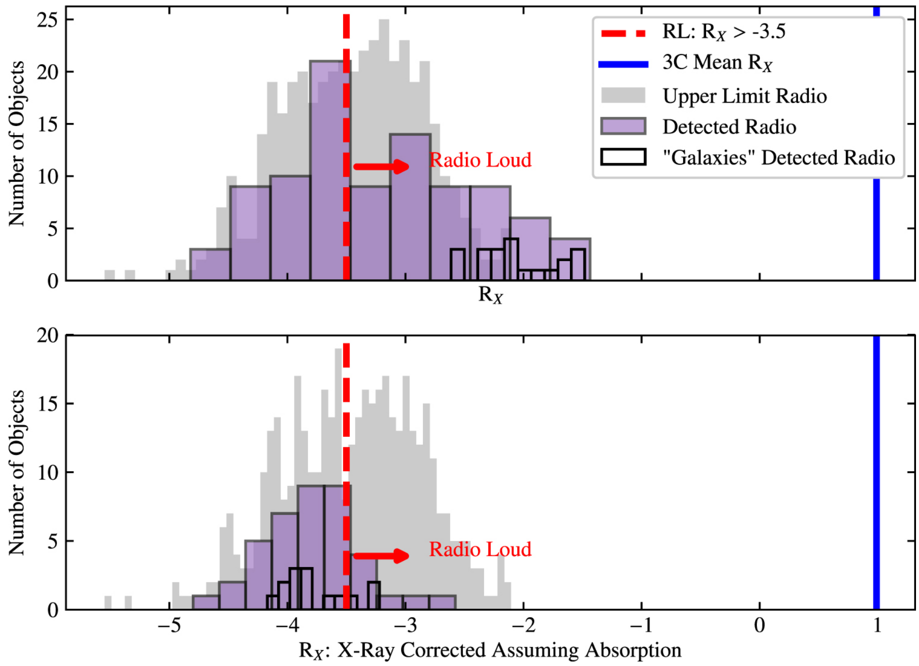

Figure 1.3: *Top*: observed Radio/X-ray radio-loudness (R_X) distribution for a sample of X-ray-selected obscured AGN (violet histogram). The grey histogram represents upper limits. The black open histogram is the distribution for X-ray detected galaxies at $z > 0.5$, originally classified as normal galaxies. The vertical red dashed line marks the RQ/RL AGN threshold defined by Terashima & Wilson (2003), while the blue solid line shows the mean value for a sample of bright bona-fide RL sources. *Bottom*: same R_X distribution after correcting the X-ray luminosity for the obscuration, showing that a large fraction of the sample was misclassified as RL AGN and normal galaxies. From Lambrides et al. (2020).

1.1.6 Radio-loud AGN: morphology and accretion mechanism

As discussed above, RL AGN have their emission in the radio-band largely dominated by nuclear activity. Their major morphological feature is the presence of bright jets, arising in the vicinity (< few pc) of the central SMBH and extending up to Mpc scale out of the host galaxy, and formed by a relativistic ($\beta = v/c \sim 0.5 - 0.9$; Giovannini et al., 2001) and collimated stream of electrons. The jet formation mechanism is still unclear and is likely related to the properties of the magnetic field (in terms of strength and spatial configuration) in the innermost regions, where the gas is accelerated and pushed away (e.g., Lynden-Bell, 1996; Ohsuga & Mineshige, 2011). Radio galaxies (RG) are often classified based on their radio morphology. A widely used classification is the one proposed by Fanaroff & Riley (1974), and divides RGs into FR I and FR II morphological types: FRII RGs (also known as edge-dominated) have powerful relativistic jets that reach maximum brightness in the so-called hot-spots, where the jets possibly interact with the external medium. If jet axis is not parallel to the sky plane, the approaching jet with respect to the line of sight benefits from relativistic boosting and appears brighter than the receding one (counter-jet). FRI RGs, instead, have core-dominated emission; their jets often feature an irregular shape and are brighter in the inner regions. In Fig 1.4 two examples of FR I and a FR II RGs are shown. Historically this morphological classification was considered to be connected with the source radio luminosity (or jet power), with low power ($L_{178\ \mathrm{kHz}} < 10^{25}$ W/Hz) RGs tending to be FR I and high-power ($L_{178\ \mathrm{kHz}} > 10^{25}$ W/Hz) RGs tending to be FR II. Nowadays the relation between radio power and morphology appears more complex, with deep radio surveys showing an increasing number of low-power FR II RGs, and clear evidence that other parameters (e.g. the host galaxy stellar mass and/or the environment) may be the primary drivers for the observed morphologies (see e.g. Mingo et al., 2019).

Another, more physically motivated, RL AGN classification refers to the black-hole accretion mechanism occurring in these objects. As discussed in § 1.1.4, in this case the classification is not based on radio properties, but rather on the presence or absence of high-excitation emission lines in their optical spectra. Again, there is not one-to-one correspondence to the FR I/FR II dichotomy, despite almost all FRIs are Low Excitation Radio Galaxies (LERG) and (high power) FR IIs are usually High Excitation Radio Galaxies (HERG).

However, there seems to be a link between RG morphology and Blazars sub-classes. Both FR I RGs and BL–Lacs exhibit a correlation in the optical/radio luminosity plane (Chiaberge, Capetti & Celotti, 2000), while this correlation is not present for FR II RGs and FSRQs. The correlation shown by FR Is and BL–Lacs is explained in terms of lack of a dusty component (i.e., the torus) which would absorb the optical emission. This link has been revisited in terms of optical spectra classification, as both FR I and FR II LERGs show much smaller obscuration than FR II HERGs (e.g., Chiaberge et al., 2002). Hence LERGs are unified with BL-Lacs regardless their radio-morphology (Giommi, Padovani & Polenta, 2013). Indeed, the low accretion rates found in FRII LERGs (Macconi et al., 2020) confirm that these are not obscured counterparts of powerful FRII/HERGs, but they are inherently different class of objects that accrete at low-efficiency regime.

1.1.7 The origin of radio emission in RQ AGN

The vast majority (90% – 99%; Padovani 2011) of the AGN population is radio-quiet. However the term 'radio-quiet' can be misleading, as RQ AGN are not radio silent, but show some level of radio emission. This radio emission is usually confined within the host galaxy boundaries and hence is very different from the typical large-scale jets and lobes of classical radio galaxies (see Fig. 1.4). The origin of the radio emission in RQ AGN has become a very debated issue in the last ten years, when radio surveys started to reach a depth where RQ AGN are detected in significant numbers (see e.g. Padovani 2011). While classical radio galaxies and RL QSO represent the brightest radio source population, and dominate the extragalactic radio sky down to $S_{1.4\mathrm{GHz}} \sim 0.5$-1 mJy (Mignano et al., 2008), at fainter flux densities the composition of the radio sky changes dramatically. It is well known that synchrotron radio emission is produced in star forming regions, where elec-

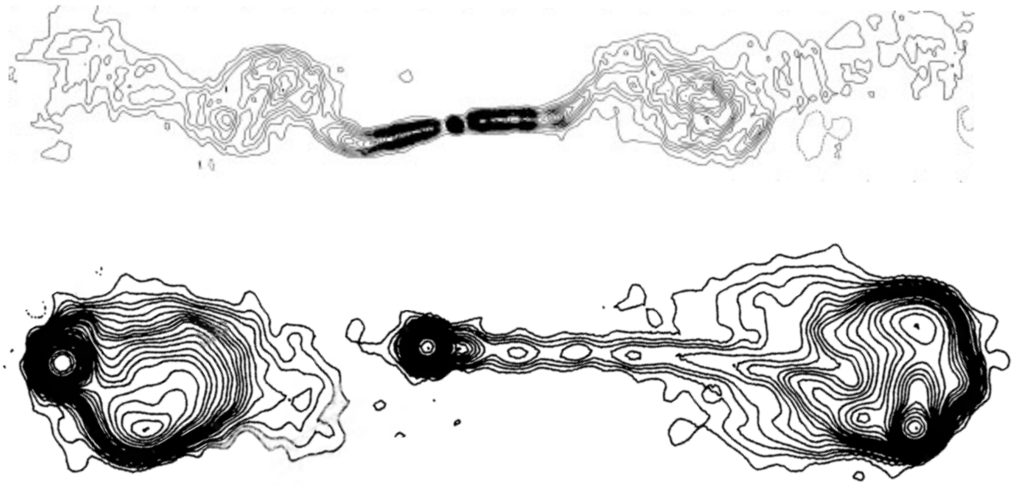

Figure 1.4: Examples of a classical FRI (top image, Perley, Willis & Scott, 1979) and a classical FRII (bottom image, Bridle et al., 1994) radio-galaxy.

trons are accelerated to relativistic speeds by Supernovae (e.g. Condon 1992). Radio emission in star-forming galaxies (SFG) is inherently weaker than in RL AGN (Wilman et al., 2008; Padovani et al., 2015; Smolčić et al., 2017a) and indeed SFG become the dominant radio population below flux densities of ~100-200 μJy (Simpson et al., 2006; Seymour et al., 2008; Smolčić et al., 2008). However, recent studies have shown that at such flux levels a significant fraction of radio sources display clear signatures of AGN activity at non-radio wavelengths. This RQ AGN population becomes dominant over RL AGN at flux densities $\lesssim 100\ \mu$Jy (e.g., Bonzini et al., 2013). RQ AGN often show similar properties to SFG, in terms of radio luminosity, host galaxy stellar mass, colour and morphology (e.g., Bonzini et al., 2013, 2015). In addition, their radio luminosity functions show similar evolutionary trends to SFG (Padovani, 2011). This led several authors to conclude that the radio emission in RQ AGN is triggered by star formation in the host galaxy disks (Padovani, 2011; Bonzini et al., 2013, 2015; Ocran et al., 2017). However, high-resolution radio follow ups of RQ AGN samples with VLBI arrays have shown that a significant fraction of RQ AGNs (20 – 40%, depending on the sample) contain AGN cores that contribute significantly (≥50%) to the total radio emission (Maini et al., 2016; Herrera Ruiz et al., 2016, 2017). The most likely scenario is that RQ AGN are composite systems where star formation and AGN triggered radio emission can co-exist, over a wide range of relative contributions. This scenario is supported by the recent modelling work of Mancuso et al. (2017), who showed that the observed radio counts can be very well reproduced by a three-component population (SFG, RL and RQ AGN), where RQ AGN are the sum of two sub-components: one dominated by star formation, and the other by AGN-triggered radio emission (see also Prandoni 2018).

The detection of significant numbers of RQ AGN at μJy flux density levels has opened new promising perspectives for AGN studies. Thanks to the lack of dust/gas obscuration at radio wavelengths, radio surveys are an extremely powerful tool to get an unbiased census of both star formation and AGN activity across cosmic time. In addition the ability of deep radio surveys to probe the whole AGN population, and not just the RL AGN minority, opens a new window on studies of galaxy/AGN co-evolution. However, the availability of extensive ancillary multi-band information remains critical. Identifying and characterizing faint radio-sources is challenging, and generally relies on a combination of multi-band diagnostics (e.g. optical spectroscopy, X-ray luminosities, mid-IR colors, SED fitting, etc.; see e.g. Prandoni et al. 2001b; Bonzini et al. 2013; Delvecchio et al. 2017; Duncan et al. 2018a,b).

1.1.8 AGN radio – X-ray luminosity correlations

A fundamental plane that puts in relation the X-ray emission, the radio emission and the BH mass in accreting systems has been discovered by Merloni, Heinz & di Matteo (2003) and independently by Falcke, Körding & Markoff (2004). The logarithmic X-ray-to-radio luminosity relation generally follows a linear correlation. The very existence of such correlations implies that accretion mechanisms and physics of the jets are likely scale-invariant, and therefore that the physical processes involved in the conversion of the accretion flow into radiated energy could be universal across a wide range of BH masses, in a wide range of radio and X-ray luminosities. Moreover, it has been argued that the slope of the correlations can be used as a proxy of the radiative efficiency of the accretion flow (see, e.g., Plotkin et al. 2012). As for AGN, the logarithmic X-ray-to-radio luminosity relation generally follows a linear correlation with a slope value distributed around 1 (Canosa et al., 1999; Brinkmann et al., 2000; Panessa et al., 2007). A flatter correlation (0.5 – 0.7) has been found for low-luminosity AGN (Dong et al., 2021), similar to that found for X-ray binaries (Narayan & Yi, 1994), and interpreted as a likely signature of an inefficient accretion process. In this framework, the radio emission is dominated by the jets' synchrotron contribution, while X-ray emission is dominated by the IC contribution due to electrons within a ADAF (Heinz & Sunyaev, 2003). These features are commonly associated with inefficient eccretion processes (see § 1.1.4), where the primary energetic output is in the form of kinetic energy ejected by the jets. Instead, in bright AGN (and some X-ray binary) a steeper relation (slope $\sim$1.4-1.6) is found, better described by an efficient accretion mechanism (Coriat et al., 2011; Dong, Wu & Cao, 2014). In this case the radio emission is dominated by the jets' synchrotron contribution, while the X-ray emission is owed to either jet's SSC mechanism. In this case, the X-ray emission lacks of the additional component due to the ADAF structure, and the SMBH accretion likely occurs in presence of geometrically thin, optically thick disk and efficient accretion mechanism, where most of the energy is rariatively dissipated (see § 1.1.4). As part of this Thesis we exploit new extremely deep X-ray and radio observations to further explore these correlations, and trace their evolution across cosmic time (see Chapter 5).

1.2 The AGN – host galaxy connection

The strict correlations exhibited by numerous observables in massive galaxies (e.g., Alexander & Hickox, 2012; Beifiori et al., 2012) are generally interpreted as clear signatures of a tight interaction between their several components, mutually affecting their physical properties through feedback processes (Silk & Rees, 1998; King, 2003, 2005; Murray, Quataert & Thompson, 2005). In particular, the mass of SMBH at the center of galaxies is found to correlate with the global properties (such as the luminosity, mass and velocity dispersion) of the stellar component over much larger (kpc) scales (e.g., Magorrian et al., 1998; Kormendy & Ho, 2013), indicating an intimate link between the feeding of black holes through accretion onto sub-pc scales and the formation of the stellar body in massive galaxies. The stellar mass building-up in galaxies results from the conversion of cold molecular gas into stars and is traced by the Star Formation Rate (SFR), that is also found to correlate with the accretion rate of the central SMBH (e.g., Gruppioni et al., 2011; Madau & Dickinson, 2014) and regulates the formation of the dust grains' seeds. For the work presented in this Thesis, of particular interest is the interconnection between the AGN and the host galaxy Inter-Stellar Medium (ISM) properties (see also Sect. 1.3). In the following a brief overview of the main ISM constituents is given, along with a brief summary of ISM properties, with a special focus on AGN host galaxies.

The ISM is composed of atomic and molecular gas, and dust grains. The gas reservoir makes up most of the ISM total mass, with typical gas-to-dust ratios ∼100 (Genzel et al., 2015; Daddi et al., 2015; Perna et al., 2018). The ISM is mostly composed by hydrogen and helium (which contributes for a small fraction of ∼10%, Scoville et al., 2014). The atomic gas absorbs the UV-light produced in the star-forming regions and re-emits it throughout strong emission lines, such as the Lyman-α (Ly-α, 1215.67 Å) and H-α (6562.81 Å) permitted lines and high-ionization forbidden lines such as the O[III] at 5008.24 Å. The molecular gas shows a filling factor of the galaxy volume significantly lower than the atomic component. Nevertheless, in high-z SFG, it is observed that the stellar radiation reprocessed and re-emitted by molecular gas significantly increases, due to the extremely dense environment (Perna et al., 2018; Circosta et al., 2019; D'Amato et al., 2020b). Moreover, in high-z QSOs the molecular gas mass is found to be a factor of ∼5 larger than the atomic gas reservoir (Calura et al., 2014).

In observations aiming at detecting the molecular gas ISM component, the most targeted emission lines are those produced by the carbon monoxide (CO). CO is one of the most abundant molecule after the molecular hydrogen (H_2), and unlike the H_2, the diatomic nature of CO implies the emission of dipole transition lines (J-transitions). Furthermore, the high dissociation energy of the CO molecules (11.1 eV) allows CO to survive even in heated environments such as star-forming regions. These features make the CO the best and widest used tracer of the molecular gas. The most targeted emission line is the ground-state CO(1→0) transition at 115.3 GHz (∼2.6 mm). Higher J-transitions are usually preferred for high-z and/or extremely dense objects, as their critical density is higher than the one of CO(1→0) (∼10^3 cm^{-3}), and they remain accessible to sub-mm facilities, when redshifted.

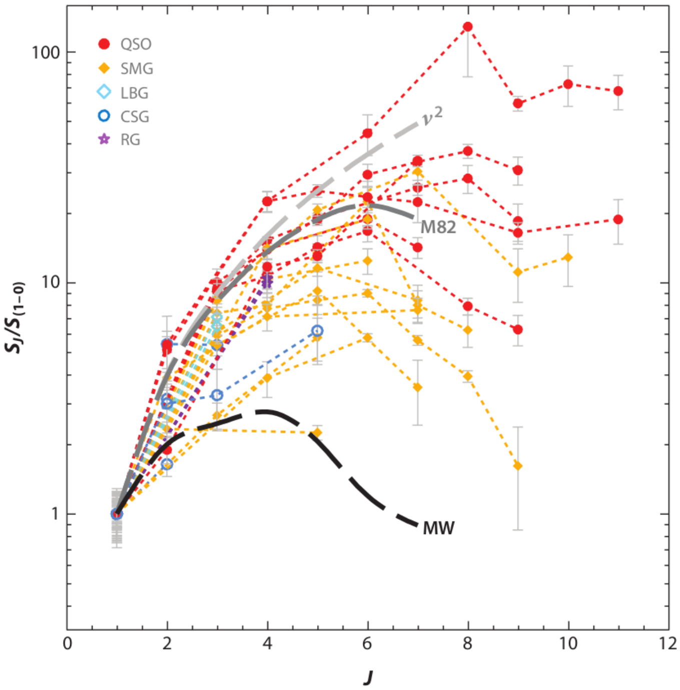

Figure 1.5: CO-SLED (also know as CO excitation ladder) for different classes of objects where the average CO(1→0) luminosities have been derived from available samples in the literature. The object classes are: Quasars (QSO), submillimeter galaxies (SMG), Lyman-break galaxies (LBG), color-selected galaxies (CSG), radio-galaxies (RG) (see Carilli & Walter 2013 for details). The CO-SLED of the Milky Way (MW) and M82 are also shown, along with the expected one for a constant brightness temperature object following the Rayleigh-Jeans law (valid for low-J, $S_\nu \propto \nu^2$). From Carilli & Walter (2013).

1.2.1 Molecular gas properties

The molecular gas excitation condition of AGN host galaxies is still a highly disputed topic, except for the brightest local objects such as the Ultra-Luminous IR Galaxies (ULIRG, Rosenberg et al., 2015). Different mechanisms may concur to the excitation of the molecular gas present in the ISM, especially in the innermost region close to the galaxy core (see Sect. 1.3). In particular, the CO Spectral Line Energy Distribution (CO–SLED) is determined by the combination of several factors, whose major (radiative-induced) contributions owe to the star formation (SF) in the photon-dominated regions (PDR) and to nuclear accretion activity in the X-ray dominated regions (XDR; see Meijerink & Spaans, 2005). Other physical processes possibly responsible for the molecular gas excitation are shock-induced mechanical heating (Rosenberg et al., 2015), supernovae- or AGN-driven outflows (Kamenetzky et al., 2016; Carniani et al., 2019) and turbolence (Harrington et al., 2021). As an example, in Fig. 1.5 typical CO-SLEDs for different classes of objects are reported (Carilli & Walter, 2013).

There is significant overlap in the properties of objects that are classified into different classes and/or through different selection criteria, especially for galaxies that host an AGN (Carilli & Walter, 2013). Several works have shown that the AGN contribution to high-J CO transitions is not negligible even in low-luminosity QSOs ($L_{2-10\ \mathrm{keV}} \sim 10^{42-43}$ erg s^{-1}, Pozzi et al. 2017; Mingozzi et al. 2018). This is especially true for compact high-z galaxies where the AGN contribution to high-J transitions can affect the whole source (Vallini et al., 2019). However, Daddi et al. (2015) have shown that, differently from what observed in local SFG, the high-J CO emission in high-z (z$\gtrsim$1) SFG is similar to that of AGN-hosting sub-millimeter galaxies (SMG). Furthermore, based on a sample of 55 AGN in the redshift range $z = 1 - 1.7$, Valentino et al. (2021) has recently claimed that the AGN has minimal effect in determining the excitation status of the host galaxy ISM in average star-forming galaxies, despite the fact that they observed the highest CO(5→4) luminosity in IR AGN-dominated sources.

Since all the mechanisms behind the molecular gas excitation produce similar CO excitation ladders, which typically show a flattening at high-J transitions (see Fig. 1.5), disentangling their contribution is a major challenge and one of the main uncertainties in determining molecular gas properties (Meijerink, Spaans & Israel, 2007; van der Werf et al., 2010; Kirkpatrick et al., 2019). Indeed, many key quantities, like gas mass and all mass-dependent parameters (e.g. star formation efficiency, depletion time, gas-derived SFR and gas fraction) require the knowledge of the CO(1→0) luminosity, which is often inferred by converting the observed transition luminosity into a CO(1→0) one by assuming a line ratio derived from a CO–SLED.

Besides the uncertainty on the CO line ratios, the major contribution to the molecular gas mass error is ascribed to the luminosity-to-mass conversion factor, namely:

$$\alpha_{CO}\ [\mathrm{M_\odot}\ (\mathrm{K\ km\ s^{-1}\ pc^2})^{-1}] = M_{H_2}/L'_{1-0}\ , \tag{1.1}$$

where M_{H_2} is the mass of the molecular hydrogen and L'_{1-0} is the CO(1→0) transition luminosity (e.g., Kaasinen et al., 2019). Typical values of α_{CO} range between 0.8 – 4, where the lowest value (~0.8, Solomon & Vanden Bout, 2005) is usually preferred for high-z compact AGN-hosting galaxies such as SMG, and the highest value (~4) is assumed for normal SFG (based on what is found for giant molecular clouds in the Milky Way; Bolatto, Wolfire & Leroy 2013). Lower values of α_{CO} imply higher luminosity per unit of molecular gas mass; as pointed out by Papadopoulos et al. (2012), an excess of emission may result from either AGN heating or intense star formation activity. Several source properties can affect the excitation level of the molecular gas, such as the compactness of the source, the AGN influence, and the physical scale on which the star formation occurs (Weiß et al., 2007). In fact, a α_{CO}~1 (i.e., a value typically measured for AGN and starburst galaxies) has been derived in several works (Schreiber et al., 2015; Magdis et al., 2012) for both local and high redshift SFG lying on the so-called stellar mass - star formation rate (M_* – SFR) main sequence; however, several works have shown that a Galactic α_{CO} value may hold also in SFG lying an order of magnitude above the M_* – SFR main sequence (Genzel et al., 2015; Tacconi et al., 2018). In addition, Scoville et al. (2014, 2016) suggest to use a single value of α_{CO}~6 for normal SFG, ULIRGs and SMG, arguing that lower values would be inappropriate to derive the integrated mass of the gas globally distributed in the host galaxy, although they may be suited for the gas conditions observed in the very nuclear region.

Based on the aforementioned uncertainties on the CO transition line ratios and α_{CO}, in this work we will make the most reasonable assumptions on conversion factors, on the basis of our knowledge about the physical condition and spatial distribution of the molecular gas reservoir in the analysed sources, and will discuss the implications of different assumptions whenever they affect the main conclusions. Furthermore, we will report independent measurements of the gas-derived quantities and will compare them, wherever is possible.

1.2.2 Dust properties

Despite the dust represents only a small fraction of the total ISM mass budget, the thermal emission emitted by dust, and resulting from the reprocessing of the UV-light produced by young stars embedded in it, dominates the far-IR (FIR) emission of SFG, including those hosting an AGN at their center.

The "dust" component underlies a variegate composition of grains with different sizes and physical properties, depending on the chemical abundance of metals and the physical conditions of the environment. Its main components are small-size grains of graphite carbon, silicates and polycyclic aromatic hydrocarbons (PAH), but larger structures can also be present, such as ice, diamonds and organic molecules. An important parameter regulating the grain size distribution in the ISM is the density of the environmental gas (Mathis, Rumpl & Nordsieck, 1977). Major efforts have been made since the beginning of the 20th century to build-up a consistent classical theory that describes the scattering/absorption of electromagnetic waves due to dust grains, as a function of the grain size and incident radiation wavelength (Mie, 1908; Debye, 1909). Recently, the emission of complex molecules such as PAH have been included in modeling-templates of the dust ISM component (e.g., Draine & Li, 2007; Draine et al., 2021). Clear signatures of dust complex compounds, observed in the MIR/FIR band, are the series of emission lines produced by PAH in the 3 – 13 μm range and a strong absorption component owed to silicates at ~9.7 μm. Fig. 1.2 (bottom panels) shows the total IR SED of an AGN, for different grades of obscuration (Type I, Intermediate Type and Type II). It is noteworthy that the silicate and the other absorption features due to compounds in the torus (see § 1.1.1 and § 1.1.2) become more visible going from Type I to Type II AGN, since they depend on the obscuration level.

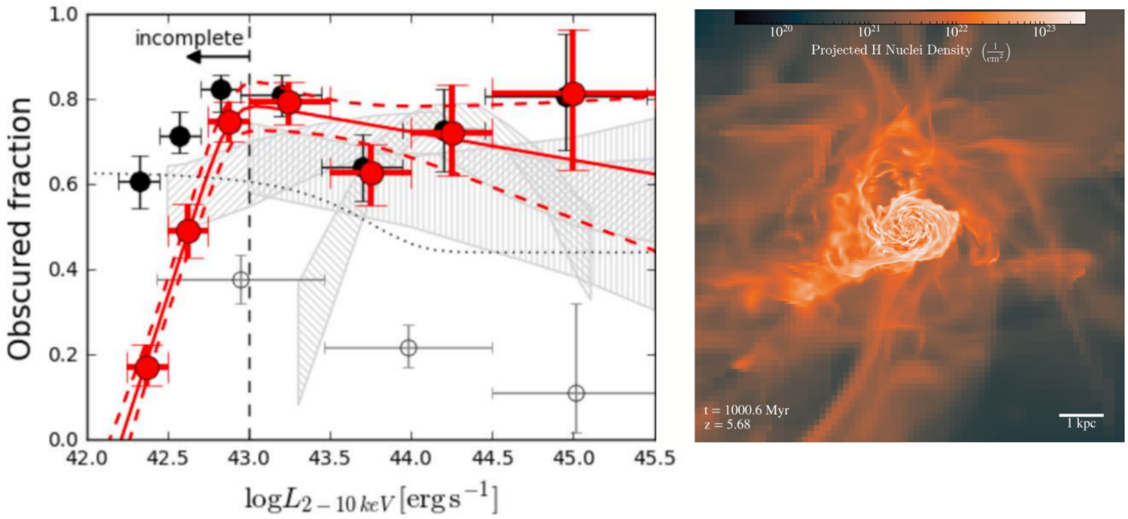

Figure 1.6: *Left*: fraction of obscured AGN with $\log N_H > 23$ vs. intrinsic X-ray luminosity as measured in the Chandra Deep Field North and South at z~4 (red and black points) and compared with other similar estimates at high-z (grey shaded areas, z ~3-5, see Vito et al. 2018 for further details) and in the local Universe (grey open circles, Burlon et al., 2011), showing an increasing of the obscured fraction with redshift. From Vito et al. (2018). *Right:* column density of the simulated galaxy gas distribution at the end of the cosmological hydro-dynamics simulation (z~5.7) performed by Trebitsch, Volonteri & Dubois (2019), showing that at high redshift the ISM can produce column densities up to $\log(N_H) \gtrsim 23$.

Despite the complexity of the dust composition, the main thermal dust emission component, peaking at 100-200 μm (see Fig. 1.2, bottom panels), is described fairly well by a simple Modified Black Body (MBB, also known as "grey-body") model. Assuming thermal equilibrium, the balance between heating and cooling of the dust grains can be written as the equilibrium between the absorbed and re-emitted flux density: $S_{\nu,i}\; Q_{abs}(a,\nu) = B_\nu(T_{dust})\; Q_{em}$, where $S_{\nu,i}$ is the incident flux density at a given frequency ν, $Q_{abs}(a,\nu)$ is the efficiency coefficient of absorption as a function of the grain size a, $B_\nu(T)$ is the black body Planck function and Q_{em} is the efficiency coefficient of emission. The term Q_{em} varies from 1 for a perfect black body to 0 for a dielectric material, so that it can be written as a function of the optical depth τ: $Q_{em} = 1 - e^{-\tau}$. The optical depth is a function of the emitting frequency ($\tau \propto \nu^\beta$), with the β index value spanning between 1 for amorphic grains and ~2 for metals and crystals (Conley et al., 2011; Rangwala et al., 2011).

1.2.3 The role of the host galaxy in AGN obscuration

Many observational and theoretical arguments have shown the important role of the host galaxy ISM in obscuring AGN, beyond the circum-nuclear torus (see Bianchi, Maiolino & Risaliti, 2012), particularly at high redshifts. Indeed, Vito et al. (2014) found an increasing fraction of heavily obscured AGN (column density $\log N_H > 23$) with increasing

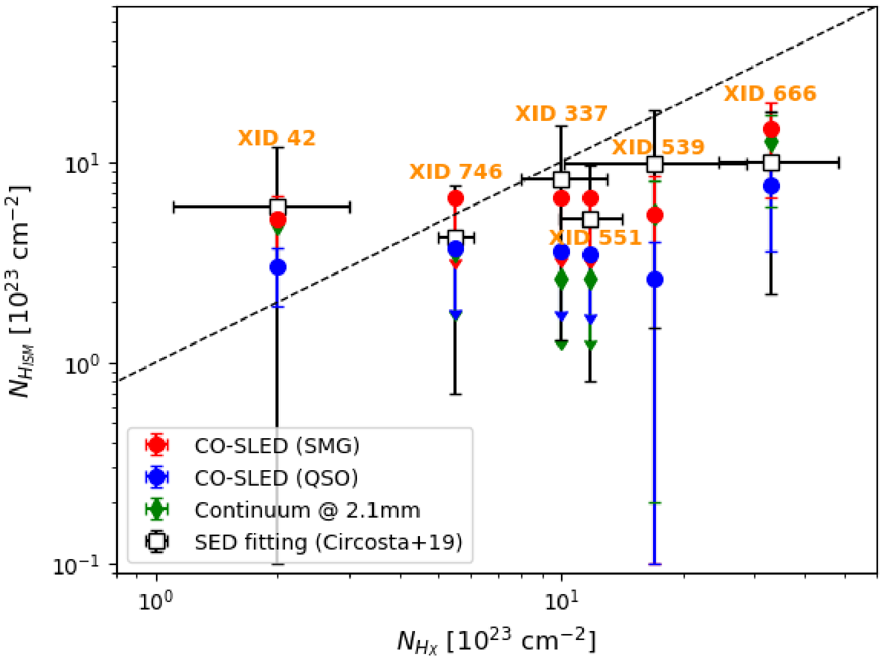

Figure 1.7: X-ray derived column densities (x-axis) vs. ISM column densities derived from ALMA data using different methods (y-axis) for a sample of obscured AGN at z = 2.5 - 4.7 in the CDF-S (D'Amato et al., 2020b). The values related to the SMG CO–SLED, the QSO CO–SLED, and the continuum emission method are indicated by the red circles, blue circles, and green diamonds, respectively. We also report on the y-axis (black open squares) the column densities derived from the SED fitting by Circosta et al. (2019). The source IDs are reported in orange. The black dashed line represents the 1:1 relation. ISM densities can reach values as high as $\log N_H \sim 24$, which suggests that the increase in the AGN obscured fraction with redshift can be linked to off-nuclear absorption.

redshift, which reaches up to 80% at z∼4. This is significantly higher than the one measured in the local Universe (∼40% Burlon et al., 2011). In addition, the AGN obscured fraction appears to be nearly constant as a function of X-ray AGN luminosity at z≳3, whereas it decreases with luminosity in the local Universe, suggesting an evolution of the AGN obscuration (Vito et al., 2018, see Fig. 1.6, left panel). Finally, several works have shown that the gas fraction (M_{gas}/M_{tot}) increases with redshift in AGN host galaxies (e.g., Carilli & Walter, 2013; Perna et al., 2018) despite the host galaxy average size decreases, suggesting that the host-galaxy ISM plays a major role in determining the obscuration of high-z AGN. In this framework, AGN obscuration is no longer (or solely) explained in terms of viewing angle, as postulated by the Unified Models, but is rather owed to an evolutionary stage of the galaxy. Indeed, a recent cosmological radiative hydro-dynamics simulations of an evolving high-redshift galaxy has shown that the host galaxy ISM can produce column densities up to $\log N_H \gtrsim 23$ in the inner ($\lesssim$ 3 kpc) region of these objects (Trebitsch, Volonteri & Dubois, 2019, see Fig. 1.6, right panel).

In D'Amato et al. (2020b) we addressed the contribution of the host galaxy ISM to the nuclear obscuration of distant (z>2.5) AGN, based on Atacama Large (sub-)Millimeter Array (ALMA) observations of six X-ray-selected SMG (Blain et al., 2002) in the CDF-S (originally presented by Circosta et al. 2019). For the selected sources we measured the ISM mass, size and column density. We compared the gas masses derived from three independent measurements (high-J CO emission lines, continuum dust emission and SED fitting), finding a good agreement. For the first time we derived the column densities from the resolved gas emission, exploring different geometries and conversion factors, and compared them to those derived from X-ray data. We found that in all cases the ISM significantly affects the AGN obscuration (see Fig. 1.7). Despite the small size of the analysed sample, this study lays a solid foundation for measurement methods of the ISM content in distant AGN, and provides strong arguments in favour of the 'evolutionary' interpretation of the increasing fraction of observed obscured AGN towards the early Universe.

1.3 The role of AGN feedback in galaxy evolution

The formation of massive galaxies and their evolution across the cosmic time is one of the key research field of modern Astrophysics. It is now widely believed that feedback processes associated with AGN can play a role in shaping galaxies over cosmic time, by changing the physical conditions of the surrounding ISM (see § 1.2.1) or expelling it from the nuclear regions, thus impacting the star formation processes and the subsequent evolution of the host galaxy (e.g. Combes 2017; Harrison 2017). Feedback from AGN is commonly invoked in two (non exclusive) flavors: radiative and kinetic (see e.g. Fabian 2012, for a review). The former is postulated to occur through powerful winds that are typically associated to radiatively efficient (Quasar- or Seyfert-like) AGN; the latter is associated to strong radio-emitting outflows of relativistic particles (i.e. the radio jets). For this reason the latter is also referred to as 'radio-mode' feedback. In the last decade, major efforts have been made to investigate the incidence of the AGN feedback in determining the galaxies' properties, especially at the epoch of the so called "cosmic noon", when the star formation and AGN activity peak ($z \sim 1-3$; Madau & Dickinson 2014); the results often lead to opposite claims, where the AGN has null or mild impact in affecting the SFR and ISM properties (Stanley et al., 2017; Kirkpatrick et al., 2019; Valentino et al., 2021), or where significant decreased gas fractions and shortened depletion timescales in the presence of AGN are found (Perna et al., 2018; Brusa et al., 2018). The many details of these processes and their incidence on galaxy evolution still remain poorly understood.

The AGN feedback is thought to affect also the properties of the medium that surrounds the AGN in large scale structures (LSS), such as galaxy clusters. The intra-cluster medium (ICM) constitute the majority of the baryonic matter (~75%) in local clusters, featuring densities of $n_e \sim 10^{-3} - 10^{-4}$ cm^{-3} and high temperatures ($T \sim 10^7 - 10^8$ K). The hot gas predominantly cools through thermal *bremsstrahlung* emission visible in the X-ray band, which is proportional to the electron and ion density and shows a sharp exponential cut-off above few tens of keV (e.g., Rosati, 1998). In the local Universe, however, there is established evidence of interactions between the jets of RGs (often found at the center of the cluster) and the surrounding ICM, through the observation of so-called "X-ray cavities" (i.e., depression of the thermal X-ray emission of the hot gas in correspondence with the radio emission of the jets and lobes of the BCG; e.g. Boehringer et al., 1993; Carilli, Perley & Harris, 1994; Bîrzan et al., 2004). Recently, Brienza et al. (2021) also showed that the magnetized plasma ejected by the AGN can reach Mpc scales. The X-ray band is particularly important to investigate several AGN feedback processes, since it allows to probe the innermost accretion mechanism responsible of the injection of energy and matter into the host-galaxy ISM (La Franca, Melini & Fiore, 2010; Bonchi et al., 2013, see also § 1.1.2) and ICM (McNamara & Nulsen, 2007; Fabian, 2012). However, the radio band is essential to study the properties of the large-scale radio jets produced by the AGN, that can affect both the host galaxy and the environment surrounding it. Finally (sub-)mm observations can probe the ISM, which constitutes the essential fueling for both SMBH accretion and star formation. In this Thesis we are particularly interested in studying the role of AGN large-scale feedback (see § 1.3.3) in regulating the star formation and ICM heating within the first gravitationally-bound LSSs (see next § 1.3.1), assembling at the "cosmic noon".

1.3.1 Proto-clusters: the cradles of galaxy assembly

Proto-clusters are the largest non-virialized scale structures in the high-redshift Universe that are going to form virialized gravitationally-bound systems at the present epoch (i.e., galaxy clusters of $\gtrsim 10^{14}$ $M_{\odot}$; Bower et al., 2004). Cosmological simulations show that the most massive ($\gtrsim 10^{15}$ $M_{\odot}$) present-day clusters assembly takes place at a redshift between z~4 and z~1 (see Fig. 1.8, Boylan-Kolchin et al., 2009; Muldrew, Hatch & Cooke, 2015). Galaxies residing in local clusters are generally different from field galaxies: most of them are early-type galaxies, and the few SFG show different properties with respect to isolated objects, such as neutral hydrogen deficiency (e.g., Abell, 1965). Such a distinctive galaxy population indicates that an interplay between cluster galaxies and the surrounding ICM occurred and somehow affected their properties during their earlier evolution. The crossing time ($t_{cr} = R_{cl}/\sigma_v$) derived from typical velocity dispersion of galaxies in local clusters (σ_v~1000 km/s) and the typical cluster size of (R_{cl}~1 Mpc) implies that these systems must have settled in a short period of time (~1 Gyr) compared to the Hubble time (Abell, 1958). Proto-clusters represent ideal laboratories to study galaxy assembling and this short, crucial phase in the transformation of galaxies. They also represent an unique class of objects to investigate the role of large-scale feedback in promoting or quenching the star-formation process (e.g., Venemans et al., 2007, and references therein). Finally, proto-clusters are important tools to place constrains on cosmology, since their number density is a strong function of many cosmological parameters (Eke, Navarro & Frenk,

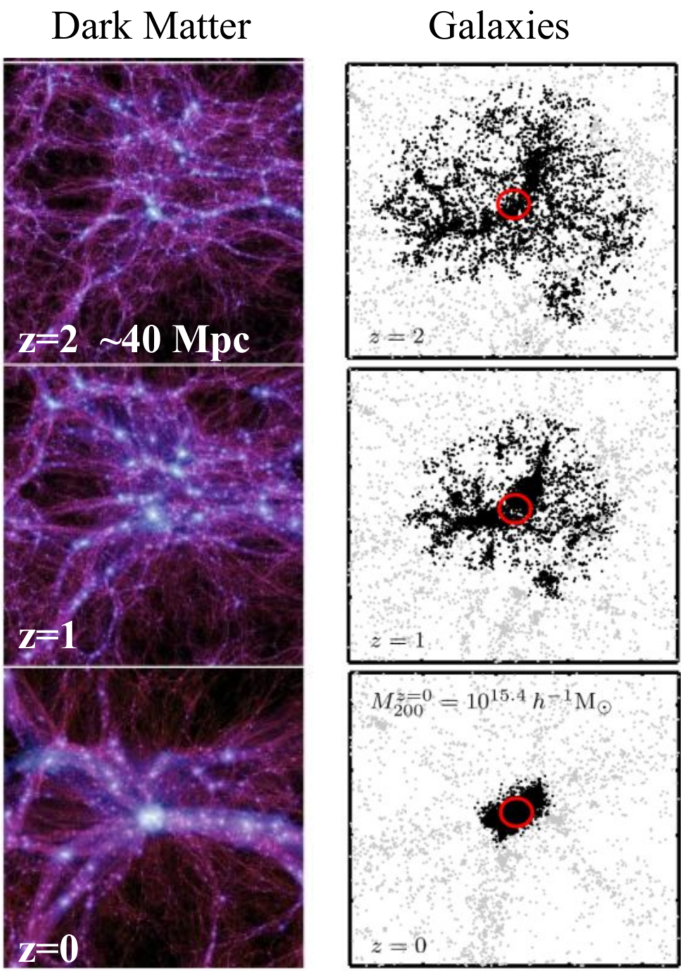

Figure 1.8: *Left*: evolution of the dark matter distribution for a massive cluster $M_{z=0} \sim 10^{15}$ $M_\odot$ in the Millennium II simulation (adapted from Boylan-Kolchin et al., 2009). *Right*: Evolution of the baryonic matter for comparable scale and cluster mass of left panel, in which each dot is a galaxy with mass $\geq 10^8$ $M_\odot$ (adapted from Muldrew, Hatch & Cooke, 2015).

1998). While their late-stage gravitational collapse can be studied theoretically in numerical cosmological simulations (e.g., De Lucia & Blaizot, 2007; Pillepich et al., 2018), the early stages of their evolution remain mostly unknown, especially prior to virialization (see the review of Overzier, 2016), mostly due to the limited number of systems discovered so far (Chiang, Overzier & Gebhardt, 2013).

Among the several methods currently available to blindly search for these structures, often limited by the IR and X-ray survey sensitivity in searching for red galaxies and hot gas diffuse emission, or requiring time-expensive multi-band observations to determine photometric redshifts (see Overzier 2016), one of the most promising technique that has been enabled by recent deep radio-surveys is the research of galaxy overdensities around high-z radio galaxies (HzRGs; e.g., Daddi et al., 2017). In Sect. 6.1 we recap the main cluster-finding methods and their current limitation at high-redshift, and highlight the importance of deep radio surveys in this newborn field of research, especially in light of the forthcoming extremely sensitive radio-surveys. As a matter of fact, it is now well established that HzRGs are excellent proto-cluster signposts, (e.g., Carilli et al., 1997; Pentericci et al., 2000; Venemans et al., 2007; Miley & De Breuck, 2008; Chiaberge et al., 2010; Strazzullo et al., 2015). Proto-clusters assembling around HzRGs also offer a unique opportunity to i) study the initial evolutionary stages of the future brightest cluster galaxy (BCG), as HzRGs generally represent proto-BCGs, i.e. the galaxies around which clusters assemble (see § 1.3.2 for a more detailed discussion of BCGs); ii) investigate HzRG-induced radio-mode feedback on the surrounding environment, i.e. the ICM and the nearby galaxies.

1.3.2 High-z powerful radio-galaxies

The description of powerful, classical RL AGN reported in § 1.1.6 mainly refers to local radio galaxy samples. The properties of powerful radio-AGN and of their host galaxies may significantly vary across cosmic time, since both the surrounding environment and the AGN duty-cycle evolve with cosmic time, as a consequence of the evolution of several key physical properties such as the stellar mass, the SFR, the gas reservoir and the SMBH accretion. In this section we will describe the main properties of extended extragalactic radio-sources at high redshift, with particular regard to the host galaxy gas reservoir and to the interaction with the external environment.

The number density of luminous ($L_{1.4\ \mathrm{GHz}} \gtrsim 10^{26}$ W/Hz) radio-galaxies, quantitatively corresponding to the FRII/HERGs population (Padovani et al., 2017), experiences a strong evolution, dramatically increasing of a factor 100-1000 from the local Universe to $z \gtrsim 2.5$ (Dunlop & Peacock, 1990; Willott et al., 2001). This epoch corresponds to a crucial phase of the Universe, when star formation and black hole accretion reach peak of their activity (Madau & Dickinson, 2014) and clusters assembly is still ongoing (see § 1.3.1). As a result, HzRGs generally differ in many properties with respect to their local counterparts. On average, they show higher luminosities and more compact sizes, although they usually share the same morphology of classical local FRII radio-galaxy. A comprehensive review of the general properties of these objects has been presented by Miley & De Breuck (2008). In this work we are mainly interested in the properties of their host galaxies' ISM (with special respect to the molecular gas reservoir that traces the star-formation activity) and in the interaction between the HzRGs and their surrounding environment.

At low-redshift, powerful radio-galaxies are generally hosted by quiescent elliptical galaxies residing at the center of galaxy clusters, which typically coincide with the BCG (Owen et al. 1996; Best et al. 2005). The rare star-forming BCGs are found at the center of cool cores, fed by streams of large-scale cooling flows (e.g., Rawle et al., 2012). The observational evidence for a stellar mass growth by a factor of 2 since $z \sim 1$ (Lidman et al., 2012; Zhang et al., 2016) led to assume a scenario where a significant fraction of the BCG stellar mass is built at later stages through dry mergers with satellite galaxies, in addition to an initial (z ~5) cooling flow accretion rapidly suppressed by AGN feedback (De Lucia & Blaizot, 2007). However, an increasing number of detections of substantial molecular gas reservoirs ($M_{H_2} \sim 10^{10} - 10^{11}$ M$_\odot$) in the host of HzRGs (z$\gtrsim$1.5) at the center of proto-clusters have been reported in the last decade, mostly thanks to ALMA observations (Daddi et al., 2009; Wagg et al., 2012; Casasola et al., 2013; Emonts et al., 2014, 2016; Casey, 2016; Webb et al., 2017; Ginolfi et al., 2017; Noble et al., 2017; Castignani, Combes & Salomé, 2020). In light of these findings, Webb et al. (2015) and McDonald et al. (2016) proposed that the BCG growth at $z \gtrsim 1$ is driven by gas-rich major mergers occurring at the center of the forming LSSs. However, the processes that trigger and regulate the star formation are still poorly understood; some evidence of enhanced star-formation in BCGs promoted by the interaction with diffuse nearby gas reservoirs was found by Webb et al. (2017).

1.3.3 Large-scale feedback of HzRGs

The detection of X-ray diffuse emission distributed around the jets and lobes of proto-BCGs in distant proto-clusters has been extensively reported in literature (Carilli et al., 2002; Fabian, Celotti & Johnstone, 2003; Scharf et al., 2003; Belsole et al., 2004; Erlund et al., 2006; Johnson et al., 2007). The most widely invoked mechanism to explain such an emission is the non-thermal IC scattering between the CMB photons and the relativistic electrons ejected by the HzRG (Fabian, Celotti & Johnstone, 2003; Scharf et al., 2003; Belsole et al., 2004; Erlund et al., 2006; Johnson et al., 2007). Such a process becomes increasingly important with redshift, since the CMB photon density increases $\propto (1+z)^4$. However, similar interactions observed in the local Universe clusters (see Sect. 1.3) may be present also in proto-clusters. Hence a possible source of the X-ray diffuse emission co-spatial with the HzRGs jets and lobes, in addition to the IC scattering of the CMB photons, could be thermal emission arising from the shock-heated gas at the loci of the jet-ICM interaction (Carilli et al., 2002; McNamara et al., 2000; Belsole et al., 2004). In this scenario, the HzRGs inject energy in the ICM through the jets proceeding outwards, causing its heating. Another important piece of evidence pointing towards AGN mechanical feedback, to explain the heating of the medium surrounding HzRGs, consists of the giant Ly-α emitting nebulae detected (up to several hundreds of kpc) around many HzRGs (e.g., McCarthy, 1993; van Ojik et al., 1996; De Breuck et al., 2000; Reuland et al., 2003). Line-diagnostic analysis reveals that this emission arises from warm gas ($T \sim 10^4 - 10^5$ K) distributed in irregular and clumpy structures filling the space within the proto-clusters (van Ojik et al., 1997; Osterbrock & Ferland, 2006; Villar-Martín et al., 2007). Among the various mechanisms that can concur to the excitation and ionization of the gas, the main one is considered to be AGN feedback from the central object (Overzier et al., 2013), even in the presence of starburst activity (Stevens et al., 2003; Villar-Martín et al., 2007; Hatch et al., 2008).

A prototypical case study is represented by the so-called "Spiderweb" proto-cluster at

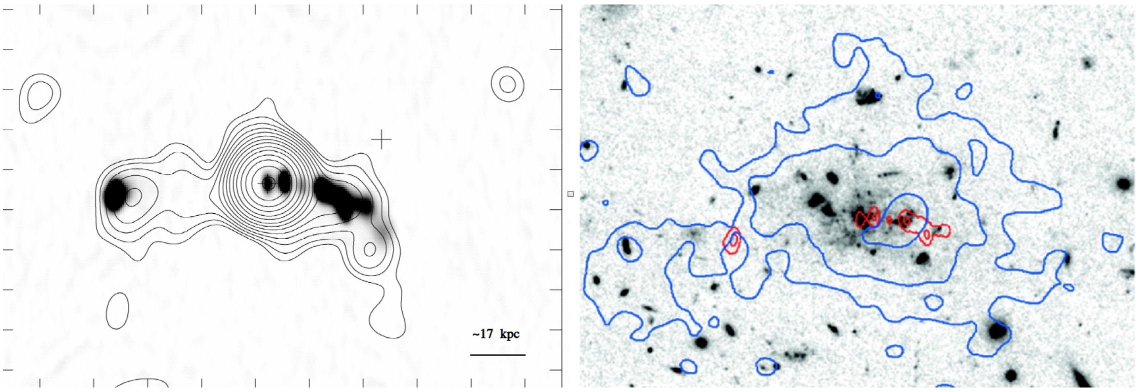

Figure 1.9: *Left*: X-ray emission from the HzRG at the center of the Spiderweb proto-cluster at z=2.2 (black contours), superimposed on the radio image at 5 GHz, showing the alignment of the X-ray emission along the radio-jets (adapted from Carilli et al., 2002). *Right*: Ly-α emission (blue contours) superimposed on the HST ACS composite ($g_{475}+I_{814}$) image showing the huge amount of satellite galaxies surrounding the HzRG. The contours of the emission at 8 GHz are marked in red (from Miley et al., 2006).

z = 2.2. This extensively studied structure shows very interesting properties, consisting of an agglomerate of SFG surrounding a powerful HzRG ($L_{1.4\ \mathrm{GHz}}$~1.25 × 10^{28} W/Hz, AGN $L_{2-10\ \mathrm{keV}}$~4 × 10^{45} erg/s) hosted by a massive galaxy (stellar mass ~10^{12} $M_\odot$) in a starbursting phase (> 1000 $M_\odot$/yr) (MRC 1138-262, Pentericci et al., 1997; Carilli et al., 2002; Stevens et al., 2003; Hatch et al., 2008; Miley et al., 2006; Seymour et al., 2012). This structure is part of a larger proto-cluster extending on ~3 Mpc scale (Kurk et al., 2004; Dannerbauer et al., 2014). In the Spiderweb proto-cluster, the radio AGN shows evidence for strong interaction with the surrounding medium (Pentericci et al., 1997). Hot gas elongated in the direction of the HzRGs jets has been detected in X-ray band by Carilli et al. (2002) and Saro et al. (2009), and was interpreted as a signature of shock-heated gas (Fig. 1.9, left panel), since the X-ray emission presents an offset with respect to the high surface brightness radio features and extends well beyond the photon field dominated by the CMB (~ 10 kpc from the nucleus). Furthermore, the central part of the structure, comprising the HzRG and satellite SFG, is immersed in a giant Ly-α nebula (~200 kpc, Pentericci et al., 1997; Kurk et al., 2004; Miley et al., 2006, see right panel of Fig. 1.9). Recently, Emonts et al. (2016) reported the discovery of a large gas reservoir (~10^{11} $M_\odot$) lying between the SFG located around (~50-70 kpc) the central BCG. In addition, Emonts et al. (2018) compared the emission of high- and low-J CO transitions, finding that in the BCG other processes than SF-heating concur to the excitation of the gas (e.g., cosmic rays and AGN feedback), and that the metal enrichment found in the gas around the HzRG suggests a link between the presence of the local cold molecular gas and the star-formation. Interestingly, most of the current star-formation in the central region of the Spiderweb proto-cluster occurs in the surrounding low-mass galaxies (~18 sources, Hatch et al., 2009), suggesting a possible interaction between the BCG, the ICM

and possibly the satellite SFG.
While the contribution of the HzRGs in heating the surrounding ICM has been convincingly established, its role in regulating the star-formation in neighbouring galaxies is still unclear. Either "positive" or "negative" feedback has been claimed, that is the capability of the AGN to respectively enhance or quench the star-formation through mechanical and/or radiative effects. As for the HzRG host, signatures of negative feedback are generally found, such as strong gas outflows that have the energy to remove significant gas fractions (Nesvadba et al., 2006) and evidence of disruptive interaction between the jet and nuclear molecular gas disks (Ruffa et al., 2019). However, some HzRGs display evidence of star formation triggered by the radio-jets, due to compression of the molecular clouds, such as the case of 4C 41.17 at z=3.8, which features UV-line emission along the radio-jet axis (e.g., Dey et al., 1997; Bicknell et al., 2000; Steinbring, 2014). In the local Universe, jet-triggered star-formation has been extensively reported by the detection of blue filaments aligned with the jets ("alignment effect"; e.g., Rees, 1989). Examples are found along the jets of Centaurus A (Graham, 1998; Mould et al., 2000; Rejkuba et al., 2002; Salomé et al., 2016), 3C285 (van Breugel & Dey, 1993; Salomé, Salomé & Combes, 2015), NGC 5643 (Cresci et al., 2015) and 3C277.3 (Capetti et al., 2021). Star formation induced by radio-jets is also supported by statistical arguments inferred from the analysis of large samples of radio sources (e.g., Zinn, Middelberg & Ibar, 2011; Kalfountzou et al., 2017; O'Dea & Saikia, 2021), and is expected to be more relevant at high redshifts, given the higher star formation rate density (Drouart et al., 2014; Capetti et al., 2021). Little is known about the possibility that these powerful jets can also trigger star formation in companion galaxies. Currently, only few systems are known showing such evidence: the Minkowski's Object located along the path of the FRI galaxy NGC 541 in the Abell 194 local cluster (Brodie, Bowyer & McCarthy, 1985; van Breugel et al., 1985; Croft et al., 2006; Salomé, Salomé & Combes, 2015; Lacy et al., 2017; Fragile et al., 2017; Zovaro et al., 2020) and the 3C 441 radio-galaxy at z=0.7, where the radio-jet impacts on a companion galaxy in the same group, showing features of star formation enhancement (Lacy et al., 1998; Wang, Wiita & Hooda, 2000; Kaiser, Schoenmakers & Röttgering, 2000; Wiita, Wang & Hooda, 2002; Simpson & Rawlings, 2002). Whether the ICM plays an intermediary role between the radio-galaxy and its companions, whether the jet-ICM interplay can lead to positive AGN feedback on multiple galaxies, and which is the incidence of this mechanism in the evolution of the intra-cluster galaxy population, remain all open questions to date.
In summary, proto-clusters are key systems where many complex physical phenomena, occurring on different spatial and temporal scales, can be studied. This can be done by exploiting observations across a broad frequency range: the X-ray band traces the sub-pc SMBH accretion, ICM heating and large-scale feedback (e.g., jet-induced shock fronts); the Ultraviolet/Optical band probes the galaxy stellar component, the AGN activity and the star-formation; star formation can be also investigated in the IR-mm band, as well

as the molecular gas reservoir and the dust component, through continuum and/or line observations; finally, the radio-band can be exploited to explore the jets' properties and the jet-ICM interaction. It is then clear that a multi-wavelength approach is of paramount importance to provide observational constraints to the proto-cluster evolution in the early Universe, and trace the interaction within their members.

In this work we discuss a proto-cluster at z=1.7 serendipitously discovered in the so-called "J1030" field. This system presents the first potential evidence of jet-induced star formation on multiple galaxies distributed on hundreds of kpc scale (Gilli et al. 2019). To this aim, we exploit the exceptional multi-wavelength coverage of the J1030 field, focusing on novel proprietary mm-radio data. In Chapter 2 we provide a general overview of the field and of the proto-cluster, based on the available data/analysis prior to this thesis.

Chapter 2

The J1030 equatorial field: the benefits of the bias

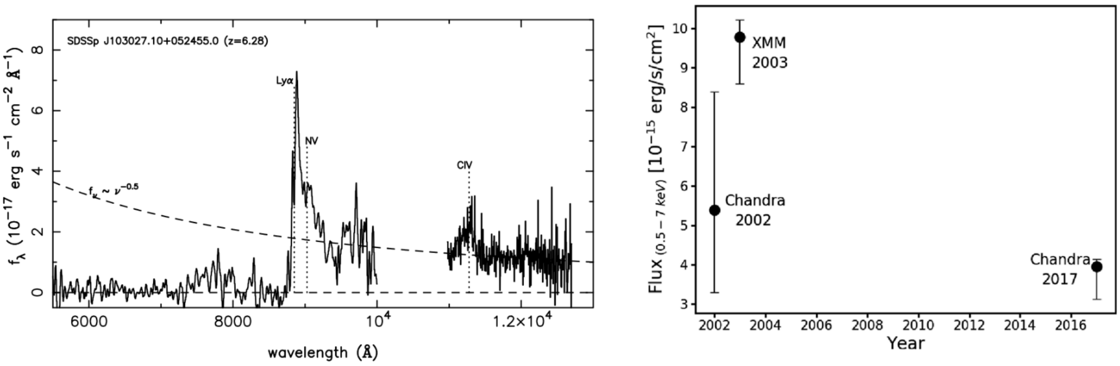

Figure 2.1: *Left:* Combined optical/NIR spectrum of SDSS 1030+0524 (solid line). The main spectral features are labeled, while the powerlaw reproducing the continuum emission and parameterized as $f_\nu \propto \nu^{-0.5}$ is indicated by the dashed line. From Fan et al. (2001). *Right:* Long-time light-curve of the QSO, where the variation of the emission between the XMM-Newton observations in 2003 and the *Chandra* observations in 2017 is visible. From Nanni et al. (2018).

One of the best laboratories to investigate high-z AGN and galaxy evolution is the equatorial field centered around the $z = 6.3$ Sloan Digital Sky Survey (SDSS) QSO J1030+0524 (RA = $10^h30^m27^s$, Dec = $+5°24'55''$, Fan et al. 2001). QSO J1030+0524 was firstly identified from a survey of i-dropout objects and following spectroscopic analysis performed by Fan et al. (2001). The Optical/NIR spectrum of the source is shown in the left panel of Fig. 2.1. The spectrum reveals a depression of the continuum emission in the ~300 Å wavelength range blueward of the Ly-α emission line, corresponding to the Ly-α forest region. This feature has been lately confirmed (Becker et al., 2001; Pentericci et al., 2002) as the first detection of the so-called Gunn–Peterson trough originally hypothesized by Gunn & Peterson (1965), where the neutral hydrogen in the inter-galactic medium causes the absorption of the emission at shorter wavelengths than the rest-frame Ly-α emission of the object. Based on the NV/CIV line ratio, Fan et al. (2001) also estimated that the quasar environment has a super-solar ($\sim\times3$) metallicity.

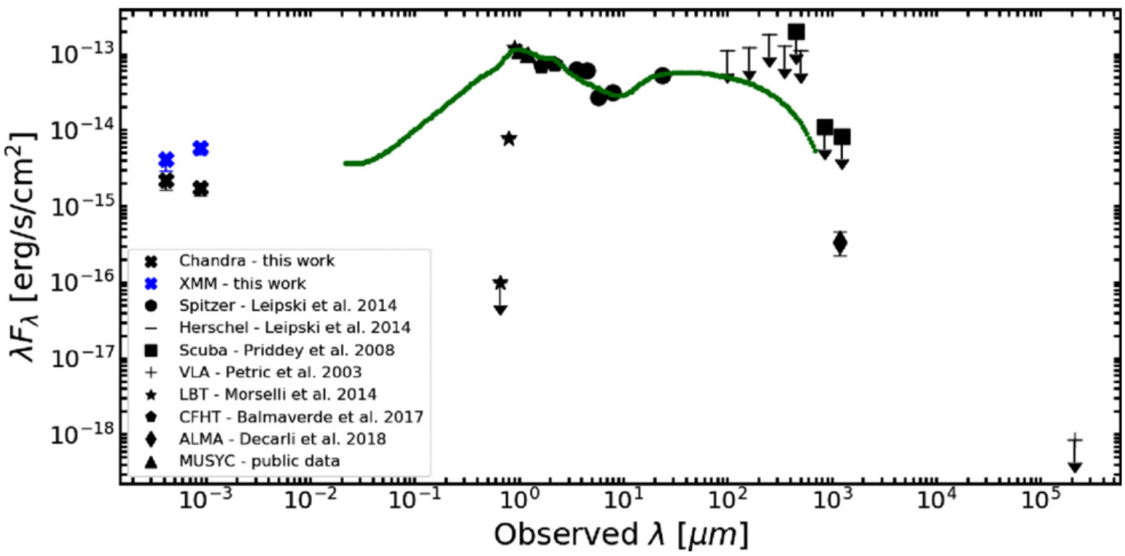

Figure 2.2: Broad-band multi-wavelength SED of SDSS J1030+0524. References to the points are labeled. The combined SED of luminous QSOs at lower redshift is marked by the green curve (Richards et al., 2006). The drop of the flux at $\lambda < 1$ is produced by the Ly-α forest. From Nanni et al. (2018).

In the following years, the field around the QSO has been targeted by numerous multi-band spectroscopic and photometric observational campaigns from the X-ray to the radio band, largely collected as part of a major project[1] led by the Istituto Nazionale di Astrofisica (INAF). A summary of all the data collected so far are reported in Table 2.1, while the field of view (FoV) of the instruments/surveys targeting the so-called J1030 field are shown in the left panel of Fig. 2.3. Among the plenty of data available in the J1030 field, particularly notable is the X-ray ~0.5 Ms *Chandra* observations carried in 2017 (Nanni et al., 2018), that makes this field the fifth deepest extragalactic X-ray survey to date. By comparing the *Chandra* emission of the QSO J1030+0524 with that previously detected by XMM-Newton in 2003, (Nanni et al., 2018) revealed a hardening ($\Delta\Gamma \sim 0.6$) and a dimming ($\times2.5$, see right panel in Fig. 2.1) of its spectrum in a rest-frame time span of 2 years, possibly as a consequence of an intrinsic variation in the accretion rate, even if an absorption event produced by an intervening gas cloud along the line of sight cannot be excluded. On top of the X-ray variability, Nanni et al. (2018) have shown that the broad-band emission of SDSS J1030+0524 is consistent with that of lower-redshift luminous QSOs (see Fig. 2.2). Based on the FIR properties of a sample of high-z QSOs (including

[1] A complete description of the project, including all the available observations and data products, such as spectra, catalogues and images, is available at http://j1030-field.oas.inaf.it/, as well as the list of published results.

SDSS J1030+0524), Decarli et al. (2018) found that SDSS J1030+0524 features a SFR < 100 $M_\odot$/yr, lower than the average SFR of the sample (few hundreds of $M_\odot$/yr). This suggests that SDSS J1030+0524 may be in a more evolved stage than the other luminous QSOs at comparable redshift, and its star formation has been possibly quenched by its feedback.

Nanni et al. (2020) extracted a catalogue of 256 extragalactic X-ray sources down to a 0.5–2 keV flux limit $f_{0.5-2\ keV} = 6 \times 10^{-17}$ erg/cm^2/s, making J1030 an ideal region to search for intrinsically faint or heavily obscured AGN. Exploiting the exceptional multi-wavelength coverage of the J1030 field, Marchesi et al. (2021) derived the photometric (or, where possible, spectroscopic) redshift for 243 of the catalogued X-ray sources. In addition, Peca et al. (2021) derived the redshift for a sub-sample of obscured AGN, based on X-ray spectra. Their redshifts are consistent with the photo-z obtained by Marchesi et al. (2021), when available.

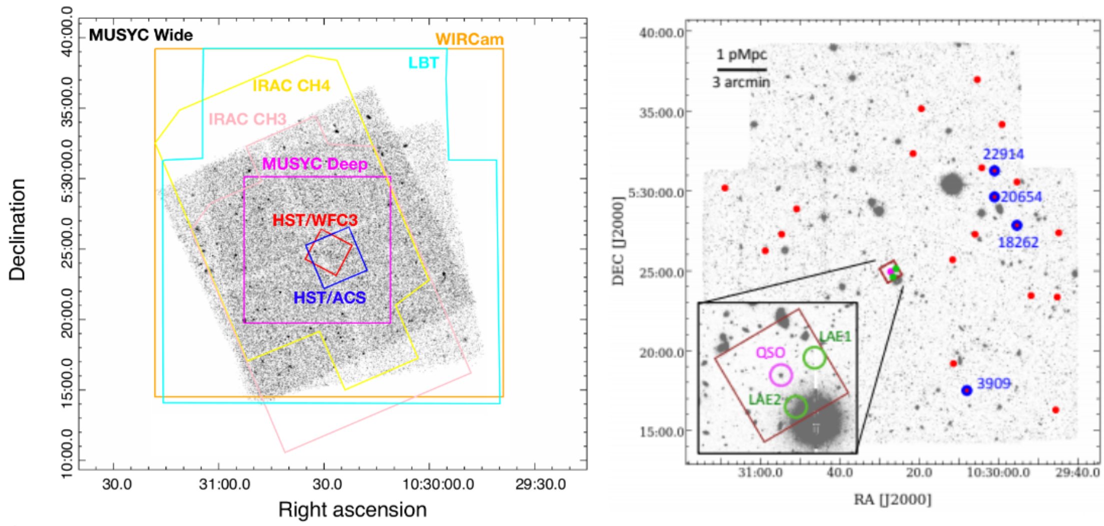

Figure 2.3: *Left:* Smoothed 0.5–7 keV *Chandra* image of the J1030 field. Overlaid in colors are the regions covered by the available photometric surveys/catalogs. From Marchesi et al. (2021). *Right:* LBT/LBC z-band image of the J1030 field, showing the position of $z \sim 6$ LBG candidates (red dots). Spectroscopically confirmed members of the LSS at z=6.3 are marked in blue and labeled with their ID in the multi-band photometric catalogue. Two additional members of the LSS have been discovered in a MUSE field centered on the QSO (see brown square). The position of these two LAEs is indicated by the green circles. The inset shows a zoom of the sky region around the MUSE field. From Mignoli et al. (2020).

The analysis of the large collection of datasets has yielded the discovery of two distinct assembling structures, one around the z=6.3 QSO and one at z=1.7. This makes this field unique, as it can be used to probe two crucial phases of galaxy assembling and evolution: the "cosmic dawn" (z $\geq$ 6, where the first galaxies and LSSs form) and the "cosmic noon" (z ~2, when both star formation and SMBH accretion peak). The first tentative detection of the galaxy overdensity around the QSO at $z = 6.3$ was reported by Stiavelli et al. (2005), based on *i*-*z* color-selected candidates. The possible presence of an overdensity was later confirmed by Kim et al. (2009) and Morselli et al. (2014), through *i*-band dropouts observed with the Hubble Space Telescope (HST) Advanced Camera for Survey (ACS) and the Large Binocular Camera (LBC) at the Large Binocular Telescope (LBT), probing “small scales” of $\sim$1 Mpc around the QSO. Thanks to deep near-IR observations carried out with the Wide-field InfraRed Camera (WIRCam) at the Canada France Hawaii Telescope (CFHT) and Infrared Array Camera (IRAC) aboard *Spitzer* telescope, Balmaverde et al. (2017) selected 21 robust $z \sim 6$ Lyman Break Galaxies (LBG[2]; red dots in the right panel of Fig. 2.3), reinforcing the significance of the candidate overdensity. Finally, Mignoli et al. (2020) reported the spectroscopic confirmation of at least six members of the overdensity, four LBGs (part of the Balmaverde et al. 2017 sample) and 2 Ly-α emitters (LAEs, marked by the blue and green circles in Fig. 2.1, respectively), corresponding to a LSS significance of $>3.5\sigma$.

At $\sim$ 40” South-West from the J1030 field center, a bright radio source is present (NRAO VLA Sky Survey - NVSS, J103023+052426; Condon et al. 1998). Deeper (root-mean-square – rms – sensitivity $\sim$15 μJy) and higher resolution ($\sim$1.5”) Very Large Array (VLA) observations show that the radio source is a FRII RG (Petric et al., 2003). Gilli et al. (2019, herafter G19) estimated a redshift z=1.6987 for this source, which can therefore be considered a HzRG. G19 also unveiled other seven galaxies at the same redshift, showing the HzRG traces a galaxy overdensity. This overdensity is the major subject of this Thesis work, and a comprehensive description of the $z = 1.7$ HzRG and associated overdensity is provided in Sect. 2.1 and Sect. 2.2.

2.1 The $z = 1.7$ HzRG in the J1030 field

The HzRG in the J1030 field and its main morphological features are shown in Fig. 2.4 (white contours and labels). The HzRG features two extended lobes; a bright hotspot is present in the Western lobe (W-lobe), while the presence of a hotspot in the Eastern lobe (E-lobe) is questionable. A relativistic jet connecting the core with the E-lobe is clearly visible. This is interpreted as an evidence that the Eastern jet is the approaching one with respect the line of sight, as often found in FRII galaxies due to the relativistic boosting of the surface brightness (see Fig. 1.4). As discussed in Nanni et al. (2018), the E-lobe and the outer jet of the FRII have a total 1.4 GHz flux density of $S_{1.4\ \mathrm{GHz}} \sim 1.7$ mJy, while the W-lobe is much brighter, with $S_{1.4\ \mathrm{GHz}} \sim 24$ mJy. The core and the inner jet have $S_{1.4\ \mathrm{GHz}} \sim 0.5$ mJy. Overall the source has a 1.4 GHz flux density $S_{1.4\ \mathrm{GHz,\ tot}} \sim 27$

[2]The UV-band includes one of the best known spectral features showed by SFG. The rest-frame wavelength of 912 Å corresponds to the Lyman series limit, below which hydrogen atoms cannot be ionized. This results in a depression of the continuum emission at shorter wavelengths (known as Lyman break) which is due to the fact that the UV radiation from the galaxy star-forming regions is mostly absorbed by the neutral Hydrogen around them. This feature is widely used to select SFG candidate up to z~$6-7$, known as Lyman-Break Galaxies (LBGs, e.g., Steidel et al., 1996; Morselli et al., 2014; Álvarez-Márquez et al., 2016).

Band/Filter	Instrument/Survey	Field of view	Depth (5σ)	Reference/Archive
X-ray - 0.5 – 7 keV	Chandra/ACIS-I	$17' \times 17'$	1.7×10^{-16} erg/cm^2/s	Nanni et al. (2018)
X-ray - 0.3 – 10 keV	XMM	Diameter: $30'$	1.0×10^{-16} erg/cm^2/s	Farrah et al. (2004)
Opt - U, B, V, R, i, z	MUSYC Wide	$30' \times 30'$	$m_{AB} = 25 - 26$	Blanc et al. (2008)
Opt - r, i, z	LBT/LBC	$23' \times 25'$	$m_{AB} = 25, 26, 27.5$	Morselli et al. (2014)
Opt - r, i, z	Subaru/Suprime-Cam	$27' \times 34'$	$m_{AB} = 26 - 28$	Díaz et al. (2014)
Opt - $F775W$ and $F850LP$	HST/ACS	$3.3' \times 3.3'$	$m_{AB} = 27.5$	Stiavelli et al. (2005)
NIR - Y, J	WIRCAM/CFHT	$24' \times 24'$	$m_{AB} = 24$	Balmaverde et al. (2017)
NIR - J, H, K	MUSYC Deep	$10' \times 10'$	$m_{AB} = 23$	Quadri et al. (2007)
NIR - K	MUSYC Wide	$30' \times 30'$	$m_{AB} = 21$	Blanc et al. (2008)
NIR - $F160W$	HST/WFC3	$2' \times 2'$	$m_{AB} = 27.5$	HST archive, D'Amato et al. (2020a)
MIR - 3.6 – 8.0 μm	Spitzer/IRAC	$35' \times 35'$	[3.6] = 22.5	Annunziatella et al. (2018)
MIR 24 μm	Spitzer/MIPS	$\sim 10' \times 16'$	[24] = 19.5	IRSA archive
FIR - 100, 160 μm	Herschel/PACS	$\sim 7' \times 7'$	~10 mJy	IRSA archive; see also Leipski et al. (2014)
FIR - 250, 350, 500 μm	Herschel/SPIRE	$\sim 16' \times 16'$	~30 mJy	IRSA archive; see also Leipski et al. (2014)
FIR - 1.1mm	AzTEC	212.6 arcmin^2	2.6 mJy	Zeballos et al. (2018)
FIR - 1.2mm	ALMA	*FWHM*: $25''$	230 μJy	Decarli et al. (2018)
FIR - 3.0mm	ALMA	$1' \times 2'$	35 μJy	D'Amato et al. (2020a)
Radio - 1.4GHz	VLA	*FWHM*: $30'$	90 μJy	Petric et al. (2003)
Radio - 1.4GHz	JVLA	*FWHM*: $30'$	12.5 μJy	D'Amato et al. (subm., 2021)
Radio - 400, 650 MHz	GMRT	*FWHM*: $80', 40'$	125, 50 μJy	PI Brienza (Observed in 2021)
Radio - 150MHz	LOFAR	*FWHM*: 3°	650 μJy	Brienza et al. (in prep.)

Band	Telescope/Instrument/Mode	Emission line sensitivity (5σ)	Reference
Opt	LBT/MODS/MOS	10^{-17} erg/cm^2/s	Mignoli et al. (2020)
Opt	Keck/DEIMOS/MOS	10^{-17} erg/cm^2/s	Decarli et al. (2019)
Opt	VLT/MUSE/IFU	2.0×10^{-18} erg/cm^2/s	ESO archive - Mignoli et al. (2020)
Opt	VLT/FORS2	6.0×10^{-18} erg/cm^2/s	Mignoli et al. (2020)
NIR	LBT/LUCI/Long Slit	2.0×10^{-17} erg/cm^2/s	Gilli et al. (2019)
mm	Noema	0.5 Jy km/s	Decarli et al. (2019)

Table 2.1: Photometric (*Top*) and spectroscopic (*Bottom*) datasets available for the J1030 field. From left to right: Band, instrument or survey, 5σ sensitivity.

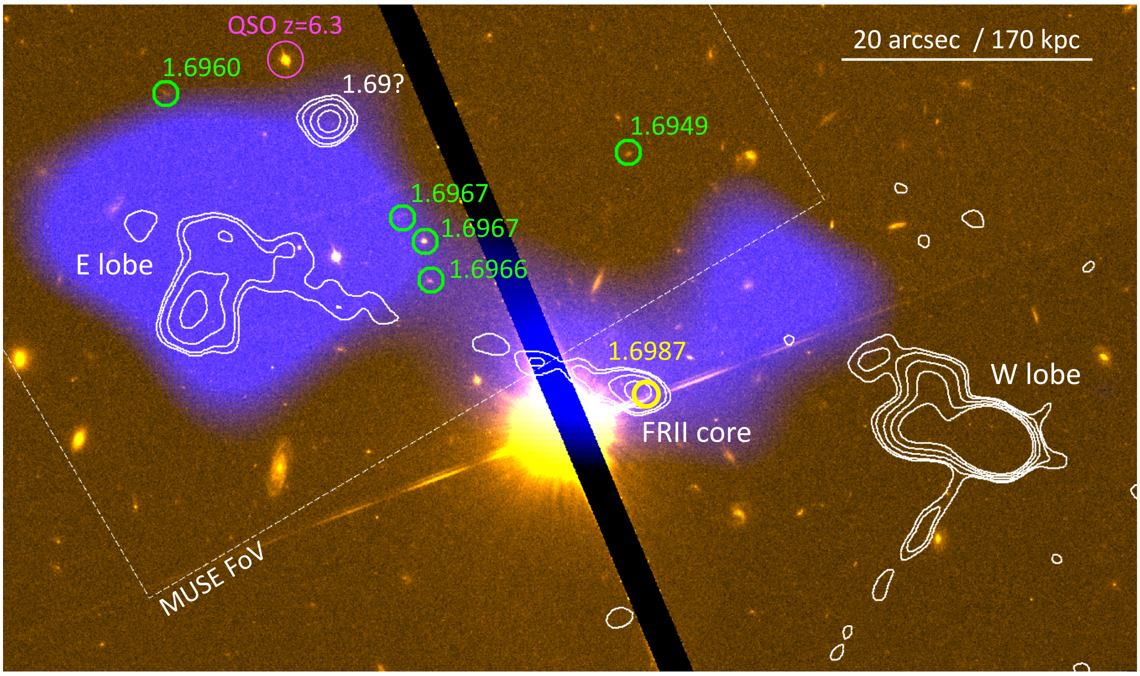

Figure 2.4: HST/ACS $F850LP$ image of the overdensity at $z = 1.7$. Overlaid in white are the VLA radio contours (based on Nanni et al. 2018 re-analysis of the Petric et al. 2003 observations). The main radio morphological features are labeled. Also shown is the *Chandra* smoothed point-source-subtracted image of diffuse X-ray emission (violet; 0.5–7 keV). North is up and east is to the left. The dark strip running across the bright star is the gap between the two ACS CCDs. The MUSE field of view is marked by the dashed white line. The position of the FRII host and its redshift are shown in yellow. Green circles mark MUSE galaxies in the overdensity with their redshifts labeled. An additional radio source may be part of the overdensity (labeled in white). The position of the $z = 6.3$ QSO at the center of the J1030 field is indicated in magenta. From G19.

mJy, very close to the total flux density measured from the lower resolution NVSS image: $S_{1.4\ \mathrm{GHz,\ tot}}$(NVSS) $\sim$ 30 mJy. This source is also present in the 150 MHz TIFR GMRT Sky Survey (TGSS) with a total flux density $S_{150\ \mathrm{MHz,\ tot}}$(TGSS) $\sim$ 164 mJy. By comparing the NVSS and TGSS flux densities an overall spectral index $\alpha \sim 0.76$ is derived. Using this spectral index value we get the following rest-frame radio luminosities: $P_{\mathrm{tot}}(1.4\ \mathrm{GHz}) \sim 4.7 \times 10^{26}$ W Hz^{-1} and $P_{\mathrm{tot}}(150\ \mathrm{MHz}) \sim 2.6 \times 10^{27}$ W Hz^{-1}, which classify this source as a powerful FRII radio galaxy.

From the flux ratio between the jet and counter-jet (R_{jet}) it is possible to obtain a joint constraint of the FRII galaxy inclination angle with respect to the line of sight (θ) and the jet velocity $\beta = v/c$:

$$R_{\mathrm{jet}} = [(1+k)/(1-k)]^{p+\alpha_{\mathrm{jet}}}, \text{ where } k = \beta\cos(\theta), \tag{2.1}$$

where p is the Doppler boost exponent and α_{jet} is the spectral index of the jet. With a measured R_{jet} in the range 1.42 – 1.65, and assuming $\alpha_{\mathrm{jet}} = 0.5$, as typical for local radio-galaxies and one-sided FRII galaxies (Giovannini et al., 2001; Ruffa et al., 2019), and a continuous jet with $p = 2$, G19 derived $k \sim 0.07 - 0.01$. Another constraint on k can be obtained by comparing the observed Doppler boosted power of the FRII core ($P^{\rm obs}_{\rm core}$) with an estimate of the intrinsic (not boosted) core power $P^{\rm int}_{\rm core}$ (Cohen et al., 2007):

$$R_{\rm core} = P^{\rm obs}_{\rm core}/P^{\rm int}_{\rm core} = \delta^{p+\alpha_{\rm core}}, \text{ where } \delta = \sqrt{(1-\beta^2)}/(1-k). \tag{2.2}$$

By combining Eqs. 2.1 and 2.2, we can then derive both β and k and, in turn, the inclination angle $\theta = \arccos(k/\beta)$. An estimate of $P^{int)}_{core}$ can be derived from the correlation $P_{\rm tot}$(408 MHz) - $P^{\rm int}_{\rm core}$(5 GHz) presented by Giovannini et al. (2001), where $P_{\rm tot}$(408 MHz) $\sim 1.2 \times 10^{27}$ W Hz^{-1} is derived from the aforementioned $P_{\rm tot}$(TGSS) and α values. The predicted $P^{\rm int}_{\rm core}$(5 GHz) is therefore $\sim 2.4 \times 10^{24}$ W Hz^{-1}. This value can be compared with the observed power, derived by assuming a flat spectral index $\alpha_{\rm core} = 0$, i.e., $P^{\rm obs}_{\rm core}$(5 GHz) = $P^{\rm obs}_{\rm core}$(1.4 GHz). This provides $R_{\rm core} \sim 0.9 - 1.2$, and, when combining Eqs. 2.1 and 2.2, $\beta \sim 0.4 - 0.5$ and an angle with respect to the line of sight of $\theta \sim 70 - 80$ deg (G19). In other words this source is almost lying on the plane of the sky; after correcting for its inclination its extension is ~600 kpc.

G19 computed the bulk kinetic power of the FRII jet, by assuming it to be proportional to the total radio luminosity of the lobes, and following Willott et al. (1999):

$$P_{\rm jet} = 3 \times f^{3/2} L_{151\ \rm MHz} \quad {\rm ergs}^{-1}, \tag{2.3}$$

where $L_{151\ \rm MHz}$ is the luminosity at 151 MHz and f is a factor that takes in account all the systematic uncertainties on the system geometry and environment, assumed equal to 15 (e.g. Hardcastle, Evans & Croston 2007). This results in $P_{\rm jet} \sim 6.3 \times 10^{45}$ erg/s.

As discussed in G19, the HzRG hosts a Compton-thick AGN (X-ray derived column density N_H~1.5×10^{24}cm^{-2}). Under the assumption that the torus and the radio jets are co-axial, the almost edge-on orientation of the FRII is consistent with the Compton-thick column density derived from the X-rays, in the frame of the unified schemes where the maximum obscuration is expected for an edge-on orientation of the torus.

The absorption-corrected X-ray luminosity of the FR II nucleus is $L_{2-10\ \rm keV}$~1.3×10^{44} erg/s, corresponding to a total luminosity of $L_{\rm bol}$~4×10^{45} erg/s (assuming a bolometric correction of 30, see Marconi et al., 2004), placing the FRII nucleus into the QSO regime. In addition $P_{\rm jet}$ is $\sim 1.5 \times L_{\rm bol}$, as generally found in powerful radio-galaxies (Ghisellini et al., 2014).

2.2 The z = 1.7 HzRG associated overdensity

On the basis of spectroscopic data collected using the Very Large Telescope (VLT) Unit Spectroscopic Explorer (MUSE), G19 reported the discovery of six star-forming galaxies in the redshift range 1.6871 – 1.6967 ($m1$–$m6$ in Table 2.2). These galaxies are distributed

ID (1)	RA(J2000) (2)	DEC(J2000) (3)	$z_{\rm spec}$ (4)
$m1$	$10^h30^m27^s.73$	$+05°24'52''.3$	1.6960 ± 0.0005
$m2$	$10^h30^m26^s.46$	$+05°24'42''.4$	1.6967 ± 0.0004
$m3$	$10^h30^m26^s.34$	$+05°24'40''.5$	1.6967 ± 0.0002
$m4$	$10^h30^m26^s.31$	$+05°24'37''.4$	1.6966 ± 0.0003
$m5$	$10^h30^m25^s.26$	$+05°24'47''.6$	1.6949 ± 0.0004
$m6$	$10^h30^m26^s.42$	$+05°25'07''.1$	1.6871 ± 0.0003
$l1$ (FRII)	$10^h30^m25^s.20$	$+05°24'28''.4$	1.6987 ± 0.0002
$l2$	$10^h30^m20^s.56$	$+05°23'28''.7$	1.6966 ± 0.0004

Table 2.2: (1) Source ID. Sources discovered by MUSE are labeled as m, while sources discovered by LUCI are labeled by l. The $l1$ source correspond to the FRII RG. (2) Source right ascension (RA) and (3) declination (DEC). (4) Spectroscopic redshift of the source.

within a projected distance of ~400 kpc from the FRII galaxy core. The spectroscopic redshift of the FRII host galaxy has been determined through LBT Utility Camera in the Infrared (LUCI) spectroscopy ($l1$ in Table 2.2); thanks to this observation, a seventh galaxy belonging to the overdensity was serendipitously discovered at ~800 kpc distance from the FRII RG ($l2$ in Table 2.2). The five MUSE galaxies closest to the HzRG are shown in Fig. 2.4 (green circles). A sixth MUSE galaxy is located ~40" North of the FRII galaxy, while the LUCI source is located ~1.5 arcmin South-West (both outside the region shown in Fig. 2.4). Based on SED fitting, G19 argued that also the strong radio source Northward from the FRII E-lobe could possibly belong to the overdensity (see white contours in Fig. 2.4, labeled with a photometric redshift ~1.69).

G19 estimated the significance of the overdensity, by comparing the number of the sources detected by MUSE ($N_{\rm src}$=6) and the number of background sources extrapolated by the source redshift distribution of the MUSE field ($N_{\rm bkg}$=0.26). The Poisson probability to observe by chance 6 source within $\Delta z < 0.01$, given $N_{\rm bkg}$, is 3.5×10^-7. Then, the structure (corresponding to an overdensity $\delta_g = N_{\rm src}/N_{\rm bkg} - 1 = 22$) is highly significant. From the overdensity level G19 attempted an estimate of the total mass of the structure, considering that at the observed epoch it is probably far from being virialized. The total mass can be estimated as (Steidel et al., 1998):

$$M_{\rm sys} = \overline{\rho}V(1 + \delta_m), \tag{2.4}$$

where $\overline{\rho}$ is the average density of the Universe at $z = 1.7$, V is the volume and $\delta_m = \delta_g/b$ is the dark matter overdensity, where $b = 2$ is the *bias* factor, as appropriate for the redshift and SFR of the MUSE galaxies (Lin et al., 2012). As for the the volume, since the system is not settled yet, galaxy infall motions can cause an underestimation of the true volume $V_{\rm true}$. The apparent volume $V_{\rm app}$ is assumed to be a box of $0.5\times0.5\times6.3 = 1.6$ proper Mpc^3, that encompasses the 6 galaxies found by MUSE. $V_{\rm true} = V_{\rm app}/C$, where the

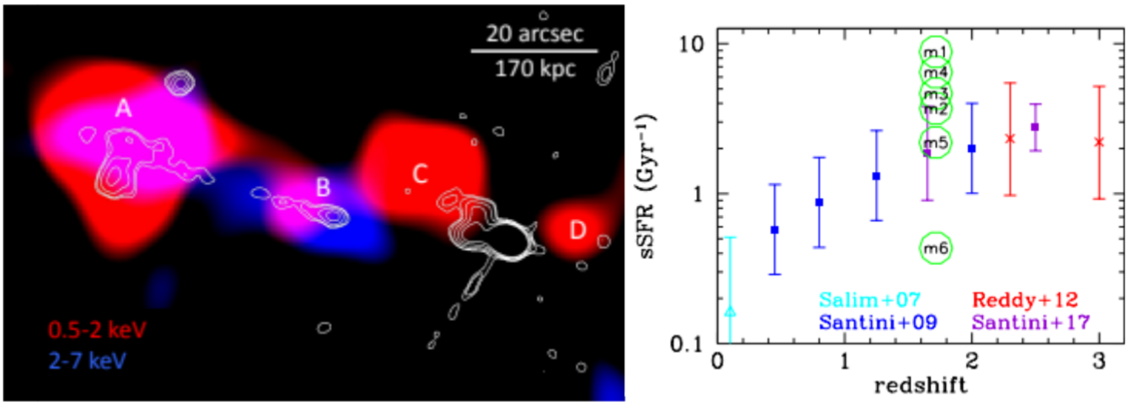

Figure 2.5: *Left:* Point-source subtracted and smoothed Chandra X-ray composite image, showing the X-ray diffuse emission (down to $\sim 2.5\sigma$) around the FRII galaxy (white contours). The red (blue) channels show the soft (hard) emission. *Right:* specific star formation rate of MUSE galaxies $m1 - m6$ (green circles) plotted against the specific star formation rate vs. redshift relation derived for field galaxies with $\log(M_*/\mathrm{M}_\odot) = 9.5 - 10$ (from different samples as labeled). From G19.

correction factor $C < 1$ can be estimated following the procedure of Cucciati et al. (2014), and solving numerically the following system of two equations where the variables are C and the true δ_m:

$$\begin{cases} 1 + b\delta_m = C(1 + \delta_g) \\ C = 1 + f - f(1 + \delta_m) \end{cases} \tag{2.5}$$

where in the second equation (derived by Steidel et al. 1998) the factor $f(z) \approx \Omega_m(z)^{0.6}$ (Lahav et al., 1991). Solving the system gives $V_{\mathrm{true}} = 3.9$ Mpc^3 and $\delta_m = 3.7$, leading to a system mass $M_{\mathrm{sys}} = 1.5 \times 10^{13}$ M$_\odot$. For comparison, considering a velocity dispersion observed along the line of sight of ~325 km/s, a virial mass of $M_{\mathrm{sys}} = 2.5 \times 10^{13}$ M$_\odot$ can be derived (Lemaux et al., 2012; Cucciati et al., 2018). The discovery of additional members of the overdensity and a more precise estimate of the structure mass are presented as part of this Thesis, based on new ALMA band 3 observations of the CO(2→1) emission line (see Chapter 3).

2.2.1 Origin of the diffuse X-ray emission

Thanks to the available deep *Chandra* observations, Nanni et al. (2018) unveiled the presence of several spots of X-ray diffuse emission around the FRII galaxy (shown in violet in Fig. 2.4). The X-ray diffuse emission is composed by both soft and hard components (labeled as A, B, C and D in the left panel of Fig. 2.5). The most significant is spot A, which overlaps with the E-lobe of the FRII radio galaxy. The widest component in spot A is soft, with the hard component being mainly distributed along the jet. The emission in spot A is well fitted by a power-law with $\Gamma \sim 1.6$. By fitting it with a thermal model it returns a 2σ lower limit to the gas temperature of ~5 keV. The steep Γ and the high temperature values point towards a mixture of thermal emission (dominating in the soft band), and non-thermal IC-CMB emission, dominating in the hard band. If this is the case, the gas temperature and luminosity ascribed to the thermal emission could be lower that those resulting from the fit. While a $\Gamma \sim 1.6$ is consistent with a IC-CMB origin of the X-ray emission, Nanni et al. (2018) noted that no X-ray diffuse emission was detected in the FRII W-lobe, despite it being 6× brighter than the E-lobe.

To better probe the IC-CMB scenario a prediction of the expected X-ray flux density was derived by exploiting the radio band observations. Under the assumption of "equipartition" (i.e., the energy in the radio lobe is equally distributed between the relativistic particles and the magnetic field), it is possible the calculate the equipartition magnetic field $B_{\rm eq}$ (Miley, 1980):

$$B_{\rm eq} = 5.69 \times 10^{-5} \left[\frac{(1+k)}{\eta} (1+z)^{3+\alpha} \frac{1}{\theta_x \theta_y \, l \sin^{3/2}\phi} \times \frac{S_{obs}}{\nu_{obs}^{-\alpha}} \frac{\nu_2^{0.5-\alpha} - \nu_1^{0.5-\alpha}}{0.5-\alpha} \right]^{2/7} \mathrm{G}, \qquad (2.6)$$

where the various parameters have the following meaning and values, accordingly to measurements and standard prescriptions (G19): $\theta_x = 10$ arcsec, $\theta_y = 12$ arcsec are the angular diameters of the Eastern radio lobe, assuming an elliptical geometry; $k = 1$ is the energy ratio between heavy particles and electrons; $\eta = 1$ is the volume filling factor of the emitting region; $l = 90$ kpc is the path length through the source along the line of sight, assumed to be equal to that in the x direction of the ellipse; $S_{obs} = 1.7 \times 10^{-3}$ Jy is radio flux density of the region at the observed frequency $\nu_{obs} = 1.4$ GHz (see Sect. 2.1); $\alpha = 0.8$ is the radio spectral index in the range between the lower ($\nu_1 = 0.01$ GHz) and upper ($\nu_1 = 100$ GHz) cut-off frequencies of the radio spectrum (based on the measured $\alpha \sim 0.76$ between 150 MHz and 1.4 GHz, see Sect. 2.1); $\phi = 90°$ is the angle between the magnetic field and the line of sight. This yields $B_{\rm eq} \sim 5\ \mu$G, which is consistent with values usually reported in literature (Isobe, Seta & Tashiro, 2011). From $B_{\rm eq}$it is possible to predict the X-ray flux density at 1 keV associated with the IC-CMB process:

$$f_{1\ \rm keV} = \frac{(5.05 \times 10^4)^{\alpha} C(\alpha) G(\alpha) (1+z)^{3+\alpha} S_{obs} \nu_{obs}^{\alpha}}{10^{47} B_{\rm eq}^{1+\alpha} \nu_X^{\alpha}}, \qquad (2.7)$$

where $\alpha = 0.8$, and $C(\alpha)$ and $G(\alpha)$ are mild functions of α, assumed constant in this case: G(α)=0.5 and C(α) = 1.15×10^{31} (see, e.g., Harris & Grindlay 1979 and Pacholczyk 1970). Assuming a power-law with $\Gamma = 1.8$, the derived $f_{1\ \rm keV}$ translates into an integrated flux $F_{0.5-7\ \rm keV} \sim 60\times$ lower than that derived from the *Chandra* observations. Even considering a population of low-energy electrons entirely filling the volume observed in the X-ray spot A, the derived IC-CMB flux density will still be an order of magnitude lower than that observed. It is however worth mentioning that in the last years an increasing number of studies have shown that the magnetic fields in FRII RGs can be up to a factor of 3 lower that that derived under equipartition conditions (e.g. Croston et al., 2005;

Kataoka & Stawarz, 2005; Migliori et al., 2007; Isobe, Seta & Tashiro, 2011; Ineson et al., 2017; Turner, Shabala & Krause, 2018). In fact, magnetic field $\times 3$ lower than B_{eq} would be sufficient to justify the observed X-ray flux in spot A as originated by the IC-CMB process. It remains difficult to explain, though, why no X-ray emission is detected around the brighter Western lobe.

As for the other X-ray spots, spot B coincides with the FRII galaxy nucleus and jet base. It mostly features hard X-ray emission, which is well described by a non-thermal flat power-law arising from the inner part of the jet, with a $\Gamma = 0.06$ (G19). As for the other spots, the soft C and D components are well fitted by a thermal model with $kT \sim 0.6$ keV and $kT \sim 0.7$ keV, respectively (G19). It is interesting to note that spot C is located at the end of the the FRII galaxy W-lobe, suggesting a possible interaction between the ICM and the lobe.

2.2.2 HzRG-induced feedback on multiple galaxies

As discussed in G19, four of the discovered overdensity members ($m1 - m4$ in Table 2.2) lie in an arc-like shape at the edge of the X-ray diffuse emission around the eastern lobe of the FRII (spot A, see Fig. 2.4). These sources feature the highest SFR (20 – 60 $M_{\odot}$/yr) among all the MUSE galaxies. In addition, they display a specific SFR (sSFR) $\sim 2-5\times$ higher than the one of the other sources, and significantly above the sSFR-redshift relations available in the literature (Fig. 2.5, right panel). Under the assumption that spot A is mostly of thermal origin, G19 proposed that the diffuse X-ray emission originates from an expanding bubble of hot gas in the ICM, shock-heated by the energy injected by the FRII radio galaxy. In this scenario, the expanding bubble compresses the cold gas in the surrounding MUSE galaxies, consequently enhancing their star-formation.

As demonstrated by G19, the jet is powerful enough to deposit the observed amount of energy into spot A. By assuming a temperature and density consistent with the fit of spot A X-ray spectrum ($kT \sim 5$ keV and $n \sim 4\times 10^{-3}$ cm^{-3}), G19 derived the total thermal energy stored in the medium, i.e. $E_{th} \sim 7 \times 10^{60}$ erg. By assuming that at least half of P_{jet} goes into the heating of ICM, as recently found in hydro-dynamical simulations (Bourne, Sijacki & Puchwein, 2019) and as supported by theoretical arguments (Weaver et al., 1977), G19 estimated that it would take only $E_{th}/(P_{jet}/2) = 70$ Myr for the jet to deposit that amount of energy into the E-lobe surrounding medium, a time which is consistent with low-frequency observations of local radio-galaxies (Harwood et al., 2017).

If the X-ray emission of component A is due to a bubble of gas that is shock-heated by the FRII jet, one may wonder whether this bubble is still expanding or whether it has stalled at the observed boundary. G19 derived the ratio between the internal pressure of the bubble (P_{hot}) and the pressure of the surrounding medium (P_{cold}), by assuming that the diffuse cold gas shares the same physical conditions as observed in the Spiderweb proto-cluster (§ 1.3.3), and found that $P_{hot}/P_{cold} > 10^4 - 10^5$, depending on whether the cold gas is in the molecular or atomic form. G19 verified that after 70 Myr, the bubble radius has expanded to 117 kpc, in excellent agreement with the measured size of spot A of the diffuse X-ray emission ($\sim$120 kpc radius). After this time, the velocity of the expanding bubble shock front is $\sim$1.2 kpc/Myr (see Eq. 18 of Gilli et al. 2017); given the size of $m1 - m4$ (4 – 5 kpc), it would take only few Myr for the shock front to cross the galaxies, nicely consistent with the time-scale of the starburst episodes inferred by their UV-emission. All this nicely fits in a positive feedback scenario, where the shocks are responsible for the molecular gas compression and SFR enhancement.

As a final remark, G19 noted that the positive feedback scenario may also hold if the diffuse X-rays seen in spot A are produced by IC-CMB rather than by shock-heated gas. By conservatively assuming the state of minimum energy $U_{\rm hot} = (7/3)U_{\rm b}$, where $U_{\rm hot} = B^2/(8\pi)$ is the magnetic field energy, a total non-thermal pressure $P_{\rm hot} = U_{\rm hot}/3$ is obtained, that is 260 times higher than $P_{\rm cold}$. Thus, in both the thermal or non-thermal scenarios, the hot gas bubble is still expanding and the positive feedback scenario stands. This is the first time positive AGN feedback was observed on multiple galaxies[3]. Additional signatures of positive feedback are presented as part of this Thesis, based on new deeper radio observations (see Chapter 4).

[3]A NASA press release reporting about this discovery is avaliable here: https://chandra.harvard.edu/press/19_releases/press_112619.html.

Chapter 3

The ALMA view of the the $z = 1.7$ over-density: evidence for a massive proto-cluster assembly

In order to detect new gas-rich members of the structure at $z = 1.7$ presented in Sect. 2.2 and possibly unveil the presence of large gas reservoirs around known members, we obtained ALMA observations of a $\sim$4 arcmin^2 region around the HzRG, targeting the CO(2→1) transition line (redshifted to Band 3 at $z = 1.7$). In this Chapter we present these observations, which resulted in a number of CO detections, including the FRII host galaxy, which was also detected in the continuum at 3 mm. We then exploit the broad-band Optical/IR coverage of the J1030 field, to build and fit the broad-band SED of the FRII host galaxy, study its physical properties, and investigate the origin of the continuum emission detected by ALMA. The results presented in this Chapter are published in D'Amato et al. (2020a, 2021).

3.1 ALMA observations and calibration

We performed a three-pointing mosaic observation in ALMA Band 3 (84 – 116 GHz) during Cycle 6 (project ID: 2018.1.01601.S, PI: R. Gilli). The 2×4 GHz spectral windows (*spws*) cover the 84.1 – 87.7 GHz and 96.1 – 99.9 GHz spectral ranges. Each *spw* is sampled by 1920 channels, each with 976.5 kHz width, corresponding to 3.7 km/s at the mean frequency of the *spws*. The observations consist of six $\sim$50.5 min execution blocks carried on the 18$^{\text{th}}$ (two execution blocks), 28$^{\text{th}}$ (one execution block) and 31$^{\text{th}}$ (three execution blocks) of December 2018. The quasars J1058+0133 and J1038+0512 served as flux/bandpass and phase calibrator, respectively. We performed the data calibration and flagging via the calibration pipeline (version 42254) of the Common Astronomy Software Applications (CASA) package (version 5.4.0-70; McMullin et al., 2007). The pipeline procedure automatically flags bad data and performs the calibration; it also produces several diagnostic plots that are useful to identify possible calibration failures and discern the need of additional flagging. After the inspection of both the diagnostic plots and calibrated data, the calibration resulted to be satisfactory.

3.2 Image cube analysis

3.2.1 Line imaging

As shown in G19, the proto-cluster members can be found at large projected separation (~800 kpc for *l*2) and large radial distance (-1300 km/s ≈ 7 Mpc for *m*6) from the FRII radio-galaxy. Then, to detect new members of the overdensity, we produced data-cubes of the entire field of view (FoV) of the observations, and we included all channels from −3000 km/s to +3000 km/s with respect to the FRII spectroscopic rest-frequency 85.426 GHz (see Table 2.2). The continuum was estimated over all the *spws* excluding this frequency range, and then fit with a polynomial and subtracted from the data-set, running the UVCONTSUB CASA task. Line imaging was then performed running the TCLEAN task of CASA on the continuum-subtracted data-set. We produced cubes with smoothed velocity channels of 100 km/s, 70 km/s, 50 km/s, 30 km/s and 15 km/s, in order to find the best trade-off between spectral resolution and signal-to-noise ratio (S/N) per channel. The robustness Briggs weighting was set to 0.5, corresponding to a restoring beam full width at half maximum (*FWHM*) of 2.161×1.655 arcsec. We found that the 30 km/s cube allows us to resolve the relevant kinematic features of the detected sources, and still has enough S/N per channel to properly constrain the spectral parameters. Therefore, the source detection and analysis reported in this work refer to the 30 km/s data-cube. The achieved rms sensitivity in the central region of the mosaic is ~150 μJy/beam at the median frequency of the cube.

3.2.2 Noise and S/N cubes

We performed the source detection, moments, and spectrum analysis by exploiting the S/N-cube. In order to produce it, we firstly generated a noise-cube, in which each pixel has been assigned a value which is the one of the rms calculated from a region around the same pixel in the original data-cube. The pixels in maps originated from interferometric datasets are not independent due to the synthesized beam convolution, and the local noise at a given position is evaluated as the pixel rms in a region around that position. Such a region should be large enough to provide a robust rms value, and small enough to provide the most accurate local rms, since the noise varies across the image. We explored regions of 5, 10 and 15 times the synthesized beam area, finding that a 10-beams area represents the best trade-off between a good tracing of the local noise variations and a good statistics to obtain a robust rms value. For each pixel, the rms is calculated to convergence in an iterative process that excludes the pixels above 3 × rms in the surrounding 10-beams region. This allows us to remove from the noise map the emission contribution of the sources present in the original data-cube. The S/N-cube is then calculated as the ratio between the data-cube and the noise-cube. The S/N cube allows us to take properly into account local noise variations when proceeding with the source detection.

3.2.3 Source detection

We developed from scratch a code that aims at blindly detecting emission lines win the S/N-cube, on the basis of spectral, spatial and S/N threshold criteria. Firstly, the code scans each pixel of each channel (i.e., each spaxel) of the S/N-cube looking for a given number N_{ch} of contiguous channels (named "sliding window"), which are all above a given S/N threshold S/N_w. Then, the code sums the S/N of the N_{ch} channels in each selected sliding window. A candidate detection is then associated with the pixel with the highest S/N in the sliding window with the highest sum of S/N over its N_{ch} channels, only if the pixel has $S/N > 3$. This procedure allows us to select the line candidates, avoiding to include spectral noise spikes. Secondly, the code rejects all the candidate detections with a number of spatially-contiguous detected pixels lower than a given number N_{px}. Finally, to assess the reliability of the detected sources ("positive detections"), we run the code on the negative S/N-cube (i.e. a cube in which each pixel has the same value but inverted sign with respect to the original S/N-cube). This way we obtain the "negative detections", which provide us with information about the incidence and S/N distribution of spurious detections. In principle, as reliability criterion, we can reject all the positive detections with a S/N lower than the maximum S/N obtained for the negative detections, for any given set of parameters (i.e., N_{ch}, S/N_w and N_{px}). However, in order to minimize the possibility to include spurious sources in our analysis, we decided to adopt a very conservative approach, and consider as reliable only the detections obtained with a parameter set for which no negative detections are found.

We performed the source search for all possible combinations of S/N_w= 1.5, 2.0, 2.5, 3.0; $N_{ch} = 2, 3, 4$ (corresponding to 60, 90 and 120 km/s, respectively); and $N_{px} = 2, 3, 4$. The maximum values of N_{ch} and N_{px} quoted above (i.e., the most stringent adopted criteria) are such that the code recovers only the brightest sources and no additional detections are found. The searching area was cropped to the >50% response area of the observations, in order to exclude the field outskirts where the noise increases very steeply and possibly produces artifacts. Then, among all combinations of S/N_w, N_{ch} and N_{px}, we excluded those for which we obtained at least one negative detection.

We found that the code is highly reliable (i.e., no negative detections found) down to $S/N_w = 2.0$ for $N_{ch} = 4$ (120 km/s) and down to $S/N_w = 2.5$ for $N_{ch} = 3$ (90 km/s), requiring at least $N_{px} = 3$. After the reliability step, only four detections remain for all the possible parameter combinations.

We detected the FRII host galaxy ($a0$) and three new members of the overdensity ($a1$, $a2$, $a3$). All our secure ALMA detections have optical counterparts in HST images. The source positions are reported in Table 3.1, along with their HST H-band magnitude H_{AB} and color index $z-H$. The 1-σ uncertainty on the source position is set to $0.5 \times \langle FWHM \rangle \times \mathrm{S/N}^{-1}$, where $\langle FWHM \rangle$ is the mean of the major and minor $FWHM$ of the beam and the S/N is that of the peak pixel (Papadopoulos et al., 2008). The ALMA sources are also indicated in the r-g-b HST image shown in the left panel of Fig. 3.1 (red circles), along with the MUSE sources (green circles), named as in G19 (see also Sect. 2.2). In the right panel of Fig. 3.1 we show cut-outs of the r-g-b HST image centered on the ALMA detected sources.

The strongest detection is $a0$, which is also the only spatially-resolved source, and unveils the presence of a large molecular gas component surrounding the radio-galaxy host. The redshift of the FRII host was already known from LUCI spectroscopy (this source is also indicated as $l1$ in Fig. 3.1 and Table 2.2). Hence there is no doubt the detected line is the redshifted CO(2→1) transition. For $a1$, $a2$ and $a3$, this is less obvious as we do not have independent estimates of the source redshifts. However, based on the CO luminosity functions derived by the ASPECS project (Decarli et al., 2019) and on the sensitivity of our observations, we estimate that the number of line interlopers expected in the observed volume is only of 0.09 sources, a factor 2.8 lower than the expected number of CO(2→1) emitters (0.25); it is also interesting to note that the probability to observe three CO(2→1) transitions in the observed volume would be very low in a blank field (P = 2×10^{-3}, assuming a Poisson distribution). Thus, the presence of a known overdensity at z = 1.7 in the field, naturally accounts for the observed number of lines as CO(2→1) transitions.

As a final remark, we note that we did not detect any diffuse molecular gas emission distributed on scales of several tens kpc and embedding the central proto-cluster region, as instead observed in the Spiderweb proto-cluster (see § 1.3.3). We note that the maximum recoverable scale (MRS) of our observations is 10 arcsec, corresponding to ~85 kpc. However, we also remind the reader that the molecular gas diffuse component in the Spiderweb proto-cluster has been detected through: *i*) ALMA observations at comparable resolution but higher MRS (~33") than ours (Emonts et al., 2018), targeting the high-J transition line CO(4-3); *ii*) Australia Telescope Compact Array (ATCA) observations of the CO(1-0) emission line tapered to ~6 arcsec resolution and a MRS of several arcmin (Emonts et al., 2016). Hence, we cannot exclude that dedicated observations may possibly unveil the presence of a diffuse molecular gas component at large scales also in the J1030 proto-cluster.

3.2.4 Spectral analysis and moments

Using the S/N-cube, we derived a 3σ-cube from the original data-cube, by masking all the pixel having S/N < 3. We firstly computed the 3σ integrated flux map (moment 0) and

ID	RA(J2000)	DEC(J2000)	H_{AB}	$z-H$
(1)	(2)	(3)	(4)	(5)
$a0$	$10^h30^m25^s.16 \pm 0^s.13$	$+5°24'28''.69 \pm 0^s.13$	22.43	2.3
$a1$	$10^h30^m24^s.84 \pm 0^s.23$	$+5°24'31''.68 \pm 0^s.23$	23.25	2.2
$a2$	$10^h30^m24^s.58 \pm 0^s.31$	$+5°24'25''.97 \pm 0^s.31$	23.54	3.1
$a3$	$10^h30^m22^s.65 \pm 0^s.23$	$+5°24'37''.08 \pm 0^s.23$	23.20 (21.7)	2.3 (3.2)

Table 3.1: (1) Source ID. (2) Source right ascension (RA) and (3) declination (DEC). (4) HST H-band (typical 1-σ uncertainty: 0.02) and (5) $z-H$ color index (typical 1-σ uncertainty: 0.25). We note that $a3$ appears as a blend of two galaxies at the high spatial resolution of the HST images (see Fig. 3.1, right panel). In this case we report the magnitude and color index of the source corresponding to the bulk of CO emission (that to the East) and in parentheses the values of the other source (that to the West).

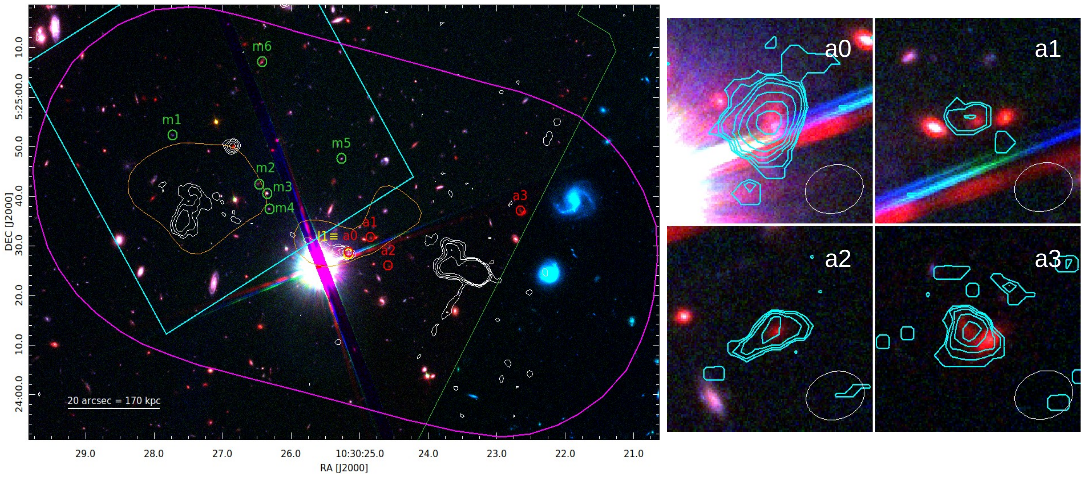

Figure 3.1: *Left:* Composed r-g-b image of the field around the FRII radio-galaxy. Red, green and blue channels are the HST F160w, F850lp and F775w filters. Green and red circles mark the MUSE ($m1$-$m6$) and ALMA ($a0$-$a3$) sources, respectively. Source $a0$ (the FRII host) corresponds to the LUCI source $l1$, marked in yellow. A second LUCI source, $l2$, is located ~1.5 arcmin southeast from $a0$, outside the image. VLA contours at 1.4 GHz are overlaid in white, starting from a ~3σ flux density threshold and increasing with a $\sqrt{3}$ geometric progression (Petric et al., 2003; Nanni et al., 2018). The orange contours marks the ~2.5σ level of the diffuse X-ray emission (0.5-7 keV) discussed in G19. The green solid polygon delimits the region covered simultaneously by all HST filters. The solid magenta line and cyan box are the ALMA >50% response area and MUSE FoV, respectively. The white horizontal line at the bottom left indicates the angular and physical scale. *Right*: ~7×7 arcsec^2 (~60×60 kpc^2) cut-outs of the composed HST r-g-b image, centered on the ALMA detected sources (named as labeled). The cyan contours represent the 3σ-moment 0 map of our observations (see Sect. 3.2.4), starting from a ~3σ flux density threshold and increasing with a $\sqrt{3}$ geometric progression. The white ellipse in the bottom right corners represents the restoring beam. From D'Amato et al. (2020a).

velocity map (moment 1) for all the sources in the whole frequency range covered by the cube. Then, we extracted the integrated spectra of each source from the original data-cube in a region drawn considering all the contiguous pixels around the peak position in the 3σ-moment 0. In this process, we exploited the moment 1 maps to reject the pixels whose velocities were largely inconsistent with the observed line velocity range (i.e., displaced by > 1000 km/s). We measured the flux density per channel (i.e. the spatially-integrated surface brightness) for the resolved source $a0$ and the mean per channel for all the other (unresolved) sources. As for the error per channel, we measured the mean of the rms in the same region drawn from the noise-cube.

We performed a Markov chain Monte Carlo (MCMC) fit of the integrated spectra by exploiting the EMCEE Python package (Foreman-Mackey et al., 2013). We used two Gaussian components for $a0$ and $a3$, which clearly show a double peaked feature in the spectrum. For $a1$ and $a2$ only one Gaussian component was used for the fit. It is worth noticing that $a2$ likely features two peaks, but we preferred to use a single-component fit due to the low S/N per channel. However, for checking purposes, we also performed a two-components fit, finding that the frequency-integrated flux of the one- and two-components fits are in excellent agreement ($\sim 1\sigma$). The spectra and their fits are shown in Fig. 3.2, as a function of the radial velocity offset (increasing with redshift) from the detected line center.

In Table 3.2 we show the results of the spectral fitting. We report the CO(2→1) redshift $z_{\rm CO}$, and the *FWHM* and peak flux density $S_{CO(2-1)}$ of each component (columns 2-7). The integrated flux $I_{CO(2-1)}$ (column 8) has been calculated as the sum of the contributions from the two components, that is:

$$I_{CO(2-1)} = \frac{1}{2}\sqrt{\frac{\pi}{\ln 2}} \times (S_{CO(2-1),red} \times FWHM_{red} + S_{CO(2-1),blue} \times FWHM_{blue})\ \text{Jy km/s}. \quad (3.1)$$

The line luminosity (column 9) is then derived as:

$$L'_{CO(2-1)} = 3.25 \times 10^7 \nu_{obs}^{-2} (1 + z_{\rm CO})^{-3} D_L^2\, I_{CO(2-1)}\ \text{K km s}^{-1}\ \text{pc}^2, \quad (3.2)$$

where ν_{obs} is the line observed frequency (in GHz) and D_L is the luminosity distance (in Mpc) (Solomon, Downes & Radford, 1992). We note that all the newly detected overdensity members are at lower redshift with respect to source $a0$ (the FRII host), and that the CO-derived redshift of $a0$ is consistent within 1σ with the spectroscopic redshift measured with the LUCI, i.e. $z_{opt} = 1.6987 \pm 0.0002$ (G19).

The spectral fitting results were exploited to constrain the velocity range (set to 1.5 × FWHM of the Gaussian model, corresponding to $\sim 3.5\sigma$ from the peak), within which we derived the moments from the 3σ-cube. This range is indicated by the brown dashed vertical lines in the spectra shown in Fig. 3.2. The contours of the 3σ-moment 0 map are shown in cyan in the right panel of Fig. 3.1, superimposed to r-g-b HST cutouts centered in each source.

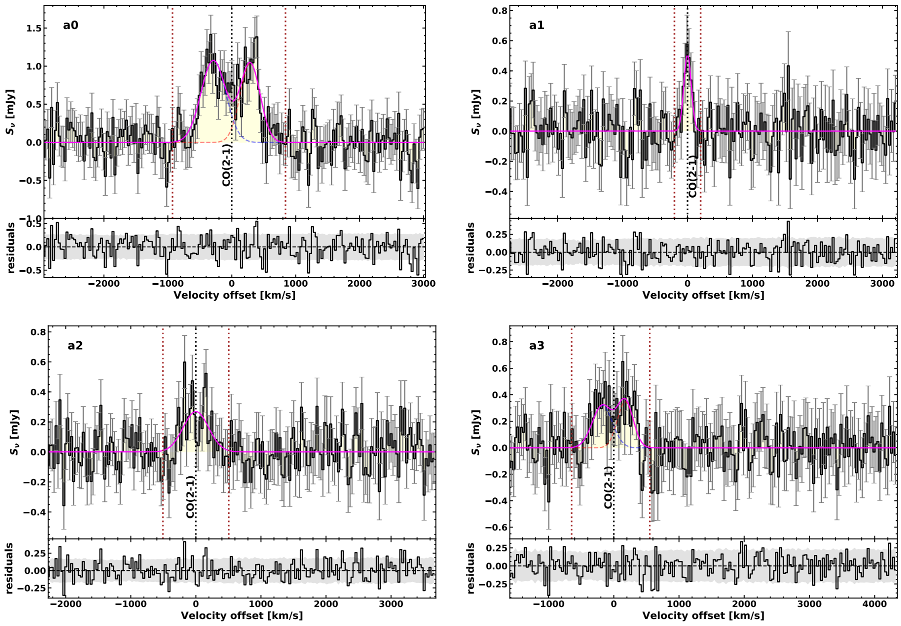

Figure 3.2: ALMA spectra of the four detected sources (channel width of 30 km/s). For each spectrum, the top panel shows the data extracted from the data-cubes (black solid line) as a function of the radial velocity offset (increasing with redshift) from the detected line center. The grey bars represent the relative error per channel measured on the noise-map. The solid magenta line marks the total model, i.e. the sum of the two components (red and blue dashed lines). The rest-frame zero-velocity is set to the central frequency of the fitted line (black dotted vertical line). For two-component fits, the central frequency of the line is set to the mean of the two components' central frequencies. The brown vertical dotted lines delimit the velocity range within which we computed the moments. For the two-component fits, the range spans from the low-velocity side of the blue-shifted component to the high-velocity side of the red-shifted one. The source ID is reported in the top left corner. Bottom panels: residuals when subtracting the total model from the data. The grey shaded region shows the rms per channel, indicating the 1σ range. From D'Amato et al. (2020a).

3.2.5 The molecular gas properties of the overdensity members

Following Eq. 1.1, we derive the molecular hydrogen mass of the ALMA detected sources as:

$$M_{H_2} = \alpha_{CO}\, L'_{CO(1-0)}\ \mathrm{M}_{\odot}. \tag{3.3}$$

In order to rescale our measured $L'_{CO(2-1)}$ to $L'_{CO(1-0)}$, we need to assume a ratio $r_{21} \equiv L'_{CO(2-1)}/L'_{CO(1-0)}$ (see § 1.2.1). This value spans from ∼0.5 for the Milky Way (MW, Weiß, Walter & Scoville, 2005) to ∼1.0 for quasars and starburst nuclei (Carilli & Walter, 2013). In normal main-sequence high-z SFG, a mild sub-thermal excitation is typically found for the CO(2→1) transition. Thus, we assume $r_{21} = 0.76$, as reported by Daddi et al. (2015) on the basis of the analysis performed on a sample of a near-IR (NIR)-selected SF disk galaxies at z=1.5 (this is also a compromise between the values for MW-like galaxies and quasars/starbursts). The similarity of the gas properties in these objects with those of the

<table>
<tr><th>ID</th><th>z_{CO}</th><th>$FWHM_{red}$ [km/s]</th><th>$FWHM_{blue}$ [km/s]</th><th>$S_{CO(2-1),red}$ [mJy]</th><th>$S_{CO(2-1),blue}$ [mJy]</th><th>$I_{CO(2-1)}$ [Jy km/s]</th><th>$L'_{CO(2-1)}$ [10^9 K km s^{-1} pc^2]</th><th>M_{H_2} [10^{10} ($\frac{0.76}{r_{21}}\frac{\alpha_{CO}}{4.3}$) M$_\odot$]</th></tr>
<tr><td>(1)</td><td>(2)</td><td>(3)</td><td>(4)</td><td>(5)</td><td>(6)</td><td>(7)</td><td>(8)</td><td>(9)</td></tr>
<tr><td>$a0$</td><td>$1.6984^{+0.0003}_{-0.0004}$</td><td>$366^{+124}_{-89}$</td><td>$452^{+104}_{-90}$</td><td>$1.04^{+0.13}_{-0.11}$</td><td>$1.07^{+0.11}_{-0.10}$</td><td>$0.88^{+0.06}_{-0.06}$</td><td>$33.6^{+2.2}_{-2.3}$</td><td>$19.3^{+0.1}_{-0.1}$</td></tr>
<tr><td>$a1$</td><td>$1.6966^{+0.0001}_{-0.0001}$</td><td colspan="2">$133^{+43}_{-33}$</td><td colspan="2">$0.51^{+0.14}_{-0.13}$</td><td>$0.07^{+0.02}_{-0.01}$</td><td>$2.6^{+0.7}_{-0.6}$</td><td>$1.5^{+0.4}_{-0.4}$</td></tr>
<tr><td>$a2$</td><td>$1.6925^{+0.0004}_{-0.0005}$</td><td colspan="2">$447^{+97}_{-81}$</td><td colspan="2">$0.28^{+0.05}_{-0.06}$</td><td>$0.12^{+0.03}_{-0.03}$</td><td>$4.7^{+1.1}_{-1.1}$</td><td>$2.7^{+0.6}_{-0.6}$</td></tr>
<tr><td>$a3$</td><td>$1.6864^{+0.0006}_{-0.0006}$</td><td>$304^{+237}_{-127}$</td><td>$365^{+201}_{-156}$</td><td>$0.33^{+0.10}_{-0.12}$</td><td>$0.32^{+0.13}_{-0.12}$</td><td>$0.22^{+0.04}_{-0.03}$</td><td>$8.4^{+1.5}_{-1.3}$</td><td>$4.8^{+0.8}_{-0.7}$</td></tr>
</table>

Table 3.2: Summary of the fit results and molecular masses. (1) ID of the source. (2) Redshift of the line, set equal to the mean of the blue- and red-shifted components for the two-component fits. (3) and (4) *FWHM* of the red- and blue-shifted component, respectively. (5) and (6) Flux density peak of the red- and blue-shifted components, respectively. (7) Integrated flux of the line. (8) Line luminosity. (9) Molecular gas mass. For $a1$ and $a2$ we performed a single-component fit.

MW also argues for a Galactic α_{CO} (Dannerbauer et al., 2009). Thus, in order to derive the gas mass, we assume $\alpha_{CO} = 4.3$ (Bolatto, Wolfire & Leroy, 2013). We note, however, that $a0$ hosts a powerful AGN that likely boosts molecular gas excitation around it, resulting in a higher r_{21} and a lower α_{CO}. In order to assess the impact of the AGN on the overall molecular gas conditions, we analysed the FRII source in more detail. This is the only ALMA source of our sample which is (marginally) resolved. We derived the angular size performing a 2-D Gaussian fit of the 3σ-moment 0 integrated intensity with the CASA task IMFIT. We obtained a major axis $a = 3.2 \pm 2.0$ arcsec and a minor axis $b = 2.0 \pm 1.6$ arcsec, corresponding to intrinsic (deconvolved from beam) physical sizes of 27 ± 17 kpc and 17 ± 13 kpc respectively, at $z = 1.7$. Despite the large uncertainties, these sizes likely unveil the presence of molecular gas that extends on large scales around the FRII nucleus. This possibly suggests that the AGN effect may be negligible, when considering the overall gas content. A lower α_{CO} is, however, still possible for this galaxy, if one considers that it is actively star forming (see below for an estimate of its SFR), and star formation induces heating processes and increases the excitation of the gas (Papadopoulos et al., 2012). This is the reason why we make explicit the dependencies on the assumed r_{21} and α_{CO}, when the derived gas masses are reported in Table 3.2 (see column 9). All the detected sources host a massive reservoir of molecular mass ($\sim 1 - 5 \times 10^{10}$ M$_\odot$), with the FRII host galaxy reaching $\sim 2 \times 10^{11}$ M$_\odot$. This is one of the most massive gas reservoirs known to date for a HzRG in an overdensity (see § 1.3.2 and § 1.3.3).

It is interesting to note that we did not detect any CO emission from the previously known members discovered through MUSE spectroscopy (see G19 and Sect. 2.2). This is likely the consequence of selection effects, since MUSE preferentially detects unobscured sources while ALMA typically detects obscured ones. However, based on the ALMA sensitivity limits at the source positions, and assuming a line width of 225 km/s (i.e., the mean of the fit components for $a1$, $a2$ and $a3$), we derive 3σ molecular mass upper limits for the MUSE sources, spanning the range $M_{H_2} \leq 2.8 - 4.8\times 10^{10}$ M$_\odot$. These limits do not rule out the presence of large amounts of molecular gas in the MUSE sources as well.

All the ALMA-detected sources show very red optical counterparts (column 5 of Table 3.1), indicating that they are dusty star-forming systems. We can provide an estimate of the source SFRs by means of the Schmidt-Kennicutt (SK, Kennicutt, 1998) relation between the SFR density and the gas surface density (in $M_\odot/pc^2$):

$$\Sigma_{SFR} = 2.5 \times 10^{-4} \Sigma_{gas}^{1.4} \ M_\odot \ yr^{-1} \ kpc^2. \tag{3.4}$$

For the unresolved sources, we assume for the size of the star-forming regions a range between a lower limit given by the optical size derived from the HST/F160w image (i.e. $\sim$ 46, 47 and 90 kpc^2 for $a1$, $a2$ and $a3$, respectively) and an upper limit given by the synthesized beam of the CO observations. This yields SFRs from ~5 – 50 $M_\odot$/yr to ~20 – 100 $M_\odot$/yr. We note that $a3$ is associated with a blend of two optical sources (HST image, Fig. 3.1), possibly ascribed to a major merger. The bulk of the CO emission seems to correspond to the fainter optical source. Conservatively, in the optical size calculation, we considered only the source corresponding to the bulk of the CO emission. For the resolved FRII host galaxy, we follow a similar approach, and assume a star-forming region size ranging from the size of the optical rest-frame emission (derived from the HST/F160w image, ~110 kpc^2) to the size of the molecular gas emission ($\pi \times a/2 \times b/2$, ~360 kpc^2). This yields ~200 – 600 $M_\odot$/yr (another estimate of the SFR will be presented in § 3.3.3).

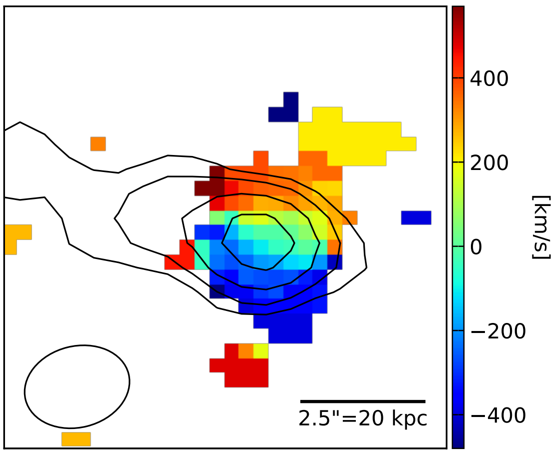

Figure 3.3: FRII host galaxy ($a0$) line velocity map (moment 1), with respect to the line central frequency of the fit marked by the vertical black dotted line in Fig. 3.2). North is up and east to the left. The black open ellipse is the restoring beam. The VLA contours, drawn as in Fig. 3.1, are shown in black. From D'Amato et al. (2020a).

From the size of the FRII source and its mass, we attempted an estimate of the ISM column density ($N_{\rm H,ISM}$) along the line of sight, and compared it with that derived from the X-ray spectrum ($N_{\rm H,X}\sim 1.5 \times 10^{24}$ cm^{-2}; G19), to evaluate the contribution of the host galaxy to the nuclear obscuration. Due to the large uncertainty on the source size, the inclination angle and disk thickness of the molecular gas are unconstrained (i.e., the relative errors are ≥1). We therefore decided to derive an upper limit for the column density assuming an edge-on disk (i.e., the inclination angle between the rotation axis and the line of sight is $\theta = 90°$, consistent with the value of $\theta \sim 70° - 80°$ found by G19; see Sect. 2.1). As for the geometry, we assumed a thin disk having the diameter equal to a and constant height equal to 1 kpc, similar to the typical scale-height of high-z spirals and chain galaxies (Elmegreen & Elmegreen, 2006). We found $N_{\rm H,ISM} \sim 5.5 \times 10^{23}$ cm^{-2}. This column density is considerable, suggesting that the ISM may contribute significantly to the total nuclear obscuration measured in the X-rays, in addition to a small, parsec-scale absorber, possibly arranged in a torus-like geometry around the nucleus (as postulated in the Unified Schemes; Urry & Padovani, 1995, see also § 1.1.1). Under the assumption that the radio jet and the torus are co-axial, the high $N_{\rm H,X}$ value measured strengthens the findings of G19 regarding the edge-on orientation of source. From the velocity map in Fig. 3.3 we observe a velocity gradient that points toward a structure that is rotating perpendicularly to the radio-jet (shown by the 1.4 GHz VLA black contours), at least in projection. This seems to indicate that the inner accretion disk (and torus) and the galaxy-scale disk have a common rotation axis. However, existing 3D modeling of local radio-galaxies (Verdoes Kleijn & de Zeeuw 2005; Ruffa et al. 2019) show that the relative inclination angle between the jet and the (sub-)kpc molecular (and/or dust) disks can vary over a wide range of values, and that a fully axis-symmetric scenario may be too simplistic. In the moment 1 map we also notice two peculiar kinematical features (northwest and southeast from the nucleus), which appear inconsistent with rotation, and possibly associated with non-circular motions. Further observations at higher resolution and S/N are needed to unveil the nature of these features.

The large molecular gas reservoir, coupled with the high SFR and stellar mass (derived through SED-fitting in § 3.3.3), and with the high radio-to-X-ray luminosity (see Sect. 2.1), all significantly larger than that of the other members, point towards a scenario where the FRII is a BCG progenitor, caught during an active phase of super massive black hole and host galaxy growth, likely induced by the extremely gas-rich environment. In addition, the source is located at the center of the spatial distribution of the known members of the overdensity (see Fig. 3.1). We note that the FRII radio galaxy redshift is higher than the one of all the other members, featuring a velocity offset of ~200 km/s from the velocity distribution peak (see Fig. 3.4). In other words the FRII galaxy is not centered with respect to the velocity distribution of the structure. However, due to the peculiar motions of the sources within the structure, it is difficult to securely translate the velocity distribution along the line of sight in a radial distance distribution. HzRGs are known to be signposts of proto-clusters and are commonly considered the best candidates for BCG progenitors (see Miley 1980 and § 1.3.2). However, HzRGs identified as proto-BCG are not always located at the center of the redshift distribution of the proto-cluster members. For example, Venemans et al. (2007) present a sample of proto-clusters associated with HzRGs, and report the case of TN J1338–1942, a system composed by 37 members at $z = 4.1$: the system has a velocity dispersion of 260 km/s, whereas the HzRG associated with the proto-BCG is shifted by 440 km/s from the dynamical center. For comparison, our FRII galaxy is only at ∼200 km/s from the distribution peak, while the velocity dispersion of the structure is much larger, i.e. 440 km/s (see §3.2.6). Moreover, we note that we discovered so far only 11 members of the structure, which is likely much richer (as also indicated from a recent photometric redshift analysis, Peca et al. 2021). If this is the case it is possible that the current redshift distribution is biased and not representative of the whole system.

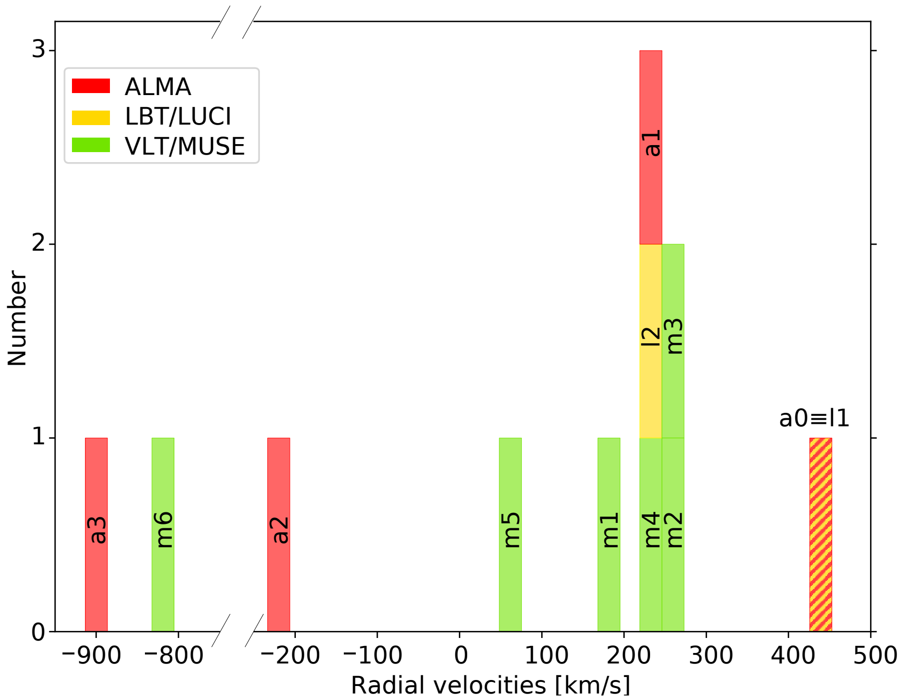

Figure 3.4: Velocity distribution of all the known members of the overdensity with respect to the mean redshift z=1.694, color coded by the discovery instrument. The velocity bins are 30 km/s wide, equal to the mean uncertainty of the sources' redshift. *a*0 and *l*1 correspond to the same source, the FRII galaxy. From D'Amato et al. (2020a).

3.2.6 Proto-cluster mass and evolution

The mean redshift of the system (including all the known members) is $\bar{z} = 1.694 \pm 0.001$. The velocity distribution of the galaxies with respect to the mean redshift is shown in Fig. 3.4. From the overall velocity distribution we derive a line of sight velocity dispersion exploiting the *gapper* method, originally presented by Wainer & Thyssen (1976) and firstly suggested by Beers, Flynn & Gebhardt (1990) as a valid method to estimate the velocity dispersion of galaxies in clusters (see also Cucciati et al. 2018). Given a set of $i = 1, \ldots, n$ galaxies, each having a velocity offset Δv_i from $\bar{z}$, we can define the gaps as $g_i = \Delta v_{i+1} - \Delta v_i$, where $i = 1, \ldots n - 1$. By defining a set of Gaussian weights as

$w_i = i(n-i)$, we can calculate the velocity dispersion as:

$$\sigma_{\rm v} = \frac{\sqrt{\pi}}{n(n-1)} \sum_{i=1}^{n-1} w_i\, g_i, \tag{3.5}$$

from which we derive $\sigma_{\rm v}$~440 km/s.

Given the velocity dispersion, we can derive the virial mass of the system following the procedure of Cucciati et al. (2018):

$$M_{sys,vir} = \frac{3\sqrt{3}\sigma_{\rm v}^3}{\alpha\ 10\ G\ H(z)} \tag{3.6}$$

where G is the gravitational constant, $H(z)$ is the Hubble parameter, and α is the ratio between the radius within which the density is 200 times the critical density (R_{200}) and the virial radius R_v. For consistency we assume $\alpha = 0.93$ as in G19, derived following the procedure presented by Cucciati et al. (2018) (see also Lemaux et al. 2012). From Eq. 3.6 we derive $M_{sys,vir}$~6×10^{13} $M_\odot$, a factor 2.4× higher than that derived from G19 on the basis of the velocity dispersion inferred by the MUSE sources alone (~325 km/s, see Sect. 2.2). Considering that the system is probably far from being virialized, we provide a second estimate of the mass, based on simple considerations on the overdensity. From the MUSE galaxy overdensity, located eastward of the FRII, G19 derived $M_{sys,MUSE} \gtrsim 1.5 \times 10^{13}$ $M_\odot$ (see Sect. 2.2). Based on the ALMA source positions, we can infer that the system extends on similar areas on both sides of the FRII host. Under the minimal hypothesis of eastward and westward overdensities being the same, we can derive $M_{sys} \gtrsim 2 \times M_{sys,MUSE}$, that is $M_{sys} \gtrsim 3 \times 10^{13}$ $M_\odot$.

We note that the most massive dark matter halo is likely assembling around the FRII (i.e. the proto-BCG). Considering that the ratio between the stellar mass of the central galaxy in a halo and the halo mass is found to be at most ~2.5% at z~2 (Behroozi, Wechsler & Conroy, 2013), and that the FRII host stellar mass is M_*~3.7×10^{11} $M_\odot$ (see § 3.3.3), we derive a halo mass of $\gtrsim 1.5 \times 10^{13}$ $M_\odot$. On the basis of cosmological simulations, Chiang, Overzier & Gebhardt (2013) have studied the expected evolution of the most massive halo of a cluster progenitor as a function of redshift (Fig. 3.5, left panel). The estimated FRII halo mass places our system among those that would evolve into a $z = 0$ cluster of at least ~$1.4 - 3 \times 10^{14}$ $M_\odot$. Furthermore, Chiang, Overzier & Gebhardt (2013) presented a correlation between galaxy overdensity profiles and the future cluster masses (Fig. 3.5, right panel). By assuming again that the ALMA and MUSE galaxy overdensities are similar (i.e. δ_g ~ 7.4; G19), we find that, in a volume similar to that observed by ALMA (~15 Mpc^3), our system at z~2 will likely evolve into a cluster of ~1×10^{15} $M_\odot$ at $z = 0$.

The progenitor of such a massive structure is expected to extend for several physical Mpc at high redshifts (see Fig. 1.8), and, in fact, we note that for ~10 of the 256 X-ray selected AGN in the ~17×17 arcmin^2 *Chandra* image of the field we measured a

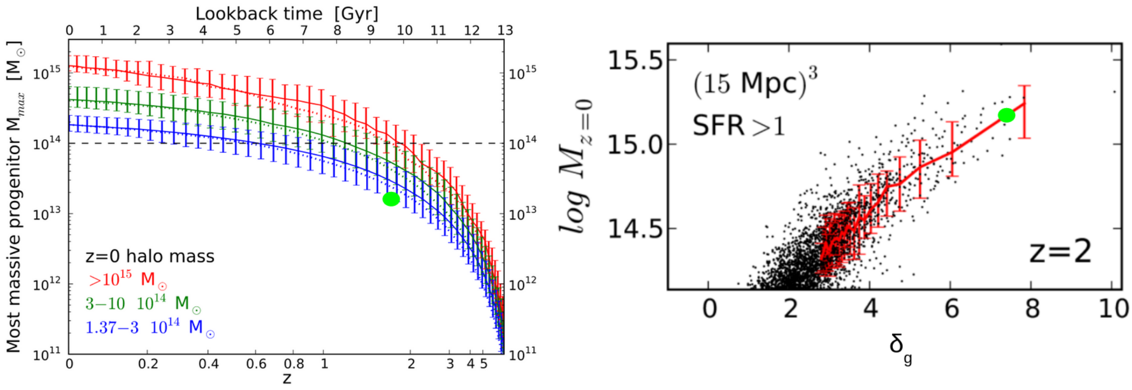

Figure 3.5: *Left*: Evolution of the most massive halo mass as a function of redshift, color-coded by the final cluster mass, as labeled in the figure. Results are based on WMAP1 (solid) and WMAP7 (dotted) simulations. The lines and error bars indicate the medians and 1σ error. The horizontal dashed line marks the final mass threshold (10^{14} $M_\odot$) above which a structure is considered a cluster. *Right*: Correlation between the galaxy overdensity δ_{gal} at $z = 2$, and the $z = 0$ descendant cluster mass $M_{z=0}$, calculated for a volume of 15 Mpc^3 and considering galaxies with SFR > 1 $M_\odot$/yr. In both panels the green dot marks the position of our object. Adapted from Chiang, Overzier & Gebhardt (2013).

photometric redshift consistent with $z = 1.7$ (Peca et al., 2021; Marchesi et al., 2021), suggesting that the entire structure extends on scales of $> 4 - 5$ Mpc from the FRII RG.

3.3 A proto-BCG caught at the peak of its stellar mass building

In this Section we exploit the J1030 field exceptional multi-wavelength coverage to improve on the estimate of the basic physical parameters of the FRII RG (such as e.g. SFR, stellar mass, AGN bolometric luminosity) through SED fitting.

3.3.1 Broadband Optical/IR photometry

The FRII optical/IR emission is located in proximity to a bright star, hence archival photometry (Table 2.1) suffers from contamination in several bands, especially at short wavelengths. Thus, the FRII host galaxy photometry has been re-analyzed in several bands. The measured fluxes and their uncertainties are reported in Table 3.3, as well as the observing instruments and original references. The re-analyzed bands are indicated in column 4.

3.3.2 ALMA continuum emission

The two 4 GHz ALMA spectral windows (84.1 – 87.7 GHz and 96.1 – 99.9 GHz) were used to produce a continuum map. In § 3.2.6 we showed that the proto-cluster members can be found across a wide velocity range (see Fig. 3.4). Thus, in order to avoid any

λ [μm] (1)	S_ν [μJy] (2)	Instrument (3)	Reference (4)
0.9	1.6 ± 0.2	HST/ACS	Stiavelli et al. (2005) (reanalyzed)
1.2	3.6 ± 0.7	CFHT/WIRCam	Balmaverde et al. (2017) (reanalyzed)
2.1	16 ± 2	CTIO/ISPI	Quadri et al. (2007) (reanalyzed)
3.5	36 ± 7	Spitzer/IRAC	Annunziatella et al. (2018) (reanalyzed)
4.5	58 ± 12	Spitzer/IRAC	”
5.7	100 ± 20	Spitzer/IRAC	”
7.8	76 ± 15	Spitzer/IRAC	”
23.5	620 ± 62	Spitzer/MIPS	IRSA archive
105.4	7655 ± 3274	Herschel/PACS	Leipski et al. (2014)
169.5	< 30000	Herschel/PACS	”
246.7	33400 ± 9800	Herschel/SPIRE	”
348.7	43600 ± 12600	Herschel/SPIRE	”
495.3	36100 ± 15000	Herschel/SPIRE	”
1120.5	2500 ± 500	AzTEC	Zeballos et al. (2018)

Table 3.3: Photometric data-points used to perform the SED fitting. (1) Observing wavelength. (2) Observed flux density. (3) Observing instrument. (4) Reference publications, where we specify whether the data have been re-analyzed.

possible contamination from line emission, we performed the continuum imaging after excluding all channels in a range of ±1500 km/s from the mean redshift of the proto-cluster ∼1500 km/s) around the mean redshift of the structure ($\bar{z}$ = 1.694). The imaging was performed with the TCLEAN CASA task in multi-frequency synthesis (*mfs*) mode, resulting in a image at an observed-frame frequency of 92.04 GHz. We used a Briggs weighting scheme with robustness parameter equal to 0.5, corresponding to a restoring beam with a major (minor) axis of 1.92 (1.50) arcsec. The average rms within the >50% response area of the observations is ∼9 μJy. The continuum emission blanked at 3σ level is shown in Fig. 3.6. Two sources have been detected at 3.3 mm: the FRII core and the Western hot spot. We will discuss the origin of the core emission in § 3.3.4.

3.3.3 SED fitting of the proto-BGC

We modeled the SED of the FRII host galaxy by using the fitting code originally presented by Fritz, Franceschini & Hatziminaoglou (2006) and improved by Feltre et al. (2012). The code fits the data, simultaneously accounting for three different components: stellar emission, modeled by means of simple stellar populations (SSPs); reprocessed emission from the dusty torus surrounding the AGN; and emission by the cold dust of the host galaxy that is heated by starburst activity. The fitting code and the libraries used to model the SED are the same ones adopted by Circosta et al. (2019). In addition, we performed a second SED fitting with the same models except for the cold dust contribution, which is now fitted with a simple gray-body model with β = 2, which generally provides a

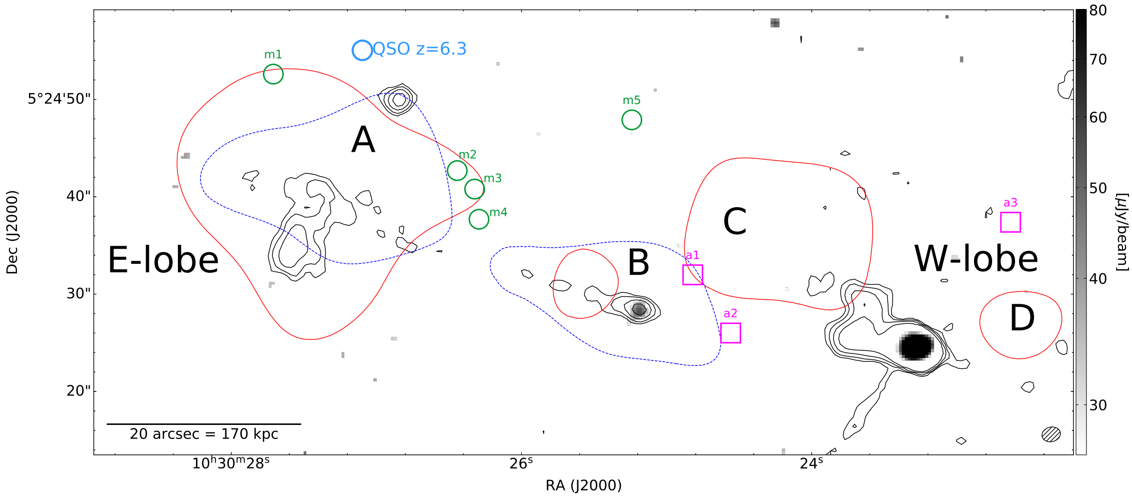

Figure 3.6: ALMA continuum emission at 92.04 GHz, blanked at the 3σ level. The black contours indicate the VLA contours at 1.4 GHz, starting from a $\sim 3\sigma$ flux density threshold and increasing with a $\sqrt{3}$ geometric progression (see Sect. 2.1). Blue (dashed) and red (solid) contours indicate the 2σ hard and soft X-ray diffuse emission, respectively. The four major components of such emission are labeled in black (A–D; see § 2.2.1). The positions of five of the sources discovered by MUSE ($m1 - m5$) are indicated by the green circles (a sixth source is located outside the image, $\sim$45 arcsec north-east from the FRII core). The positions of the proto-cluster members discovered by ALMA ($a1 - a3$) are marked by the magenta boxes. The Eastern and Western lobes are labeled as E-lobe and W-lobe, respectively. The light blue circle indicates the $z = 6.3$ QSO (at the center of the J1030 field). The solid black line at the bottom-left corner indicates the angular and physical scale, while the dashed ellipse at the bottom-right corner is the restoring beam of the ALMA image. Adapted from D'Amato et al. (2021).

very good description of the dust component for both high-z, gas-rich-obscured AGN (see Conley et al. 2011; Fu et al. 2012; Riechers et al. 2013; Gilli et al. 2014) and local gas-rich starburst galaxies (Rangwala et al. 2011). In both fits, we excluded the ALMA 3 mm data point, due to the uncertain origin of the core 3 mm emission (thermal or synchrotron, see § 3.3.4). In Fig. 3.7 we report the SED of the FRII host galaxy and the fitting model (black solid line), as well as the three emission components of the fit. The left panel shows the SED fitting using the cold dust template, while the right panel shows the SED fitting where the dust emission has been modeled using the gray-body. The reduced χ^2 is equal to 1.2 in the first case and equal to 1.0 in the second case.

From the SED fitting we estimate the AGN bolometric and total FIR ($8 - 1000\ \mu$m) luminosities, as well as the stellar mass. The uncertainties for the derived parameter values are based on the error analysis of Circosta et al. (2019), who take into account all acceptable solutions within 1σ confidence level (i.e. within a given range of $\Delta\chi^2$), obtained by varying the fitting parameters and using different fitting codes (see Section 5.2 of Circosta et al. 2019 for caveats and details). Such fiducial errors are of the order of 20% for the luminosities and of 30% for the stellar mass. The AGN contribution in the 8–1000 μm range is significantly higher (24%) for the gray-body model fitting than

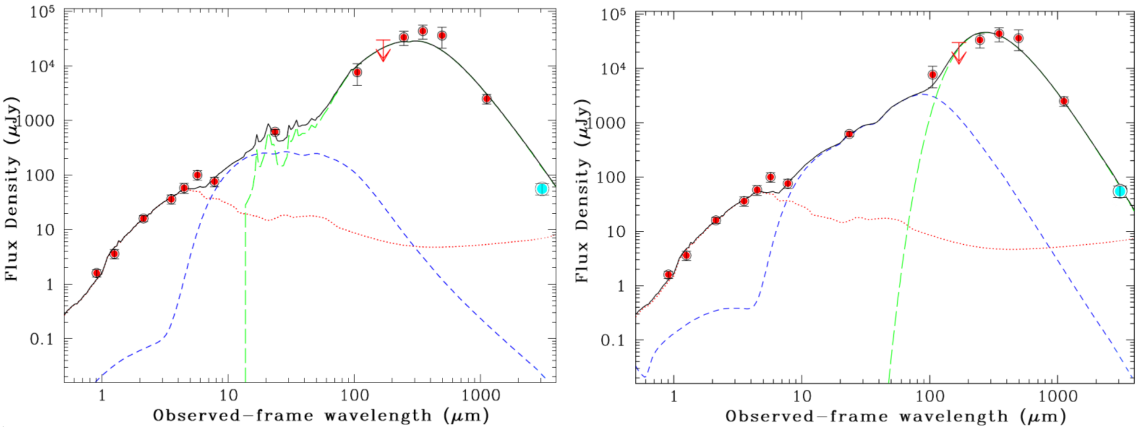

Figure 3.7: SED fitting of the FRII host galaxy. Photometric points are marked by the filled red circles, while the total fitting model is indicated by the solid black line. In both panels the ALMA point is not included during the fitting and is marked by the filled cyan circle. *Left*: The model includes three components: stellar emission (indicated by the red dotted line), the reprocessed emission of the dusty torus surrounding the AGN (blue dashed line), and emission by the cold dust of the host galaxy, heated by starburst activity (green dashed line). *Right:* same as the left panel, except for the cold dust template that has been substituted by a gray-body model with $\beta = 2$. From D'Amato et al. (2021).

for the dust-template fitting (3.1%). The AGN contribution derived from the gray-body model fitting is more consistent with what is expected for Type II heavily obscured AGN such as our FRII galaxy. Once the AGN contribution is subtracted, the FIR luminosities ($L_{8-1000\ \mu\mathrm{m}} \sim 3 \times 10^{12}\ \mathrm{L}_\odot$) derived from the two fitting methods agree within ~10%, i.e. well within the 1σ uncertainties. As a consequence also the SFRs derived by exploiting the L_{FIR} – SFR linear calibration presented by Kennicutt (1998) are in agreement within the errors (SFR~570–630 $\mathrm{M}_\odot$/yr). This SFR range is consistent with the upper end of the range evaluated from the molecular gas through Eq. 3.4 ($\sim 200 - 600\mathrm{M}_\odot$/yr; see § 3.2.5).

As for the AGN bolometric luminosity, we obtain fully consistent values ($\mathrm{L}_{\mathrm{bol,\ AGN}} \sim 1.1 - 1.5 \times 10^{46}$ erg/s) from the two SED fitting methods. Adopting, as bolometric corrections, the values derived by Duras et al. (2020, see also Lusso et al. 2012) from a large samples of AGN spanning seven dex in luminosity, we predict an intrinsic 2–10 keV luminosity of $L_{2-10\mathrm{keV}} \sim 3.2 - 3.8 \times 10^{44}$ erg/s, i.e. a factor of ~2.5 – 3 higher that the one estimated by G19 by fitting the X-ray spectrum. Given the large uncertainties in Duras et al. (2020) relation and in the correction for the column density applied by G19, we can conclude that the AGN luminosity derived from the SED-fitting is broadly consistent with the one derived from the X-ray spectrum.

In summary, the two adopted SED fitting methods result in consistent (1σ) AGN bolometric luminosity, FIR luminosity, stellar mass and SFR. Given the slightly better $\chi^2 = 1.0$ we report here the values derived from the SED fitting with the gray-body model: $L_{\mathrm{bol,\ AGN}} \sim 1.1 \times 10^{46}$ erg/s, $L_{8-1000\ \mu\mathrm{m}} \sim 3.7 \times 10^{12}\ \mathrm{L}_\odot$ (24% of which is ascribed to the AGN), stellar mass $M_* \sim 3.7 \times 10^{11}\ \mathrm{M}_\odot$ and SFR = 570 $\mathrm{M}_\odot$/yr. The high sSFR = 1.5 ± 0.5 Gyr^{-1} derived for the FRII host galaxy classifies this object as a starburst galaxy when compared with other SFG at the same redshift (Schreiber et al., 2015), implying that the proto-BCG is currently being observed during the brief phase (few 10^8 yr, Lapi et al. 2018) of its major stellar mass building. Indeed, we note that the derived SFR implies that the molecular gas reservoir measured in § 3.2.5 will be depleted in $\sim 3.5 \times 10^8$ yr. Moreover, assuming that the BH is accreting with an efficiency $\eta = 0.3$ (as assumed by G19, and as generally assumed for BHs powering jetted AGN, see Blandford & Znajek 1977; Ghisellini et al. 2014), from the bolometric luminosity, we derive an accretion rate for the SMBH of $\dot{M} = L_{\rm bol,\ AGN}/(\eta c^2) \approx 0.6$ M$_\odot$/yr.

3.3.4 Origin of the continuum emission at 3.3 mm

The measured 3mm flux density of the FRII core is 55 ± 9 μJy. This measurement is nicely in agreement with the flux density expected from dust thermal emission, when considering the best fit, i.e. the one obtained using the gray-body model (1σ). However, the measured flux density is inconsistent at a 3σ level with the expected one for the dust-template fit, which is 2.4× higher. Given the best χ^2 and the more plausible AGN fraction of the gray-body model (§ 3.3.3), we favour a scenario where thermal emission from the cold dust in the ISM is at the origin of the observed flux density.

To further check this conclusion, we compare the observed 3mm flux density with the one expected from synchrotron emission. By exploiting the stellar mass- and redshift-dependent $L_{8-1000\ \mu\rm m} - L_{1.4\ \rm GHz}$ relation recently presented by Delvecchio et al. (2021), we derive a SFR-driven observed-frame flux density $S_{1.5\ \rm GHz,\ SFR} \sim 90$ μJy. This value is well below the one measured in our new 1.5 GHz JVLA map[1], i.e. $S_{1.5\ \rm GHz} = 315 \pm 25$ μJy, confirming that the flux density at 1.5 GHz is dominated by the AGN. If we subtract $S_{1.5\ \rm GHz,\ SFR}$ from the measured $S_{1.5\ \rm GHz}$, and we assume a synchrotron spectral index $\alpha = 0.7$[2], we derive an expected synchrotron emission at 3 mm $S_{3\ \rm mm,sync} = 13$ μJy. This value is a factor > 4 below the 3mm flux density measured in our ALMA map (55 μJy), supporting a scenario in which the dust is primarily responsible for the observed flux density at 3 mm. However, we cannot rule out some contribution from synchrotron emission, when considering the large uncertainties on all the involved quantities and relations.

[1] The JVLA map will be presented in Chapter 4. It features a factor of 1.5 better resolution and a factor of 10 better sensitivity with respect to the previous VLA observations. The higher resolution in particular allows us to derive a more robust flux density for the FRII core.

[2] This value can be considered intermediate between the flatter values typically observed at the jet base and the steeper ones typically observed at very high frequencies, due to the fast ageing of energetic electrons (see Giovannini et al. 2001; Ruffa et al. 2019; Padovani et al. 2017).

Chapter 4

The 1.5 GHz observations of the $z = 1.7$ HzRG: evidence for large scale feedback

In this Chapter we present novel deep observations of the J1030 field carried out with the JVLA in L-band (1.5 GHz). We present the data reduction of the total intensity and polarized signal. This dataset will be exploited here to investigate the radio properties of the $z = 1.7$ FRII radio galaxy, and unveil signatures of possible interaction between the radio galaxy plasma and the the surrounding proto-cluster ICM. A more general analysis of the new JVLA dataset will be presented in Chapter 5, where the radio-source catalogue will be presented. The results presented in this Chapter are reported in D'Amato et al. (2021) and D'Amato et al. (subm.).

4.1 JVLA observations and calibration of the J1030 field

We used the JVLA in configuration A to carry out observations of the J1030 field in L-band (1 – 2 GHz). The observations were organized in 11 observing blocks distributed from May to June 2018 (Project ID: VLA/18A-440, PI: I. Prandoni), for a total on-source observing time of ~30 hours. The Half Primary Beam Width (*HPBW*) of the observations is ~27 arcmin, as shown by the dashed green circle in the left panel of Fig. 5.1. The observed spectral range is covered by 16 *spws*; each *spw* consists of 64 channels of 1 MHz width. The quasar 3C147 was used as flux and bandpass calibrator, while the quasar J1024-0052 served as phase calibrator.

4.1.1 Total intensity calibration and imaging

The calibration and flagging of the datasets was initially performed through the calibration pipeline of the CASA package (version 5.1.2-4; McMullin et al., 2007). All the datasets were found to be strongly affected (>50%) by radio–frequency interference (RFI), as expected for the JVLA L-band[1]. This resulted in the failure of the calibration pipeline and required careful manual calibration of each raw dataset. We started by applying the Hanning–smoothing and online flags, following the pipeline procedure. Then we calibrated the two calibrators in order to perform a preliminary RFI flagging both in time and frequency using the FLAGDATA task of CASA. We recursively repeated this step two times to refine the flags after each calibration. Finally, we inspected the data to perform small additional manual flags when required. We note that this procedure is especially important for the phase calibrator, as it traces the RFI's variation across the full observing block. We found that *spw* 8 was strongly affected by contamination and decided to flag it entirely. Then, we performed standard gain and bandpass calibration and applied the calibration tables to the target. The calibrator flags are included in the gain tables and then are automatically applied to the target (the J1030 field). We found that four out of the 11 observing blocks were still strongly contaminated by RFI, and we decided to exclude them from the analysis. Then, we combined the remaining seven observations into the final dataset. Finally, the dataset has been self-calibrated by exploiting the luminous ($S_{1.4\ \mathrm{GHz}} \sim$ 200 mJy) NVSS J102921+051938 quasar (Condon et al., 1998), located in the J1030 field at ~17 arcmin South-West from the field center. This source will be also used in the next § 4.1.2 as polarization calibrator. We performed the imaging using the TCLEAN task of CASA with the AWPROJECT gridder, as required for wide fields. The robustness Briggs weighting was set to 0.5, corresponding to a restoring beam with a major (minor) axis of 1.31 (1.05) arcsec. This choice provides the best trade-off between resolution and sensitivity, and it also helps suppressing residual RFI affecting short baselines.

4.1.2 Polarized emission calibration and fractional polarization imaging

Standard polarization calibration normally requires the observation of a polarized calibrator. Unfortunately, we did not observe such a calibrator, since the analysis of polarized emission was not in the original intent of the observations. With the discovery of a possible positive AGN feedback scenario promoting star formation in multiple galaxies around the FRII RG (G19), we decided to explore the polarization properties of the RG. Polarization can indeed reveal signatures of interactions between the radio galaxy plasma and the surrounding proto-cluster ICM: in presence of shock fronts an increased fraction of the polarized emission is expected, together with an alignment of the magnetic field vectors perpendicular to the shock propagation direction (Brunetti & Jones 2014).

To overcome the lack of a polarized calibrator, we developed an ad hoc calibration procedure that exploits the flux/bandpass calibrator (3C147) and the presence of a strong polarized source in our target field (J1030) detected in the NVSS. This allowed us to produce polarized fraction images of the FRII RG in the two NVSS Intermediate Frequencies (IFs; two 42 MHz bands centered at 1365 MHz – IF1 – and 1435 MHz – IF2;

[1] https://science.nrao.edu/facilities/vla/docs/manuals/obsguide/rfi

Condon et al. 1998). As a first step we determined the instrumental leakage and cross-hand delay. While the leakage terms can be calculated using a non-polarized source at the observed frequency, in order to correct for the instrumental delay a source with significant polarized emission is usually required. We then used 3C147 (which in L-band has a polarization fraction <0.05%[2]) as leakage calibrator. If a significant leakage emission is detected in the linear polarization image of the source, then the leakage signal itself can be used to correct for the delays. We performed an imaging in total intensity (Stokes I) and linear polarization ($\sqrt{U^2 + Q^2}$, where U and Q are the Stokes parameters) of 3C147, finding that the total intensity is ~20 Jy, as expected from flux tabulated values of VLA calibrators (Perley & Butler, 2017). The measured polarized emission is ~1% of the total intensity, much higher than the upper limit reported for 3C147 (<0.05%). This demonstrates that leakage emission is significant. Thus, we first calculated the cross-hand delays using the GAINCAL task of CASA, combining all scans and *spws* to find one solution that will be bootstrapped to all the *spws* during the table application, as suggested by the CASA guidelines[3] for standard polarization calibration. Then, we calculated the leakage terms applying on-the-fly the cross-hand delays table. Finally we applied the leakage and delay tables to the target (J1030) and calibrator (3C147) fields. We re-imaged the total intensity and linear polarization of 3C147 after the corrections, finding that the total intensity is conserved, while the polarized emission is strongly reduced (fractional polarization ~0.01%, in agreement with the upper limit of this source).

Once the datasets are corrected for the instrumental effects, we need to calibrate the polarized emission and polarization angle. Although this is usually impossible without the observation of a polarized calibrator, we fortunately found a bright polarized point source in our target field (NVSS J102921+051938; also used to perform the self-calibration of the total intensity, see § 4.1.1). This source has polarization parameters derived from the two NVSS IFs reported in the literature. A simple model for this source can hence be derived and we can use it as a calibrator. The source mean polarized fraction ($\overline{F} = 4.73 \pm 0.3\%$) and mean polarization angle ($\overline{\tau} = 6.8 \pm 0.9$ deg) obtained from the two IFs are reported by Condon et al. (1998), while the source rotation measure ($RM = 11.7 \pm 7.5$ deg/m^2) is reported by Taylor, Stil & Sunstrum (2009). By exploiting the relation between the RM and the change in the position angle between IF1 and IF2 ($\Delta\tau = \tau_1 - \tau_2$; see Eq. 1 in Taylor, Stil & Sunstrum 2009), we can derive the position angles for IF1 (τ_1) and IF2 (τ_2) by solving the following system of two equations:

$$\begin{cases} \overline{\tau} = \frac{\tau_1+\tau_2}{2} \\ RM = C\frac{\Delta\tau}{\lambda_2^2-\lambda_1^2}, \end{cases} \tag{4.1}$$

where C is a correction factor that accounts for the finite bandwidth of the IFs (equal to

[2] https://science.nrao.edu/facilities/vla/docs/manuals/obsguide/modes/pol

[3] https://casaguides.nrao.edu/index.php?title=CASA_Guides:Polarization_Calibration_based_on_CASA_pipeline_standard_reduction:_The_radio_galaxy_3C75-CASA5.6.2

0.96 for the NVSS; Taylor, Stil & Sunstrum 2009), and λ_1 and λ_2 are the central wavelengths of the IF1 anf IF2, respectively. We find $\tau_1 = 8.4$ deg and $\tau_2 = 5.2$ deg. We note that we assumed no wrapping of the magnetic field between IF1 and IF2, as appropriate for sources with a $RM < 400$ deg/m^2 (Taylor, Stil & Sunstrum, 2009).

The polarization fraction of our calibrator is assumed to be equal to $\overline{F}$ in both the IFs; considering the IFs are contiguous and rather narrow, we expect that assuming an average value provides estimates of the polarized emission in the two IFs accurate enough for our purposes. Then, we shifted the phase center of target field on the calibrator source, and split it in a new calibrator field (using the CASA tasks FIXVIS and SPLIT, respectively). From this dataset, composed by the target field and the calibrator field (i.e., the target field phase-shifted on the calibrator source), we split two subsets, each heaving the same bandwidth and central frequency of the two NVSS' IFs. We manually set the calibrator polarized fraction and polarization angle in each subset via the SETJY task, then we calculated the gains and applied them to the target and calibrator field. In order to check whether the polarized fraction and polarization angle have been correctly applied to the target field, we performed a quick imaging of the target field around the calibrator position, and measured its linear polarized emission and polarization angle, finding a good agreement ($<1\sigma$) with the model values.

We performed the polarization imaging of the FRII source for the two IFs separately. The debiased linear polarization image is calculated following Eq. 5 of George, Stil & Keller (2012):

$$P = \sqrt{U^2 + Q^2 - 2.3\sigma_{UQ}^2} \tag{4.2}$$

where σ_{UQ} is the average *rms* of the U and Q images. This formula is suited for S/N $\geq$ 4 polarized emission. In our map only the brightest regions of the lobes have S/N $\gtrsim 4$, while the rest of the emission has S/N ≥ 3 (§ 4.1.2). This implies that the absolute value of the fractional polarization is less reliable in the low-S/N regions. Nevertheless we stress that the debias simply applies an offset to all pixels, and this does not affect the relative importance of the polarized emission in different regions of the source, which is what we are interested to investigate.

The debiased linear polarization images have a sensitivity of 36 μJy/b (IF1) and 32 μJy/b (IF2). We checked that such images do not suffer from significant in-band depolarization. To do so, we used the polarization-uncalibrated dataset, to produce polarization images for several bandwidths (5, 10, 50 100 MHz) centered on 1.4 GHz. This allowed us to identify the bandwidth at which depolarization overcomes the gain in sensitivity obtained from broadening the frequency range. We found that in-band depolarization starts to decrease the S/N of the polarized flux between 50 MHz and 100 MHz; thus, for the two IFs (each 42 MHz wide) in-band depolarization is not a matter of concern. As a final step, we computed the fractional polarization map for each IF, as the ratio between the

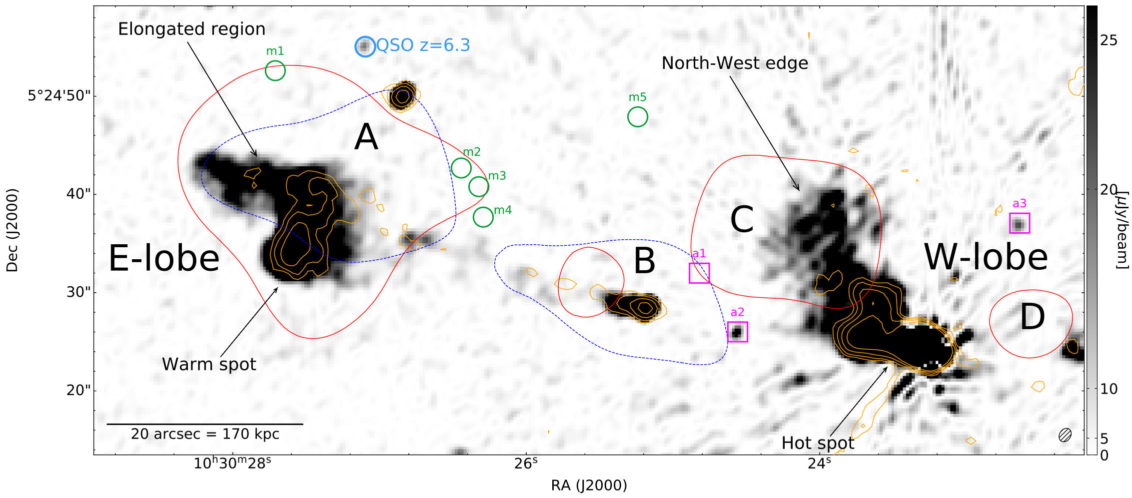

Figure 4.1: Cut-out of the 1.5 GHz JVLA image centered on the HzRG at z = 1.7. The old VLA contours at 1.4 GHz (Petric et al., 2003; Nanni et al., 2018) are reported in orange, starting from a 3σ threshold and increasing with a $\sqrt{3}$ geometric progression. Blue and red contours are the $\sim 2\sigma$ hard and soft X-ray diffuse emission, respectively. The four major components of such emission are labeled in black (A, B C and D). The positions of five of proto-cluster members discovered by MUSE ($m1 - m5$) are indicated by the green circles (a sixth source is located outside the cut-out, ~45 arcsec North-East from the FRII galaxy core). The positions of the proto-cluster members discovered by ALMA ($a1 - a3$) are marked by the magenta boxes. We note that $a2$ and $a3$ are detected in the JVLA image (they will be discussed in Chapter 5). The Eastern and Western lobes are labeled as E-lobe and W-lobe, respectively. The main morphological features of the lobes are also reported, indicated by the black arrows. The light blue circle indicates the z=6.3 QSO at the center of the J1030 field, which is detected for the first time in the radio-band (see Chapter 5 for a more in-depth discussion of this source). The solid black line at the bottom-left corner indicates the angular and physical scale, while the dashed ellipse at the bottom-right corner is the restoring beam of the JVLA image.

debiased linear polarization and the total intensity maps[4].

4.2 The z = 1.7 HzRG: radio–continuum properties

In this Section we investigate the radio–continuum properties of the z=1.7 HzRG located at the center of the proto-cluster, with particular respect to the morphology of its extended emission.

The total intensity 1.5 GHz JVLA image of the FRII radio galaxy is shown in Fig. 4.1. It is clear that the new JVLA observations reveal significantly more extended emission in both the lobes of the FRII RG than observed in the previous shallower VLA observations reported by Petric et al. (2003) and re-analyzed by Nanni et al. (2018, see orange contours in Fig. 4.1). The FRII galaxy is the second brightest source of the field, with a total flux

[4]To derive fully consistent fractional polarization maps we produced ad hoc total intensity images for the two NVSS IFs, with the same parameters of the U and Q Stokes used to calculate the linear polarization.

density of $S_{1.5\ \mathrm{GHz,\ obs}} \sim 28$ mJy. By assuming a spectral index $\alpha = 0.7$, this measurement corresponds to $S_{1.4\ \mathrm{GHz,\ obs}} \sim 30$ mJy, in perfect agreement with the value measured by NVSS (~30 mJy) and slightly larger than the one measured by Nanni et al. (2018, ~27 mJy, see Sect. 2.1), considering the local rms of ~2.5 μJy.

The RG W-lobe features a clear hotspot, whose emission constitutes ~75% of the total source flux density. It is interesting to note that the W-lobe emission extending to the North-West, and covering a projected area of ~110 arcsec^2, largely overlaps with the X-ray spot C, which is ascribed to thermal emission (see § 2.2.1). This finding strengthens the hypothesis that the W-lobe hits the surrounding medium, causing shock re-acceleration of the RG plasma particles.

The RG E-lobe presents a more complex geometry, and lacks of a classical hotspot (i.e., 1.4 GHz brightness > 0.6 mJy/arcsec^2 and brightness contrast with the rest of the radio source ≥ 4, following the hotspot definition of de Ruiter et al. 1990). The brightest region of the E-lobe is aligned along the axis passing through the core and the Western hotsopt, but seems to be located Southward of the eastern jet. We define it as a warm spot. The new JVLA observations reveal the presence of diffuse emission to the North of the of the warm spot and elongated in the East-West direction. This emission was not detected in the shallower VLA image. As already discussed in § 2.2.1, the overall E-lobe emission overlaps with the diffuse X-ray spot A. The JVLA observations reveal that the East-West elongated emission nicely coincides with the hard X-ray component (blue dashed contour in Fig. 4.1), suggesting that in this region a non-negligible part of the X-ray diffuse emission could be of non-thermal origin, associated with the IC-CMB process.

Thanks to the higher resolution and sensitivity of the new observations, the core and the Eastern jet base are resolved in the JVLA image. Thus, we can provide a more reliable estimate of the FRII galaxy inclination angle, based on the jet vs. counter-jet base flux density ratio R_{jet}, following G19 (see Sect. 2.1, Eq. 2.1). As in G19, we assume a jet velocity $\beta = 0.75$, a Doppler boost exponent $p = 2$, and a jet base spectral index $\alpha_{\mathrm{jet}} = 0.5$, and obtain $k = \beta\cos(\theta) \sim 0.14$, corresponding to $\theta \sim 80°$. This is consistent with the findings of G19 ($\theta \sim 70 - 80°$). We also provide a second estimate of the inclination angle, based on the jet length ratio $L_{\mathrm{jet}}/L_{\mathrm{cjet}}$, following Giovannini et al. (1998):

$$L_{\mathrm{jet}}/L_{\mathrm{cjet}} = (1+k)/(1-k), \text{ where } k = \beta\cos(\theta). \tag{4.3}$$

This is done for two working hypothesis: *i*) the Eastern jet ends at the edge of the East-West elongated emission and *ii*) the Eastern jet ends at the warm spot. In case *i*) we find $k \sim 0.25$, in case *ii*) we obtain $k \sim 0.14$, which nicely agrees with the value obtained from R_{jet}. This suggests that the warm spot may indeed correspond to the end of the approaching Eastern jet, which would likely imply a bending of the jet. This interpretation is also strengthened by the analysis of the polarized emission, presented in the next Section.

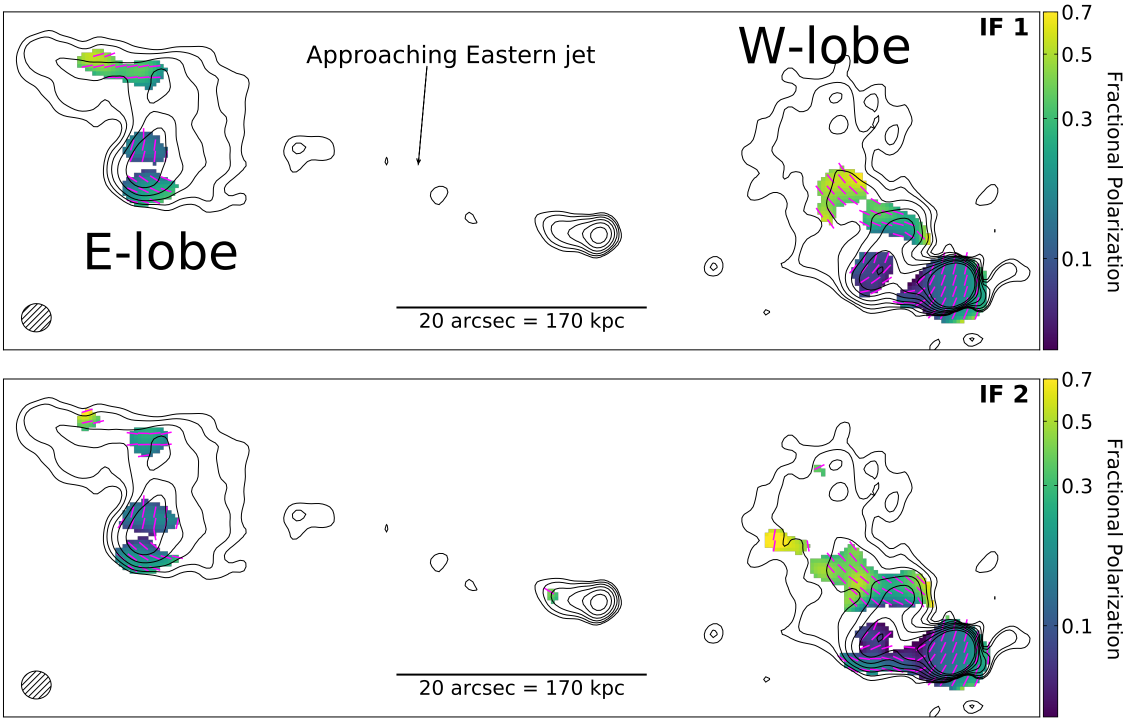

Figure 4.2: Fractional polarization images of the FRII HzRG in the two 42 MHz wide IFs: IF1 (1365 MHz, top panel) and IF2 (1435 MHz, bottom panel). The images are blanked at a 3σ threshold. The black contours indicate the total intensity emission from the full-band JVLA image, starting from a $\sim 3\sigma$ threshold and increasing with a $\sqrt{3}$ geometric progression. The magenta dashes indicate the orientation of the magnetic field. The dashed ellipse in the bottom left corner represents the restoring beam. The solid black lines in the bottom of the two panels indicate the angular and physical scales. For clarity, in the IF1 image we indicated the Eastern and Western lobes as E-lobe and W-lobe, respectively, and specify that the E-jet is the approaching one. From D'Amato et al. (2021).

Finally, we provide a revised estimate of the source size, based on the full extent of the radio emission. The RG (deconvolved) major axis is measured to be 1.3 arcmin, which corresponds to a projection-corrected physical size of ~700 kpc (to be compared with the value of ~600 kpc reported by G19).

4.3 The $z = 1.7$ HzRG polarization properties: signatures of AGN feedback?

The fractional polarization maps of the FRII RG are shown in Fig. 4.2, blanked at the 3σ level of the linear polarization) for IF1 (top) and IF2 (bottom). The magnetic field orientation, calculated as $0.5\arctan(U/Q) + \pi/2$[5], in steps of 3 pixels (i.e., half of the beam radius), is indicated by the magenta dashes.

The fractional polarization of the FRII HzRG shows a patchy structure (Fig. 4.2).

[5]In other words we define the magnetic field orientation as perpendicular to the electric vector. This is formally correct only under the hypothesis of optically-thin plasma.

Both the Western and Eastern spots are detected, as well as the terminal part of the Western jet (clearly visible in IF2). Patchy polarized emission is also detected in the extended structures of the lobes. The fractional polarization in the W-lobe hotspot and E-lobe warm spot is in the 10% – 20% range in both IFs[6]. In addition, the magnetic field appears to be oriented along the jet axis in the Western jet. Both the level of fractional polarization and the magnetic field orientation are consistent with what typically found in FRII radio galaxies (Parma et al., 1993; Muxlow & Garrington, 1991; Pentericci et al., 2000). Furthermore, the similar fractional polarization values found in the Western and Eastern spots is consistent with an edge-on orientation of the FRII galaxy with respect to the line of sight (see G19 and § 4.2), under the hypothesis of a uniform distribution of the local medium (Laing 1988; Garrington & Conway 1991).

We note that the Eastern warm spot shows two regions of significant polarized emission; moreover, the magnetic field seems to experience a 90 degree rotation going from the Southern to the Northern patch, showing a wrapping around the peak emission of the total intensity, as observed in several cases around FRII hot spots (Saikia & Salter, 1988; Pentericci et al., 2000). We can then argue that the southern patch may correspond with the terminal region of the approaching Eastern jet, as previously argued (Sect. 4.2), with the Northern patch likely associated with a bending of the jet, due to the impact with the external medium. The polarized emission detected in the East-West elongated region of the E-lobe extends along the Northern edge of the lobe and shows an increase of the fractional polarization from West to East, suggesting the presence of another compression front.

More in general, when analysing the extended regions of both the FRII radio galaxy lobes, we notice an increased polarization fraction in correspondence of bending morphologies in total intensity. The orientation of the magnetic field also seems to follow the observed bendings. Considering that the source is seen at almost edge-on orientation, these observational features may again suggest that these regions experience a compression and an alignment of the magnetic field, possibly associated with the impact with components of the ICM. We point out, however, that another, perhaps simpler, explanation exist for the observed bendings in the lobes, i.e. peculiar motion of the galaxy through the ICM. This scenario would be supported by the observed line of sight velocity offset between the galaxy and the dynamic center of the proto-cluster (see § 3.2.5), if evidence for radio plasma – ICM interactions reported earlier in this Thesis (see Sect. 2.1, § 2.2.1 and Sect. 4.2) is neglected.

As a final caveat, we point out that the observed spots and knots may be partially optically thick. This would affect the relative orientation of the electric and magnetic field vectors, making the interpretation of the magnetic field orientation in these regions more uncertain. In addition, the polarization fraction of the source used as a polarization

[6]The polarized signal S/N is > 4 in the spots' regions, hence debiasing can be considered reliable, as well as the measured fractional polarization values.

calibrator may have varied across the nearly three decades span between the NVSS and our observations. However, over these time-scales the variation of the polarization fraction is typically $\lesssim$10% (Galluzzi et al., 2017), which is certainly smaller than the overall uncertainties of our calibration method.

In summary we conclude that, while the presence of interactions between the radio plasma and the surrounding ICM are able to simultaneously explain all the observed features, several caveats exist which prevent us from an unambiguous interpretation of our results. Further radio observations are needed to confirm or reject the presence of plasma-ICM interactions, and shed further light on the positive feedback mechanism. In fact, we asked and obtained new low-frequency observations of the HzRG with the Low Frequency Array (LOFAR, 144 MHz) and the Upgraded Giant Metrewave Radio Telescope (uGMRT, 550-850 MHz and 250-500 MHz). Both LOFAR and uGMRT observations have been already carried out. While uGMRT observations are still in the data-reduction phase, preliminary results from the LOFAR map show more extended emission with respect the JVLA map presented in this work, arising from low-energy electron population in both the FRII RG lobes; moreover, spectral index map built from the 144 MHz LOFAR and 1.5 GHz JVLA observations show a flattening of the spectral index towards the external region of the FRII RG lobes, as a likely signature of shock-induced re-acceleration of the electrons. This finding further strengthens the AGN positive feedback scenario.

Chapter 5

The J1030 JVLA field: a legacy for the future

In this Chapter we present the overall statistical properties of the new radio–continuum JVLA image obtained through the data reduction process described in Chapter 4. We also present the radio-source catalogue extracted from it and the derived source counts. A full exploitation of this catalogue is beyond the scopes of this Thesis. Here we just present the properties of some notable sources in the field, and investigate the relation between the X-ray and radio luminosity of the J1030 *Chandra* catalogue (Nanni et al. 2018). Spectroscopic and/or photometric redshifts for the Chandra sources were derived by Marchesi et al. (2021, see Chapter 2 for more details). The results presented in this Chapter are going to be published in D'Amato et al. (subm.).

5.1 The JVLA field

The JVLA 1.5 GHz field is shown in Fig. 5.1 (left panel); it has a diameter of 30 arcmin and corresponds to the region over which the radio source catalogue has been extracted. We restricted our analysis to the inner 30 arcmin diameter of the field to keep under control smearing effects (described in § 5.1.1). This region fully encompasses the JVLA 1.5 GHz *HPBW* (~27', green dashed circle) and the field covered by the deep *Chandra* mosaic (solid cyan line; see Nanni et al. 2018 and Chapter 2). The visibility area of this 30 arcmin diameter region is shown in the right panel of Fig. 5.1 (right panel). We note that the deepest rms reached at the center is ~2.5 μJy/b, the ~50% of the analyzed area has a noise level $\lesssim$ 3.5 μJy/b (vertical red dashed line), and ~100% is below 6 μJy/b. The achieved sensitivity makes our field one of the deepest radio surveys to date; in Fig. 5.2 we show a comparison of the J1030 radio survey (5σ) sensitivity and area with those of other deep radio surveys available to date at cm wavelengths.

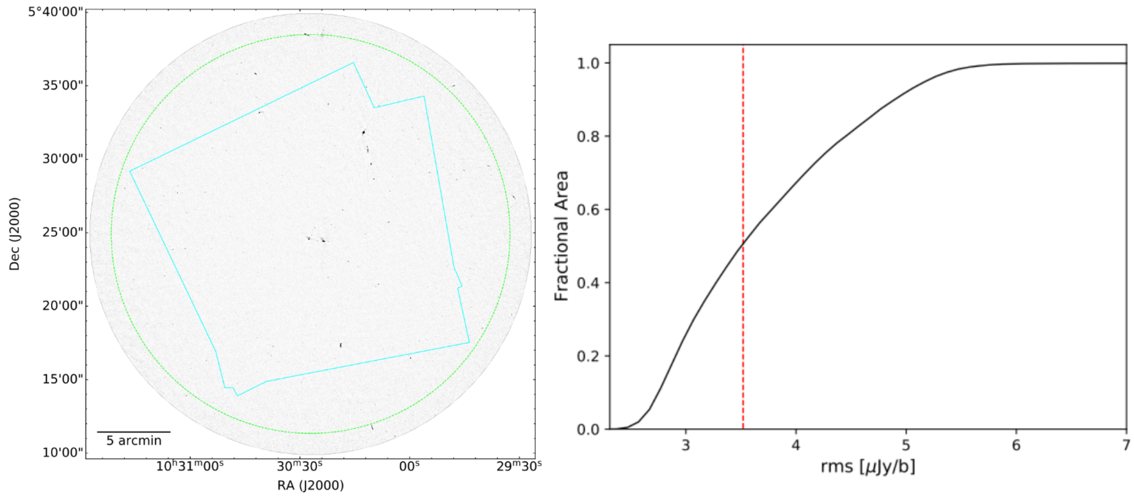

Figure 5.1: *Left*: 1.5 GHz JVLA image of the J1030 field. The field considered here has a diameter of 30', and corresponds to the region where the source catalogue has been extracted. The *HPBW* for the JVLA at 1.5 GHz is ~27' and is indicated by the green dashed circle. The region covered by the *Chandra* mosaic is marked by the solid cyan line. *Right*: Visibility area of the JVLA field (black solid line). The median noise is 3.5 μJy/b, and is indicated by the red vertical dashed line.

5.1.1 Time and bandwidth smearing

Wide-field radio imaging is affected by smearing effects that reduce the peak flux density of a source while correspondingly increasing the apparent source size such that the total integrated flux density is conserved. Smearing effects increase with the distance from the phase center of the image and depend on the spatial resolution, the observing frequency, and the time and frequency resolution. More specifically, time and frequency resolutions determine distortion along the tangential and radial directions at a given distance from the image center, respectively (Bridle & Schwab, 1999, Eq. 18-29 and Eq. 18-43). Considering the integration time (2 seconds) and the spectral resolution (1 MHz) of our observations, we have that at 15 arcmin radius from the center the tangential and radial smearing are ~0.3% and ~10%, respectively. A radial smearing of 10% is significant, but still acceptable. Considering that the image sensitivity degrades very steeply beyond the *HPBW* (green circle in Fig. 5.1), we decided to limit our analysis to the inner 15 arcmin radius region. This region fully encompasses the *Chandra* mosaic (Fig. 5.1).

5.2 Source detection and catalogue extraction

We derived the source catalogue using the Python Blob Detector and Source Finder (PyBDSF; Mohan & Rafferty, 2015). In the source extraction process PyBDSF takes into account local variations of the background noise. We derived the noise image, using a sliding box with a side of 45 pixels and a step of 15 pixels, which is found to fairly reproduce the noise variations measured across the image. In regions around very bright

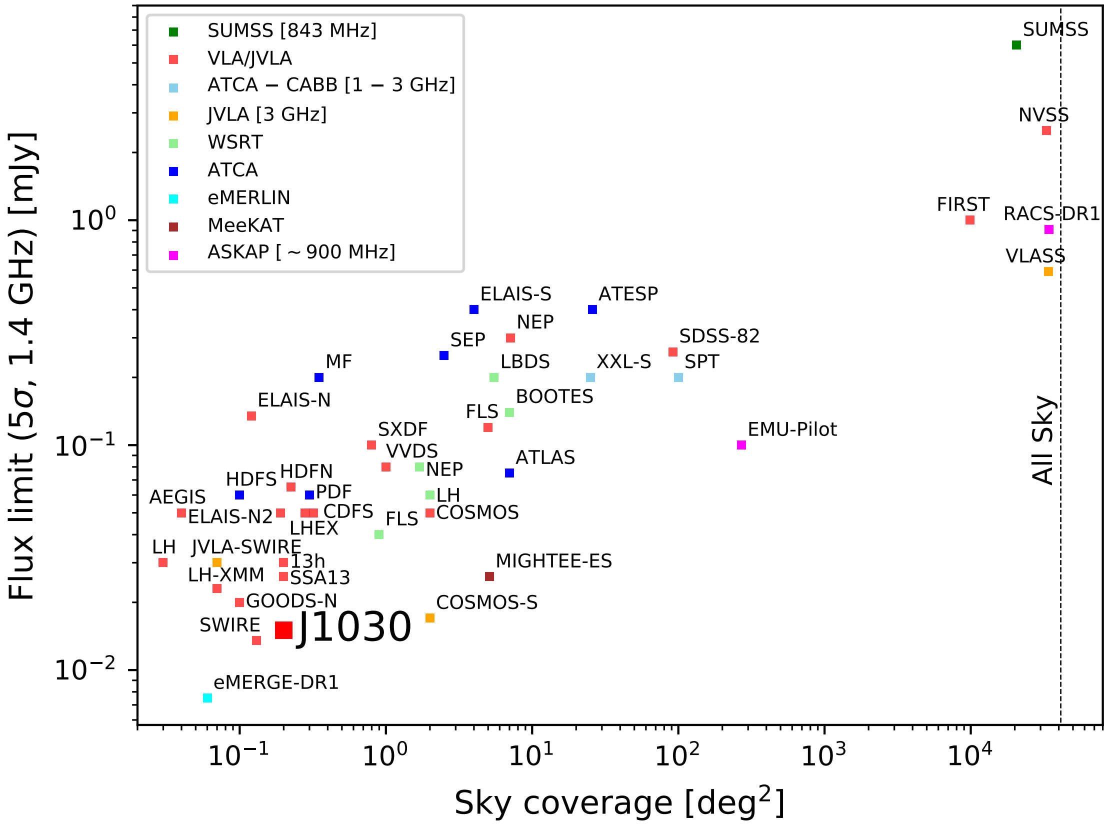

Figure 5.2: Sky coverage vs. sensitivity limit (5σ) for available radio survey at cm wavelengths, color-coded by the instrument as in the legend. The flux densities refer to 1.4 GHz; the surveys at other frequencies have been rescaled to 1.4 GHz assuming a radio spectral index of 0.7. The large red square indicates the J1030 field presented in this work. The reported surveys are as follows: LBDS (Windhorst, van Heerde & Katgert, 1984), NEP (VLA, Kollgaard et al., 1994), FIRST (White et al., 1997), MF (Gruppioni et al., 1997), NVSS (Condon et al., 1998), PDF (Hopkins et al., 1998), ELAIS–S (Gruppioni et al., 1999), ELAIS–N (Ciliegi et al., 1999), SUMSS (Bock, Large & Sadler, 1999), ATESP (Prandoni et al., 2000), BOOTES (de Vries et al., 2002), VVDS (Bondi et al., 2003), FLS (VLA, Condon et al., 2003), FLS (WSRT, Morganti et al., 2004), 13h (Seymour, McHardy & Gunn, 2004), HDFN (Huynh et al., 2005), LHEX (Oyabu et al., 2005), SXDF (Simpson et al., 2006), ELAIS–N2, LH–XMM and HDFN (Biggs & Ivison, 2006), SSA13 (Fomalont et al., 2006), ATLAS (Norris et al., 2006), COSMOS (Schinnerer et al., 2007), AEGIS (Ivison et al., 2007), SWIRE (Owen & Morrison, 2008), LH (VLA, Ibar et al., 2009), NEP (WSRT, White et al., 2010), GOODS–N (Morrison et al., 2010), SDSS–82 (Hodge et al., 2011), JVLA–SWIRE (Condon et al., 2012), SEP (White et al., 2012), CDFS (Miller et al., 2013), COSMOS–S (Smolčić et al., 2017a), LH (WSRT, Prandoni et al., 2018), RACS–DR1 (McConnell et al., 2020), MIGHTEE–ES (Heywood et al., 2021), EMU–Pilot (Norris et al., 2021), VLASS (ongoing, Lacy et al., 2016), eMERGE–DR1 (ongoing, Muxlow et al., 2020), SPT (ongoing, PI: N. Tothill), XXL–S (ongoing as part of SPT, PI: V. Smolčić).

sources (S/N $\gtrsim$ 150), noise variations are higher due to residual phase errors. Hence the box side was reduced to 30 pixels with a step of 10 pixels. We set an initial detection threshold to 4.5σ, where σ is defined as the local rms noise at the source position. This allows to account for errors in the measured fluxes, and avoid that low S/N sources are missed by the detection algorithm. The final detection threshold was then derived through the reliability analysis (see Sect. 5.2.1).

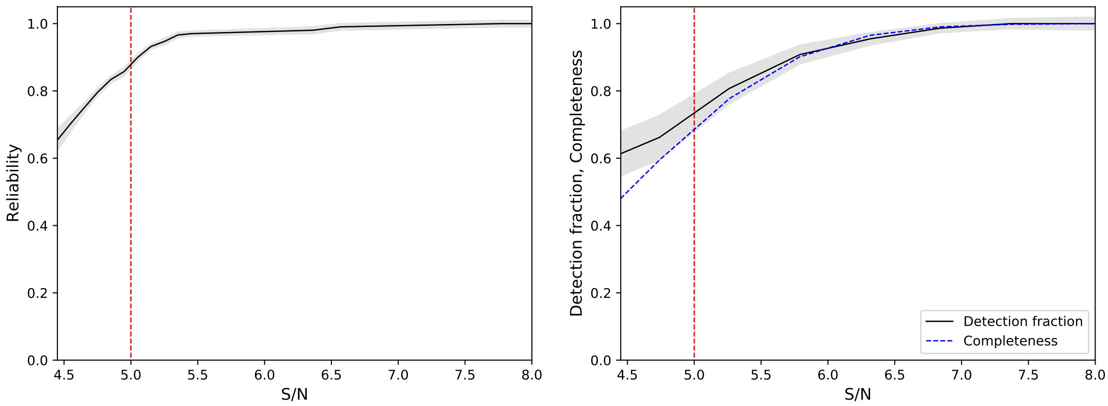

Figure 5.3: *Left*:Reliability function of the catalogue (black solid line) with the 1-σ uncertainty (grey shades) as a function of the S/N. The red vertical dashed line marks the detection threshold (S/N=5), corresponding to a reliability value of 90%. *Right:* Mean detection fraction of the simulated point-like sources (black solid line) with the 1-σ uncertainty (grey shades) as a function of the S/N. The red vertical dashed line marks the detection threshold (S/N=5). The blue dashed line indicates the S/N completeness function (see text for more details).

5.2.1 Catalogue Reliability

We assessed the catalogue reliability as a function of the S/N. To this goal, we ran PyBDSF on the negative image (i.e. an image in which each pixel has the same value, but inverted sign, see also § 3.2.3) using the same parameters adopted for the catalogue extraction. We found a total of 136 negative detections in the inner 15 arcmin radius region; they have a homogeneous spatial distribution that excludes the presence of highly biased regions, especially near to bright sources where the noise may significantly deviate from a random Gaussian distribution due to the presence of residual artifacts. We defined the false detection rate (FDR) as the ratio between the negative and positive detections, and the reliability as R = 1-FDR$|_{S/N}$, where FDR$|_{S/N}$ is the integrated FDR at a given S/N. The reliability as a function of S/N is reported in Fig. 5.3 (left panel). The errors are obtained from by propagating the Poisson errors of the negative detections. We found that the reliability is higher than 90% for S/N $\gtrsim$ 5 and 100% for S/N $\gtrsim$ 5.5.

5.2.2 Catalogue completeness

The presence of background noise introduces errors in the measurement of source fluxes. This causes source catalogues to be affected by incompleteness at low S/N. If the noise (and hence flux errors) follow a Gaussian distribution, the S/N incompleteness can be analytically evaluated and corrected by exploiting the Gaussian Error Function (see e.g. Mandal et al. 2021). In order to verify whether the noise follows a Gaussian distribution, we generated ten simulated catalogues of point-like sources and injected them in the image at random positions, over the same area where the source catalogue was extracted (30 arcmin diameter). For each simulation the source fluxes were drawn from an uniform distribution, spanning a flux range going from 2 times the rms at the center of the image to 20 times the rms at 15 arcmin from the center. Sources are forced to be at least 4 arcsec apart from each other, to avoid overlaps that may introduce systematics in the flux measurements and source statistics. The choice of uniform flux distribution was motivated by the need of having good statistics in each flux bin, without increasing too much the size of the simulated samples. Each simulation is composed of 1000 sources, that were injected in the image through the ADDCOMPONENT tool of CASA. We checked that the visibility area is not significantly altered after the injection of the simulated sources, i.e. that the noise distribution remains the same as in the original map. For each simulated catalogue, we ran PyBDSF with the same parameter setting as used for the extraction of the real sources. The recovered sources are identified by matching the PyBDSF detections with the input catalogues of simulated sources, using a maximum separation of 0.5 arcsec between the input source position and the PyBDSF position. Then, we calculated the detection fraction (DF) as a function of S/N, as the ratio between the detected sources and the total sources in each S/N bin (that is 0.5 wide). Finally, we calculated the overall DF and its error as the mean and standard deviation of the DFs of the ten simulations. We report the DF as a function of S/N in Fig. 5.3 (black solid line, right panel). We note that, since the DF has been calculated in bins of S/N, we do not have to correct it for the visibility area.

In the case of a pure Gaussian noise distribution, the probability of a single measurement to fall outside of a given range $\pm x$ is given by the complementary Gaussian Error Function $\mathrm{erfc}(x) = 1 - \mathrm{erf}(x)$, where $\mathrm{erf}(x)$ is the Gaussian Error Function. If we set $x = (\sigma_{\rm th} - S/N)/\sqrt{2}$, where $\sigma_{\rm th}$=4.5 is the detection threshold used in the catalogue extraction, we can define the S/N completeness as:

$$C_{\rm S/N} = 0.5\,\mathrm{erfc}(x), \tag{5.1}$$

that is the probability that a measurement whose intrinsic S/N is above the detection threshold falls below it. We show the completeness function (blue dashed line) in Fig. 5.3 (right panel) and compare it with the measured DF. It is clear that the two completeness estimates are in agreement (at 1σ, see the grey shades), at least down to S/N $\lesssim$ 5. Down to this limit the completeness can be fairly predicted by assuming a Gaussian noise distribution.

We note that there are two kinds of incompleteness: the one described here which mostly affects point sources, and the so called *resolution bias*, which instead affects well resolved sources. The latter will be discussed in Sect. 5.4.1.

5.3 Final source catalogue

Based on the reliability and completeness analysis, we decided to set as detection threshold for the final catalogue S/N = 5, corresponding to a total of 1283 sources. At this threshold the reliability of the catalogue is 90% and the completeness is 70%. The catalogue gets $\sim$ 100% reliable and > 80% complete at S/N $\gtrsim$ 5.5. The sources classified as multi-component sources (i.e., that are fitted by multiple Gaussian models) are 29, and are labeled with an "M" flag in the catalogue. We manually inspected these sources and found that the peak and total flux densities are correctly measured, whereas their size are in general smaller than what inferred from the flux distribution within their 3σ boundaries. In addition, we found 14 extended sources with a complex morphology, that cannot be adequately described by the Gaussian fitting performed by PyBDSF. Many of these sources result in different entries in the catalogue, as their components are not recognized as being part of a same source by PyBDSF. We manually measured the emission and size of these sources and substituted the various entries in the catalogue with a single one accounting for all the source components, Such sources are flagged as "E" in the catalogue. The remaining 1240 sources, well-fitted by a single Gaussian component, are flagged as "S" in the catalogue. We list the first ten entries of the source catalogue in Table 5.1. A complete version of this table will be available at the Centre de Données astronomiques de Strasbourg (CDS). The columns provide the following parameters:

- Column 1: Radio-source identification number (RID).
- Columns 2 and 3: Right ascension (RA) and its error in degrees.
- Columns 4 and 5: Declination (Dec) and its error in degrees.
- Columns 6 and 7: Total flux density (S_T) and its error in μJy.
- Columns 8 and 9: Peak flux density (S_P) and its error in μJy/beam.
- Columns 10 and 11: Fitted major axis (Maj) and its error in arcsec.
- Columns 12 and 13: Fitted minor axis (Min) and its error in arcsec.
- Columns 14 and 15: Fitted position angle (PA) and its error in degrees.
- Columns 16 and 17: Deconvolved major axis ($\mathrm{Maj_{DC}}$) and its error in arcsec.
- Columns 18 and 19: Deconvolved minor axis ($\mathrm{Min_{DC}}$) and its error in arcsec.
- Columns 20 and 21: Deconvolved position angle ($\mathrm{PA_{DC}}$) and its error in degrees.
- Column 22: Local rms in μJy/beam.
- Column 23: Source flag.

RID	RA [deg]	Dec [deg]	S_T [μJy]	S_P [μJy/beam]	Maj [arcsec]	Min [arcsec]	PA [deg]	$\mathrm{Maj_{DC}}$ [arcsec]	$\mathrm{Min_{DC}}$ [arcsec]	$\mathrm{PA_{DC}}$ [deg]	rms [μJy/beam]	Flag
1	157.86122 ± 4E-05	5.41278 ± 3E-05	35 ± 10	29 ± 5	1.8 ± 0.4	1.0 ± 0.1	121 ± 16	–	–	–	5.1	S
2	157.85838 ± 3E-05	5.38995 ± 2E-05	45 ± 11	33 ± 5	1.6 ± 0.3	1.3 ± 0.2	106 ± 30	1.1 ± 0.3	0.0 ± 0.2	91 ± 30	5.0	S
3	157.85789 ± 3E-05	5.39100 ± 2E-05	92 ± 16	46 ± 6	1.9 ± 0.3	1.5 ± 0.2	102 ± 25	1.5 ± 0.3	0.9 ± 0.2	91 ± 25	5.3	S
4	157.85756 ± 2E-05	5.41786 ± 1E-05	140± 13	76 ± 5	1.9 ± 0.1	1.4 ± 0.1	107 ± 10	1.5 ± 0.1	0.7 ± 0.1	97 ± 10	4.6	S
5	157.85775 ± 3E-05	5.41681 ± 2E-05	23 ± 7	26 ± 4	1.4 ± 0.3	1.0 ± 0.1	100 ± 22	–	–	–	4.8	S
6	157.85592 ± 3E-05	5.39919 ± 2E-05	48 ± 11	38 ± 5	1.5 ± 0.2	1.2 ± 0.2	125 ± 28	0.9 ± 0.2	0.3 ± 0.2	104 ± 28	5.1	S
7	157.85485 ± 2E-05	5.38497 ± 1E-05	93 ± 13	58 ± 5	1.9 ± 0.2	1.3 ± 0.1	112 ± 12	1.4 ± 0.2	0.4 ± 0.1	103 ± 12	5.1	S
8	157.85450 ± 4E-05	5.36899 ± 3E-05	94 ± 19	36 ± 5	2.4 ± 0.4	1.6 ± 0.2	123 ± 19	2.1 ± 0.4	1.1 ± 0.2	119 ± 19	5.2	S
9	157.85355 ± 2E-05	5.39500 ± 1E-05	82 ± 12	57 ± 5	1.7 ± 0.2	1.2 ± 0.1	91 ± 14	–	–	–	5.1	S
10	157.84847 ± 2E-05	5.48333 ± 1E-05	93± 11	60 ± 5	1.7 ± 0.1	1.4 ± 0.1	115 ± 19	1.1 ± 0.1	0.6 ± 0.1	94 ± 19	4.5	S

Table 5.1: The first ten entries of the radio-source catalogue. Columns are described in the text (§ 5.2.1). A complete version of the catalogue will be available at the CDS site.

5.3.1 Flux scale

We checked the flux scale of our catalogue by comparing the total flux density of our sources against the values reported by the VLA Faint Images of the Radio Sky at Twenty-centimeters (FIRST) survey at 1.4 GHz (Becker, White & Helfand, 1995). In order to increase the statistics, we considered in this case a larger sample, taking into account all the sources detected by PyBDSF up to a 30 arcmin radius from the field center. We used a matching radius of 2 arcsec, defined from the analysis of the separation distribution of the matched sources. We restricted the analysis to the FIRST point-like source, finding 22 matches. We found that the median JVLA-to-FIRST flux density ratio is 0.91. Such an offset is likely to be ascribed to the higher resolution of our JVLA survey.

5.3.2 Source Sizes

The ratio between the total flux density (S_T) and the peak flux density (S_P) of a radio source is inherently related to its extension. For sources described by a 2D-Gaussian model, the total-to-peak flux ratio is given by the following equation (Prandoni et al., 2000):

$$\frac{S_T}{S_P} = \frac{\theta_{\mathrm{min}}\theta_{\mathrm{maj}}}{b_{\mathrm{min}}b_{\mathrm{maj}}} \tag{5.2}$$

where θ_{min} and θ_{maj} are respectively the minor and major axis of the source, and b_{min} and b_{maj} are respectively the minor and major axis of the synthesized beam. In Fig. 5.4 (left panel) we report the S_T/S_P distribution of our sources as a function of S/N. We note that at low S/N there are many sources that, due to flux measurement errors, have $S_T/S_P <$ 1. On the other hand, at high S/N random errors become negligible and systematic errors show up. In particular we see that S_T/S_P tends to ~1.1 as expected, given the estimated 10% radial smearing effect discussed in § 5.1.1. We can use the S_T/S_P distribution as a function of S/N to discriminate between resolved and unresolved source, by taking into proper account both random and systematic flux measurement errors. The minimum ratio S_T/S_P that reliably separates resolved from unresolved sources can be expressed as a function of S/N by the following relation (e.g., Prandoni et al., 2000; Retana-Montenegro et al., 2018; Mandal et al., 2021):

$$\frac{S_T}{S_P} = \epsilon \left[1 + N \times \sigma\left(\frac{S_T}{S_P}\right)\right] \tag{5.3}$$

where ϵ accounts for systematic errors and is set to 1.1, as found at high S/N. The factor $N{\times}\sigma(S_T/S_P)$ accounts for random errors and is expressed in multiples (N) of the standard deviations $\sigma(S_T/S_P)$. For a 90% significance level N≈1.64. In the case of 2D-Gaussian fits and Gaussian error, Condon (1997) derived the error propagation for the fit parameters, describing the relative errors for the fitting axes ($\sigma(\theta_{\rm maj})/\theta_{\rm maj}$ and $\sigma(\theta_{\rm min})/\theta_{\rm min}$) as a function of S/N. In particular, for a non-resolved source, these relative errors can be written as:

$$\frac{\sigma(\theta_{\rm maj})}{\theta_{\rm maj}} = k_1 \ {\rm S/N}^{-1} \tag{5.4}$$

$$\frac{\sigma(\theta_{\rm min})}{\theta_{\rm min}} = k_2 \ {\rm S/N}^{-1} \tag{5.5}$$

where k_1 and k_2 are proportional factors. By fitting $\sigma(\theta_{\rm maj})/\theta_{\rm maj}$ and $\sigma(\theta_{\rm min})/\theta_{\rm min}$ as a function of S/N we found for our sources $k_1 = 1.14$ and $k_2 = 0.93$. Then from Eq. 5.2 we obtain the following expression for S_T/S_P errors:

$$\sigma\left(\frac{S_T}{S_P}\right) = [k_1^2 + k_2^2]^{1/2} \ {\rm S/N}^{-1} \approx 1.48 \ {\rm S/N}^{-1} \, . \tag{5.6}$$

If we substitute Eq. 5.6 into Eq. 5.3 we obtain:

$$\frac{S_T}{S_P} = 1.1 \times \left[1 + \left(\frac{2.44}{S/N}\right)\right] \tag{5.7}$$

which represents the curve that subtends unresolved sources at a 90% significance level (black solid line in Fig. 5.4, left panel). Indeed, we note that if this curve is mirrored with respect to the S/N axis, it comprises almost all the sources characterised by $S_T/S_P < 1$.

5.4 Systematic effects

5.4.1 Resolution bias

The completeness of the catalogue does not only depends on the S/N of the sources, but also on their angular size. Given a total flux density, the larger the source the wider the area over which the flux is distributed and the lower its peak flux density. Thus, a larger source will drop below the detection threshold more easily than a smaller source with the same total flux density. This is called resolution bias. In case of errors following a Gaussian distribution, the resolution bias can be analytically treated following the procedure of Prandoni et al. (2001a). The maximum deconvolved size that a source can have without

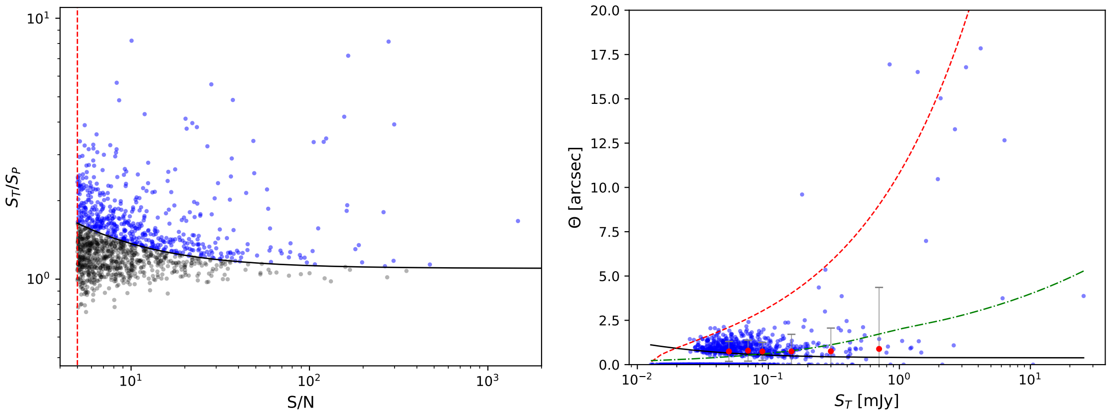

Figure 5.4: *Left*: Ratio between total (S_T) and peak (S_P) flux density as a function of S/N. The red vertical dashed line marks the detection threshold (S/N=5). The black solid line divides resolved sources (above the line, blue points) from unresolved sources (below the line, black points). *Right:* Deconvolved source size as a function of total flux density. Unresolved source have deconvolved size set to 0. The red circles mark the median deconvolved size in bins of S_T with 1σ error indicated by the grey bars. The red dashed line indicates the maximum deconvolved size ($\Theta_{\rm max}$, Eq. 5.8), the green dash-dotted line represents the median size relation of Windhorst, Mathis & Neuschaefer (1990) ($\Theta_{\rm med}$, Eq. 5.11), calculated assuming a flux-dependent exponent m (Eq. 5.12). The solid black line is the minimum deconvolved size ($\Theta_{\rm min}$, Eq. 5.9).

falling below the detection threshold of S/N=5, as a function of the total flux density S_T, can be written as:

$$\Theta_{\rm max} = \Theta_{\rm N}\sqrt{S_T/(5\sigma) - 1} \tag{5.8}$$

where $\Theta_{\rm N}$ is the geometric mean of the synthesized beam axes and σ is the image noise. By exploiting Eq. 5.2 and Eq. 5.7 we can also derive an approximate function for the minimum deconvolved size (i.e., minimum size that can be resolved):

$$\Theta_{\rm min} = \Theta_{\rm N}\sqrt{1.1 \times \left(1 + \frac{2.44}{S_T/(5\sigma)}\right) - 1}. \tag{5.9}$$

In Fig. 5.4 (right panel) we report the source deconvolved sizes as a function of their total flux. The deconvolved size is assumed equal to the source axes geometric mean if $\theta_{\rm maj}/\theta_{\rm min} < 3$ and equal to $\theta_{\rm maj}$ otherwise. Unresolved sources, i.e. those below the curve defined by Eq. 5.7, have their deconvolved sizes set to 0. The red filled circles indicate the median deconvolved size of the sources in bins of S_T from 0.4 mJy to 1 mJy. The bin size varies from 0.2 mJy to 0.6 mJy, in order to have sufficient statistics in each bin. We also plot the maximum ($\Theta_{\rm max}$) and minimum ($\Theta_{\rm min}$) deconvolved size, defined by Eq. 5.8 and Eq. 5.9 respectively, where we set σ equal to the image median noise (3.5 μJy). We note that the deconvolved size of the majority of the sources lies below the $\Theta_{\rm max}$ relation, as expected.

To evaluate the impact of resolution bias on our catalogue, we need to infer the intrin-

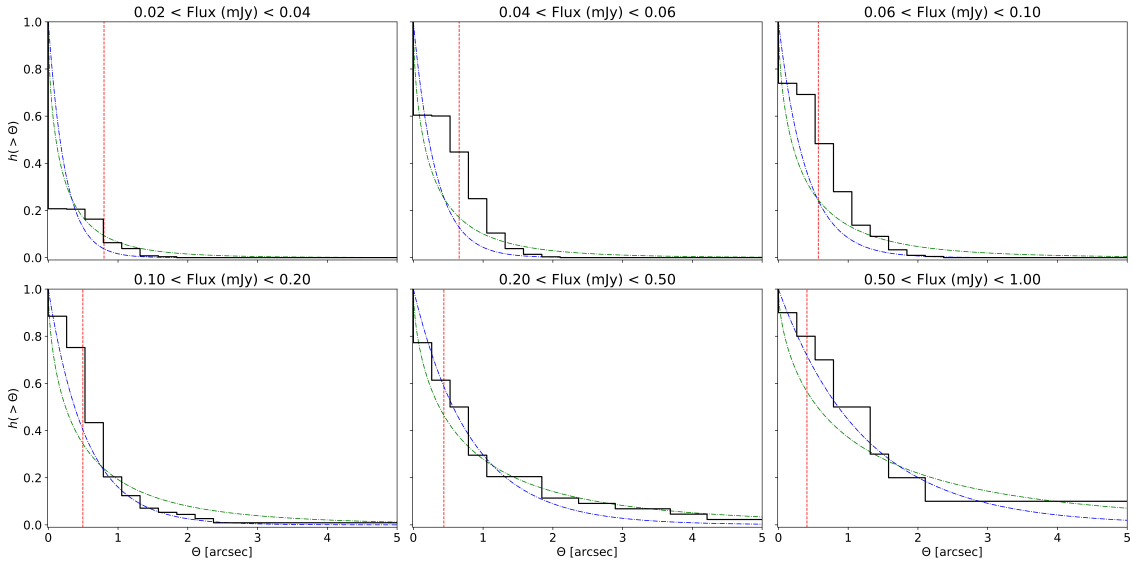

Figure 5.5: Cumulative size distribution of our source sample (black solid line) in six bins of flux density. The red dashed line represents the minimum deconvolved size (Eq. 5.9), while the green and blue dash-dotted lines represent the source size cumulative distribution function described by Eq. 5.10, setting $q = 0.62$ and $q = 1$ respectively. All lines are calculated at the geometric mean of each flux bin.

sic size distribution of the sources; this will provide us with the number of sources, with a given flux density, that have a deconvolved size larger than $\Theta_{\rm max}$ and thus are missed in our survey. Based on 1.4 GHz surveys available at the time, Windhorst, Mathis & Neuschaefer (1990) proposed the following (empirical) source size integral distribution, that has been widely used since then to estimate the resolution bias (e.g., Prandoni et al., 2001a; Huynh et al., 2005; Hales et al., 2014b; Mandal et al., 2021):

$$h(>\Theta) = \exp[-\ln 2(\Theta/\Theta_{\rm med})^q] \tag{5.10}$$

where $q = 0.62$ and $\Theta_{\rm med}$ is the median size distribution of the sources as a function of flux density:

$$\Theta_{\rm med} = k \times (S_{1.4\ \rm GHz})^m \tag{5.11}$$

with $k = 2$ arcsec, $m = 0.3$ and $S_{1.4\ \rm GHz}$ is in units of mJy. These parameters are best suited to describe source sizes down to 1.4 GHz flux densities of a few mJy. More recently, a steeper exponent m was proposed for sub-mJy sources (Richards, 2000; Bondi et al., 2008; Smolčić et al., 2017a). Following Mandal et al. (2021), we assume a flux-dependent $m = m(S)$ exponent, to account for a smooth transition between the sub-mJy regime dominated by SFG or host-confined AGN ($m = 0.5$) and the mJy regime dominated by extended radio-galaxies ($m = 0.3$):

$$m(S_{1.4\ \rm GHz}) = 0.3 + 0.2\exp(-S^2_{1.4\ \rm GHz}) \tag{5.12}$$

We found that the median size of our sample (red circles in Fig. 5.4, right panel) is fairly reproduced by a $\Theta_{\rm med} - S_{1.4\ \rm GHz}$ relation with a variable exponent $m(S_{1.4\ \rm GHz})$ (see green dash-dotted line in Fig. 5.4).

In Fig. 5.5 we show the integral size distribution of our source sample in different flux density bins. Mandal et al. (2021) explored several combinations of parameters for Eqs. 5.10 and 5.11 that differ from those original proposed by Windhorst, Mathis & Neuschaefer (1990). In particular, they find that the integral size distribution of their low-frequency (150 MHz) source sample is better described when a steeper function with $q = 0.8$ is assumed. We explored the range $q = 0.62 - 1$, finding that our sources are better described by different values of q, depending on the flux density bin, as shown by the green and blue dash-dotted line in Fig. 5.5. We decided to assume $q = 1$ in the estimation of the resolution bias, and included the factored uncertainties associated to flatter slopes (down to $q = 0.62$) into a systematic error term, when correcting the source counts for resolution bias (Sect. 5.5). As shown by Prandoni et al. (2001a), the correction to be applied is:

$$C_{\rm res} = 1/[1 - h(> \Theta_{\rm lim})] \tag{5.13}$$

where $\Theta_{\rm lim}$ is the upper limit of the angular size above which the catalogue is incomplete, defined as $\Theta_{\rm lim} = \max[\Theta_{\rm min}, \Theta_{\rm max}]$.

5.4.2 Eddington bias

In presence of a non-uniform flux density distribution, the source flux densities do not follow a pure Gaussian noise distribution. In particular, if the true source distribution decreases with increasing flux density, the flux densities tend to be boosted and the probability to detect a source below the detection threshold is higher than the probability to miss a source above the threshold, artificially boosting the detection fraction. This is the so-called Eddington bias (Eddington, 1913). One approach to correct for the Eddington bias consists in rescaling the measured fluxes to their intrinsic values, before deriving the number counts. A maximum likelihood solution for the true source flux density can be defined as follows (Hales et al. 2014a, and references therein):

$$S_{\rm true} = \frac{S_{\rm meas}}{2}\left(1 + \sqrt{1 - \frac{4\gamma}{\rm S/N^2}}\right) \tag{5.14}$$

where $\gamma = \gamma(S)$ is the exponent of the intrinsic number count distribution at a given flux density, modeled by a power-law ($d{\rm N}/d{\rm S} \sim S^{-\gamma}$). The slope of the counts can be modeled from empirical polynomial fits of the observed counts. There are several fits available in the literature. Following Mandal et al. (2021), in this work we used as a fiducial model the sixth-order polynomial fit by Bondi et al. (2008), and we included the factored uncertainties associated to other fits into a systematic error term, when correcting

ΔS [mJy] (1)	$\langle S \rangle$ [mJy] (2)	N_S (3)	dN/dS S$^{2.5}$ [sr^{-1}Jy$^{1.5}$] (4)	σ^- (5)	σ^+ (6)	Sys$^-$ (7)	Sys$^+$ (8)
0.019 – 0.027	0.023	169	2.35	0.18	0.19	0.43	0.41
0.027 – 0.038	0.032	266	3.85	0.24	0.25	0.48	0.68
0.038 – 0.054	0.045	255	4.61	0.29	0.31	0.53	0.78
0.054 – 0.077	0.065	154	4.29	0.35	0.37	0.42	0.72
0.077 – 0.109	0.091	104	4.76	0.47	0.51	0.39	0.79
0.109 – 0.154	0.129	57	4.35	0.58	0.65	0.32	0.72
0.154 – 0.217	0.183	29	3.70	0.69	0.81	0.26	0.61
0.217 – 0.307	0.258	17	3.63	0.88	1.09	0.23	0.59
0.307 – 0.435	0.365	16	5.77	1.44	1.80	0.39	0.93
0.435 – 0.615	0.517	7	4.29	1.62	2.23	0.34	0.71
0.615 – 1.229	0.869	10	6.549	2.07	2.73	0.48	1.08
1.229 – 2.459	1.739	8	14.71	5.20	7.04	0.98	2.39
2.459 – 4.918	3.477	3	15.53	8.44	15.11	0.97	2.52
4.918 – 19.670	9.835	3	35.79	19.45	34.84	3.14	5.30
19.670 – 78.680	39.340	2	180.3	116.30	237.90	6.11	26.23

Table 5.2: 1.5 GHz source counts as derived from our survey. (1) Flux density interval. (2) Flux density geometric mean. (3) Number of detected sources. (4) Differential counts normalized to a non evolving Euclidean model. (5) and (6) Poissonian errors on the normalized counts. (7) and (8) Systematic errors, accounting for different modeling of resolution and Eddington bias corrections (see § 5.4.1 and 5.4.2 for more details).

the source counts for the Eddington bias (see Mandal et al. 2021 for more details).

5.5 Source counts

The 1.5 GHz J1030 differential source counts, normalized to a non-evolving Euclidean model ($S^{2.5}$), are listed in Table 5.2 and shown in Fig. 5.6, where they are rescaled to 1.4 GHz assuming a spectral index $\alpha = 0.7$ (blue squares bordered in black). Each source has been weighted by the reciprocal of its visibility area. The counts were corrected for the systematic errors as described in Sects. 5.2 and 5.4. The uncertainties associated with such corrections are factored into systematic error terms (see Sys$^-$ and Sys$^+$ columns in Table 5.2). Our source counts are compared with others available from literature, as shown in Fig. 5.6. The comparison counts come from a number of wide-area (>> 1 deg^2) surveys taken at 1.4 GHz or at frequencies not far from 1.4 GHz, to minimize systematic errors introduced when rescaling the counts to 1.4 GHz. Unless stated differently, the rescaling has been done by assuming $\alpha = 0.7$, as for the J1030 survey. These surveys are: the FIRST survey (White et al. 1997), the 943.5 MHz EMU Pilot Survey (EMU-PS; Norris et al. 2021), the SDSS STRIPE-82 mosaic (Heywood et al. 2016), the ATESP survey (Prandoni et al. 2001a), the Westerbork Lockman Hole mosaic (LHW; Prandoni et al. 2018), the Phoenix Deep Survey (PDF; Hopkins et al. 2003), the 3 GHz JVLA-COSMOS project (rescaled to 1.4 GHz by Smolčić et al. 2017b, by exploiting measured

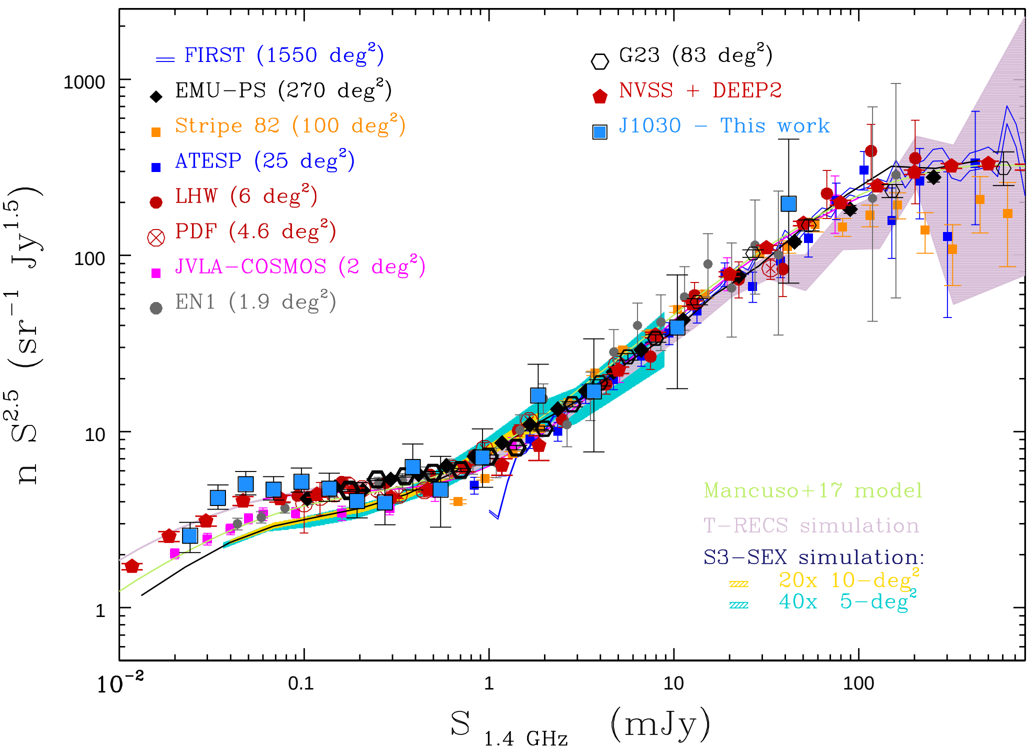

Figure 5.6: Normalized differential source counts derived from the J1030 radio source catalogue (blue squares bordered in black). The counts have been rescaled from 1.5 GHz to 1.4 GHz by assuming $\alpha = 0.7$. Vertical bars represent the squared sum of Poissonian errors (computed following Regener 1951) and systematic errors on the normalized counts. Also shown for comparison are the counts derived from a number of wide-field (>> 1 deg^2) surveys. All the surveys shown in this plot are taken at 1.4 GHz or at frequencies not far from 1.4 GHz, to minimize systematic errors introduced when rescaling the counts to 1.4 GHz. Unless stated differently, the rescaling has been done by assuming $\alpha = 0.7$, as for the J1030 survey. The surveys are listed in the legend and in the text. The yellow and light blue shaded areas illustrate the predicted cosmic variance effects for survey coverages of 5 and 10 sq deg respectively. They have been obtained by splitting the S3-SEX simulation of Wilman et al. (2008) (covering 1×200 deg^2, see black line) in forty 5-deg^2 and twenty 10-deg^2 fields respectively. The 25 deg^2 medium tier of the more recent T-RECS simulations (Bonaldi et al. 2019) is represented by the violet shaded area. Finally, the counts derived from the Mancuso et al. (2017) radio source evolutionary model are indicated by the light green solid line.

source spectral indices, whenever available), the 610 MHz survey of the ELAIS-N1 (EN1) field (Ocran et al. 2020), the 887.5 MHz counts obtained in the GAMA 23 (G23) field with ASKAP (Gurkan et al. subm.). Also shown are the recent counts obtained by Matthews et al. (2021) by combining the NVSS and the 1.2 GHz MeerKAT DEEP2 field (1 deg^2), which span eight decades of flux density.

Another interesting comparison is the one with simulations derived by combining evolutionary models of RL AGN, SFG and RQ AGN. In particular we show the 1.4 GHz counts derived from the recent modeling of (Mancuso et al., 2017, light green solid line), the 25 deg^2 Tiered Radio Extragalactic Continuum Simulation (T-RECS, pink shaded area, Bonaldi et al., 2019), as well as the source counts derived from the semi-empirical sky simulation developed in the framework of the SKA Simulated Skies project (S3-SEX, black solid line, Wilman et al., 2008, 2010). The role of cosmic variance is well illustrated by the yellow and light blue shaded areas. They have been obtained by splitting the S3-SEX simulation of Wilman et al. (2008) (covering 1×200 deg^2, see black line) in forty 5-deg^2 and twenty 10-deg^2 fields respectively. Our counts are taken over a significantly smaller field (0.2 deg^2), so larger deviations may be expected. Conversely Fig. 5.6 clearly shows that our source counts, which are among the deepest available so far, are in very good agreement with other determinations derived from wider surveys. Particularly they provide an excellent match (i.e. within 1σ) to the most recent surveys (Matthews et al., 2021) and models/simulations (Bonaldi et al., 2019).

5.6 Notable sources

Thanks to their depth, our novel 1.5 GHz J1030 JVLA observations allowed us to detect several interesting sources, as discussed in the following.

5.6.1 SDSS J1030+0524 QSO at $z = 6.3$

We detected, for the first time in the radio-band, the $z = 6.3$ SDSS J1030+0524 QSO at the center of the field (see Chapter 2; the JVLA emission is shown in the inset of Fig. 5.7). The measured observed-frame flux density is $S_{1.5\ \mathrm{GHz,\ obs}} = 25 \pm 5\ \mu$Jy, corresponding to a 1.4 GHz rest-frame luminosity of $L_{1.4\ \mathrm{GHz,\ rest}} = 4.3 \pm 0.2 \times 10^{24}$ W/Hz, assuming a radio spectral index of 0.7.

Based on the shallower 1.4 GHz VLA observations presented by Petric et al. (2003), where the source was undetected down to a 3σ upper limit of 60 μJy, Bañados et al. (2015) estimated a 3σ upper limit for the 5 GHz rest-frame integrated luminosity, $\log(L_{5\ \mathrm{GHz,\ rest}}) < 7.9\ L_\odot$. Furthermore, from the QSO 3.6 μm flux density ($74 \pm 3\ \mu$Jy, Leipski et al., 2014), Bañados et al. (2015) derived the UV-rest-frame luminosity ($L_{4400\ \mathrm{Å,\ rest}} \sim 12.91\ L_\odot$) assuming an optical spectral index of -0.5. On the basis of the UV-rest-frame flux density $f_{4400\ \mathrm{Å}}$ and the upper limit to the 5 GHz rest-frame flux density $f_{5\ \mathrm{GHz}}$, an upper limit for the optical radio-loudness was derived, i.e. $R_O = f_{5\ \mathrm{GHz}}/f_{4400\ \mathrm{Å}} < 1.5$. This upper limit is well below the $R_O = 10$ threshold, that marks the division between radio-quiet and radio-loud quasars, following the definition by Jiang et al. (2007).

Thanks to our detection we can now securely estimate the optical radio-loudness of this object: from $S_{1.5\ \mathrm{GHz,\ obs}}$ we derive a rest-frame $\log(L_{5\ \mathrm{GHz,\ rest}}) = 7.56 \pm 0.09\ L_\odot$ and a radio loudness $R_O = 0.62 \pm 0.12$. The radio loudness of the SDSS J1030+0524 QSO

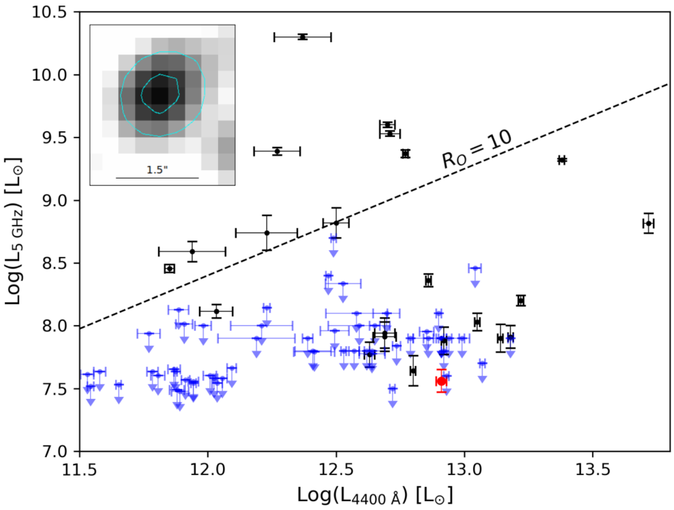

Figure 5.7: Rest-frame optical luminosity at 4400 Å vs. rest-frame radio luminosity at 5 GHz for known quasars at z~6 (Bañados et al. 2015 and references therein; Bañados et al. 2018; Liu et al. 2021; Sbarrato et al. 2021). Black points mark radio detected sources, while blue points indicate radio undetected ones, for which 3σ upper limits are reported. The red point marks the position of the SDSS J1030+0524 QSO, based on our JVLA detection. The black dashed line indicates the radio-loudness value $R_O = 10$, set as a threshold between radio-quiet and radio-loud AGN (Jiang et al., 2007). The inset shows the JVLA emission, with cyan contours starting at the 3σ level and increasing with a $\sqrt{3}$ geometric progression. The black bar indicates the angular scale of the image.

is compared to the one of the other known quasars at $z \gtrsim 6$ in Fig. 5.7 (Bañados et al. 2015; Bañados et al. 2018; Liu et al. 2021; Sbarrato et al. 2021). SDSS J1030+0524 is the faintest radio-detected QSO and the second most radio-quiet QSO discovered so far at $z \gtrsim 6$.

It is interesting to note that this RQ AGN is at the center of a giant assembling structure (Mignoli et al., 2020), the most distant known to date around a SMBH. Several works have shown that high-z ($z \gtrsim 1.5-2$) proto-clusters preferentially assemble around powerful RL-AGN (e.g. Pentericci et al., 1997; Venemans et al., 2007; Miley & De Breuck, 2008; Overzier, 2016; Gilli et al., 2019), possibly up to $z \sim 5.2-5.8$ (Overzier et al., 2006; Zheng et al., 2006). In addition, Liu et al. (2021) have shown that the radio-loud fraction (RLF) of z~6 quasars is consistent with the fraction observed at low-redshift (~10%), suggesting no evolution of the RLF for optically selected quasars across cosmic time. The link between radio loudness and high-z overdensities is still an open issue, as well as proto-BCG radio properties and their evolution across cosmic time. Further wide-field deep observations around high-z QSOs are needed to reach firmer conclusions.

Band (1)	M_{AB} (2)	Instrument (3)	Reference (4)
r	>26	LBT/LBC	Morselli et al. (2014)
i	>25.5	LBT/LBC	”
z	26.6 ± 0.2	HST/ACS	Stiavelli et al. (2005)
Y	25.4 ± 0.5	CFHT/WIRCam	Balmaverde et al. (2017)
J	23.7 ± 0.2	CFHT/WIRCam	”
H	23.5 ± 0.2	HST/WFC3	D'Amato et al. (2020a)
K	22.6 ± 0.1	CTIO/ISPI	Quadri et al. (2007)
CH1	20.8 ± 0.7	Spitzer/IRAC	Annunziatella et al. (2018)
CH2	20.6 ± 0.5	Spitzer/IRAC	”

Table 5.3: Optical/IR photometry of $a2$. (1) Observed band. (2) AB magnitude. The upper limits are given at the 5σ level. (3) Observing instrument. (4) Reference of the measurements.

5.6.2 Radio-detected $z = 1.7$ proto-cluster members

We report the detection of two members of the proto-cluster at $z = 1.7$. Both are associated with ALMA-detected galaxies: $a2$ and $a3$ (see Fig. 3.1 and 4.1). Their 1.5 GHz flux densities are $S_{1.5\ \mathrm{GHz,\ obs}}$ ~28 μJy and ~13 μJy respectively. Assuming that the measured 1.5 GHz flux densities are fully ascribed to star-formation activity, we can derive radio-based SFRs. This is done by exploiting the relation presented by Novak et al. (2017, assuming a Chabrier IMF), and results in SFR ~200 $M_\odot$/yr for $a2$ and ~50 $M_\odot$/yr for $a3$. While the latter value is consistent with the SFR range derived from the SK-law (see Eq. 3.4 in Chapter 3), the former is 4 × larger (SFR_{SK} ~40 – 60 $M_\odot$/yr), suggesting a possible AGN origin of (at least part of) the radio emission in $a2$. We hence derived another independent SFR estimate for $a2$, by performing a SED fitting of the source and exploiting the broad-band coverage of the J1030 field[1]. In Table 5.3 we report the photometry of the source in each available band, the observing instrument and the references of the public data. The SED fitting was done with the *Hyperz* code (Bolzonella, Miralles & Pelló, 2000). The best fit resulted in a stellar mass of $\log(M_*/M_\odot) = 10.75 \pm 0.25$ and in an upper limit to the SFR (at the 90% significance level) of 43 $M_\odot$/yr, in good agreement with the SFR range derived through the SK law, and based on the cold molecular gas content of the galaxy. The low value of the corresponding sSFR upper limit ($<7 \times 10^{-10}$ yr^{-1}) is consistent with the typical sSFR of normal star-forming galaxies at the same redshift (Schreiber et al., 2015). All this strongly argues for AGN emission being at the origin of the observed 1.5 GHz flux density. If confirmed, $a2$ would be the second AGN detected in the structure, located closely (projected distance ~80 kpc) to the assembling proto-BCG.

[1] We note that $a3$ is associated with the brighter of two blended galaxies (see HST cut-out in Fig. 3.1). The optical/IR magnitudes are therefore unreliable and a SED fitting for this source is not possible.

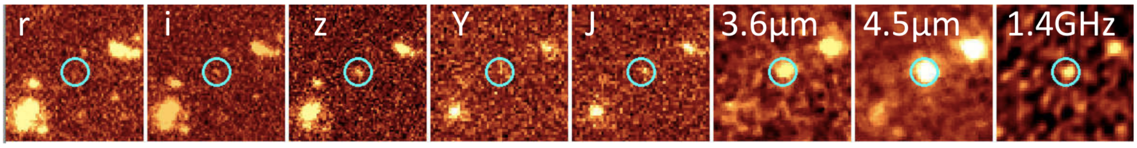

Figure 5.8: Multi-λ cutouts (15"x15" each) centered on source ID 24071 (cyan circle). See Table 2.1 for references.

5.6.3 An obscured AGN candidate at cosmic dawn

Despite most of the accretion onto SMBHs in the Universe is obscured, and even more so at early times, no reliable example of obscured AGN has been yet detected in the first billion year of the Universe, i.e. at $z \gtrsim 6$. To date, ~300 quasars have been discovered at $z > 5.7$ (Bañados et al., 2016), all free from obscuration. One of the 21 LBGs selected by Balmaverde et al. (2017) as candidate members of the overdensity assembling around the J1030 QSO at $z = 6.3$ (see Chapter 2) is detected for the first time in our JVLA image ($S_{1.5\ \mathrm{GHz,\ obs}}$ ~27 μJy). The multi-band data of this source (ID 24071 in Balmaverde et al. 2017 catalogue) is presented in Fig. 5.8. Balmaverde et al. (2017) measured a photometric $z_{\mathrm{phot}} = 5.62^{+0.15}_{-0.15}$ for this source. Assuming this redshift, the observed 1.5 GHz flux density would imply a very large radio-based SFR ($\gtrsim$1000 $M_{\odot}$/yr), which in turn would imply flux densities of the order of 15–30 mJy at the peak of dust emission, i.e. at ~160 μm rest-frame. At $z = 5.6$ this emission gets redshifted to the 1 mm band, but the source is not detected at 1.1 mm by AzTEC down to a 5σ flux limit of ~2.6 mJy (Zeballos et al., 2018), suggesting the radio emission is to be ascribed to a central AGN. This source is not even detected in X-rays by *Chandra*, possibly due to obscuration. These features make ID 24071 one of the most promising obscured AGN candidate at $z \gtrsim 5.6$; further spectroscopic observations aimed at securing the redshift of this source, will ultimately confirm/reject this scenario. To this extent, our group has recently proposed and obtained CII observations with ALMA and Ly-α observations with LBT/MODS. We should hence have soon a secure spectroscopic redshift for ID 24071.

5.7 Radio-X-ray luminosity relation

In the following we investigate the relation between the X-ray and radio luminosity on a sub-sample of the X-ray source catalogue presented by Nanni et al. (2020). In particular we focused on the sub-sample of sources with spectroscopic and/or photometric redshift determinations. Based on ~500 ks *Chandra* observations, Nanni et al. (2020) built-up a catalogue of 256 total sources in the central part of the J1030 field (see cyan solid line in Fig. 5.1). By exploiting the UV to FIR multi-wavelength coverage of the field, Marchesi et al. (2021) performed the SED fitting for 243 of the 256 X-ray sources, deriving their photometric redshift (see Chapter 2). In addition, they obtained spectroscopic redshifts for 123 of such sources, as well as spectral classification. They grouped the sources in four classes: BL- and NL-AGN (see § 1.1.3), Emission Line Galaxies (ELG) and Early-type Galaxies (ETG).

We matched the 243 X-ray sources analyzed by Marchesi et al. (2021) with our radio source catalogue. Since Nanni et al. (2020) identified the optical/near-IR counterparts of the X-ray sources (through likelihood-analysis association), we used the optical positions of the sources to perform the match. We used a matching radius of 1.5 arcsec, which appears appropriate from the analysis of the optical/radio position separation distribution. We note that the positional errors of both the optical and radio positions are >10× smaller than the chosen matching radius, and that we visually inspected the associations on optical and radio image cutouts. In total, we found 96 matches. Fifty-six of the 96 detected sources have spectroscopic redshift and spectral classification. For the 147 X-ray sources without a catalogued radio counterpart, we measured the 3σ 1.5 GHz flux density limit, based on the local noise at the source position. Despite the small X-ray-selected sample, the availability of secure spectroscopic redshifts and source classification allowed us to explore the radio/X-ray properties for different classes of sources over a wide range of cosmic time. The redshift distribution of the analyzed 243 sources is shown in Fig. 5.9. Most of them have redshift in the range $0 \lesssim z \lesssim 3$.

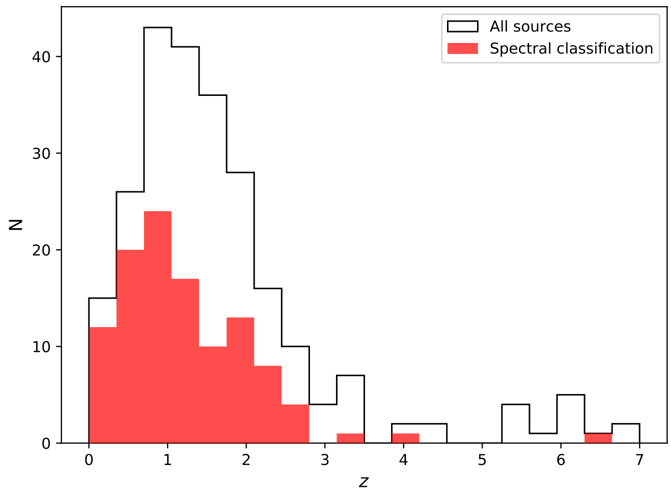

Figure 5.9: Redshift distribution of the 243 X-ray sources (black solid line) used for our radio/X-ray analysis, in redshift bins of 0.35. The distribution of the 123 sources having spectroscopic classification (and redshift) is shown in red.

We converted the observed 1.5 GHz flux densities ($S_{1.5\ \mathrm{GHz,obs}}$) to 1.4 GHz rest-frame luminosities as follows:

$$L_{1.4\ \mathrm{GHz}} = 4\pi\, D_L^2 \times \frac{S_{1.5\ \mathrm{GHz,obs}}}{\nu_{\mathrm{obs}}^{\alpha}} \times \left(\frac{\nu_{\mathrm{rest}}}{1+z}\right)^{1+\alpha} \quad \mathrm{erg\ s^{-1}} \tag{5.15}$$

where D_L is the luminosity distance and α is the spectral index, assumed equal to 0.7. All quantities are expressed in cgs units. The intrinsic, de-absorbed X-ray luminosities measured in the 2-7 keV rest-frame and extrapolated up to 10 keV assuming a photon index $\Gamma = 1.8$ (i.e., the average intrinsic value for AGN, see Piconcelli et al., 2005).

In Fig. 5.10 we show the position of our sources in the radio–X-ray luminosity plane. Sources are color-coded based on source type (left panel) and on source redshift (right panel). Radio detected sources are indicated by the circles, while radio upper limits are indicated by the triangles. Sources without spectral classification in the left panel are indicated in light-grey. Also shown are different radio/X-ray correlations from the literature, which refer to different types of objects. For SFG, we show the relation found by Mineo et al. (2014) from a sample of $z \sim 0 - 1.3$ sources. For RL AGN we report the relation found by Canosa et al. (1999, green line) in the local Universe. We note that the (narrow line) FRII galaxy at the center of the proto-cluster at $z = 1.7$ is located above the local RL AGN relation. Finally, the magenta line represents the radio-to-X-ray relation found for a sample of local ($z \lesssim 0.35$) X-ray-selected Seyfert galaxies by (Panessa et al., 2015, slope $\sim$1.1). We note that the solid part of the lines marks the X-ray luminosity range over which the relations have been derived, while the dotted part represents the extrapolation at all X-ray luminosities.

We note that both the radio and X-ray luminosities increase with redshift, as expected in flux-limited samples. However different classes of objects tend to occupy different regions of this plane. NL-AGN and ELG are preferentially clustered around intermediate values of L_X, in the range $42.5 \lesssim \log(L_X) \lesssim 43.5$; while ETG and BL-AGN are typically located at lower and higher X-ray luminosities, respectively. We also notice that ETG and BL-AGN show a clear correlation between the radio and X-ray luminosity, suggesting a common origin for the emission in the two bands, likely ascribed to nuclear emission. This does not seem to be the case for ELG, which show a flat radio luminosity distribution. NL-AGN have a less clear behaviour, with low L_X ones being similar to ELG and high L_X ones being similar to BL-AGN.

We investigated the significance of the radio/X-ray luminosity correlation of the ETG and AGN sub-sample, accounting for upper limits through survival analysis. Specifically we used the ASURV tool (Feigelson & Nelson, 1985; Isobe, Feigelson & Nelson, 1986; Lavalley, Isobe & Feigelson, 1992), and computed the Spearman rank correlation coefficient (Spearman, 1904), finding $\rho = 0.475$. The resulting probability that the correlation is not present is negligible (null hypothesis, $P_{\rm nh} < 10^{-5}$). We repeated the analysis on the whole sample of 243 X-ray sources, to test the effect of including sources without spectroscopic classification. Despite $P_{\rm nh}$ remains negligible ($< 10^{-5}$), we found a lower value $\rho = 0.341$. The Spearman coefficient increases for positive correlations (up to +1 for a perfect monotone increasing function), while a value of 0 means no correlation. This implies a weaker correlation with respect to the ETG/AGN sub-sample, meaning that sources without a spectroscopic classification likely include objects where radio and X-ray emissions do not have a common nuclear origin. Finally we performed the survival analysis considering only ELG. This results in a high probability of no correlation

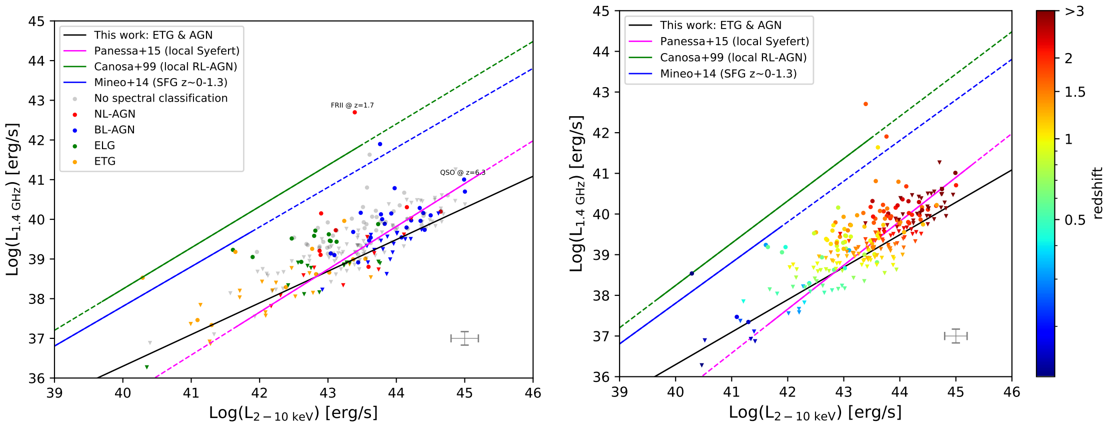

Figure 5.10: *Left*: X-ray intrinsic luminosity in the 2–10 keV band vs. rest -frame 1.4 GHz radio luminosity for our sample. NL-AGN, BL-AGN, ETG and ELG are indicated by blue, red, orange and green symbols, respectively. The light-grey symbols mark the sources without a spectroscopic classification. Circles mark radio-detected sources, while triangles represent 3σ upper limits for the undetected ones. Typical uncertainties on the radio (X-ray) luminosity is indicated by the vertical (horizontal) errorbar in the bottom-right corner. The solid black line is the correlation presented in this work (slope ~ 0.8; see text for more details). The magenta line is the Panessa et al. (2015) correlation found for local Syefert galaxies (slope ~ 1.1), while the blue line is the relation for $0 \lesssim z \lesssim 1.3$ SFG (Mineo et al., 2014). The green line is the relation found for local radio-loud AGN by Canosa et al. (1999). The solid part of the lines represent the X-ray luminosity range in which they have been derived; the dashed part of the lines represent extrapolations to the entire luminosity range covered of our sample. Notable sources, i.e. the $z = 6.3$ QSO and the $z = 1.7$ FRII galaxy, are labeled in the figure. *Right:* Same as in left panel, but sources are color-coded based on their redshift (right color-bar): 123 sources have spectroscopic redshifts, the other 120 source have photometric redshift.

between L_R and L_X ($P_{\rm nh} \sim 0.8$). Despite the small size of the sample (13 objects), this finding suggests that ELG include a significant fraction of sources where radio and X-ray luminosities are to be ascribed to different emission mechanisms (we will return on this point below).

To quantify the correlation for the AGN-driven sub-sample, we applied the regression method by Buckley & James (1979) using ASURV, to take into account upper limits; we found a linear correlation of the form:

$$\log(L_R) = (0.79 \pm 0.12)\ \log(L_X) + 4.38 \tag{5.16}$$

where L_R and L_X are expressed in erg/s. We note that the slope of this correlation is consistent, at the 1σ level, with the classical fundamental plane value (Merloni, Heinz & di Matteo 2003) and with values typically found for samples of low luminosity AGN ($\sim 0.5 - 0.7$; Dong et al., 2021). This slope is commonly interpreted as signature of a radiatively inefficient accretion process, where the radio emission is ascribed to the jet's synchrotron and the X-ray emission is mainly due to IC scattering from the ADAF region

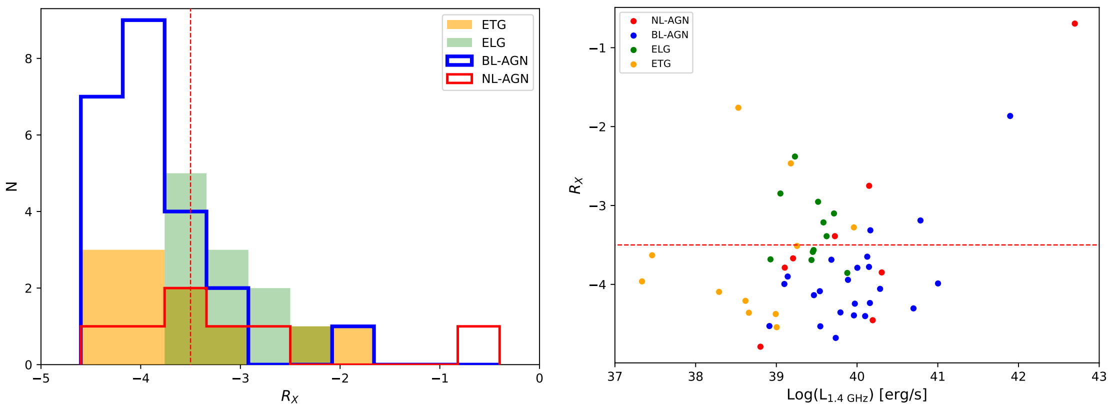

Figure 5.11: *Left*: Radio-loudness distribution of the radio-detected X-ray sources, color-coded by their spectral classification. The $R_X = 3.5$ threshold separating RQ from RL AGN (Lambrides et al., 2020) is indicated by the red dashed vertical line. The radio-loudest source is the FRII galaxy at $z = 1.7$. *Right:* Radio-loudness of the radio-detected X-ray sources as a function of 1.4 GHz rest-frame luminosity, color-coded by object class.

(see § 1.1.4 and § 1.1.8 for more details). Indeed we note that the slope of our relation is strongly constrained by the X-ray faint ETG, which are most likely inefficient accretors. On the other hand, we note that X-ray luminous ($\log(L_X) \gtrsim 43.5$) AGN tend to lie above the relation defined above (Eq. 5.16), and their distribution is scattered around the steeper Panessa et al. (2015) relation (slope ~1.1), found for nearby Seyfert galaxies. This suggests that in these objects an efficient accretion flow may feed the central SMBH, and the radio and X-ray emission are ascribed to the jet's synchrotron and SSC mechanisms, respectively (see § 1.1.4 and § 1.1.8 for more details). We point out that our sources span a much wider redshift range ($0 \lesssim z \lesssim 3$, and up to $z = 6.3$ for the SDSS J1030+0524 QSO) than Panessa et al. (2015) sample, suggesting that local Seyfert (both Type I and Type II) and $z \geq 1$ radio-quiet NL- and BL-AGN may have similar radio/X-ray properties.

Most ELG lie between the AGN and the SFG relations, meaning that they do not seem to be described by neither of them. Indeed, our ELG sample shows high ($> 10^{42}$ erg/s) L_X values, typical of AGN, and $L_R < 10^{40}$ erg/s, which are high, but still consistent with star-formation activity. Hence the radio emission of these objects is probably dominated by star-formation, while the X-ray emission is in excess to what expected from star formation, and is ascribed to the AGN. In fact, it is also possible that in these objects both star formation and AGN processes contribute to the radio and X-ray emissions, considering that their redshift range ($1 \lesssim z \lesssim 2$) corresponds to cosmic noon, where both activities peak.

In Fig. 5.11 (left panel) we show the radio loudness $R_X = \log(L_R/L_X)$ distribution for the sub-sample of radio-detected X-ray sources. Different colors correspond to different spectral classes. We note that the R_X distribution peaks at ~ -4, and that most of the sources (75%) have $R_X \lesssim -3.5$. Lambrides et al. (2020) set this value as a threshold to separate RL and RQ AGN, based on the analysis of a low-luminosity AGN sample (see also Terashima & Wilson, 2003). According to Lambrides et al. (2020) threshold, most of our objects are RQ, from local faint ETG to high-z powerful BL-AGN. The radio-loudest object corresponds to the FRII galaxy at the center of the proto-cluster at $z = 1.7$. We note, however, that most ELG display rather high R_X values ($\gtrsim -3.5$), i.e. they appear as RL. This is in apparent contradiction with a scenario where radio emission is mostly ascribed to star formation, as proposed above. In the right panel of Fig. 5.11 we show R_X as a function of L_R for the radio-detected X-ray sources. We note that ELG classified as RL show a radio luminosity comparable with those classified as RQ and generally lower than that of many RQ AGN. This seems to confirm that the radio loudness parameter is not meaningful for this class of objects, where different mechanisms power the radio and the X-ray emission.

Chapter 6

Conclusions and future perspectives

6.1 Summary and conclusions

A galaxy overdensity assembling around a powerful FRII type HzRG at $z = 1.7$ was discovered at the center of the J1030 field by G19, who unveiled the presence of eight galaxies (including the HzRG host) within a projected distance of 800 kpc and in the redshift range 1.6871 – 1.6987, on the basis of VLT/MUSE and LBT/LUCI spectroscopic observations. The J1030 field was originally observed at 1.4 GHz by the VLA (Petric et al., 2003), with a resolution of ~1.8 arcsec and an rms of ~15 μJy. Such observations revealed the extended emission of the FRII radio galaxy and its complex morphology. By means of deep *Chandra* observations of the field, the presence of X-ray diffuse emission was also discovered, mostly coinciding with the extended radio emission of the HzRG lobes, Eastern jet and nucleus (G19). Remarkably, four of the overdensity members lie in an arc-like shape at the edge of the main X-ray component, located around the Eastern lobe of the HzRG. G19 proposed that the X-ray diffuse emission arises from an expanding bubble of gas that is shock-heated by the FRII jet, triggering the star formation in the surrounding galaxies. If confirmed, this would be the first evidence of positive AGN feedback on multiple galaxies at hundreds of kiloparsec distance.

In this Thesis we analyzed novel interferometric observations of the J1030 field, carried out with ALMA and JVLA. We mainly aimed at further investigating the proto-cluster, by searching for new members and studying their gas content, as well as the diffuse radio emission of the HzRG. Coupling these observations with the ancillary data available for the J1030 field, we also looked for signatures of interaction with the ICM in order to support/reject the positive feedback scenario. Thanks to the sensitivity of our JVLA observations, we also extracted one of the deepest radio samples available to date. We exploited this dataset to study the radio/X-ray luminosity correlation for a sub-sample of the X-ray sources in the overlapping *Chandra* field. The main results of our work are summarized as follows:

– in Chapter 3 we presented ALMA Band 3 observations of the CO(2→1) line transition of the region around the HzRG. We developed a new blind-search code that automatically performs the detection of emission lines in data-cubes, on the basis of spectral, spatial and reliability criteria. We reported the discovery of three new gas-rich ($M_{H2} \sim 1.5 - 4.8 \times 10^{10}$ $M_{\odot}$) galaxies (named $a1$, $a2$ and $a3$), leading to a total of 11 confirmed overdensity members within a projected distance of $\sim$ 1.15 Mpc and in a redshift range of $\Delta z = 0.012$. In addition, we discovered a large molecular gas reservoir ($M_{H2} \sim 2 \times 10^{11}$ $M_{\odot}$) distributed around the host galaxy of the HzRG (named $a0$); we fitted the CO emitting region with a 2D-Gaussian model of deconvolved major and minor axis of 27 ± 17 kpc and 17 ± 13 kpc, respectively. The CO velocity map unveils a rotating structure that appears perpendicular to the radio jets, at least in projection. The associated ISM column density, assuming a simple edge-on disk orientation (as proposed by G19 on the basis of the VLA image), is $N_{H,ISM} \sim 5.5 \times 10^{23}$ cm^{-2}, implying that the ISM may significantly contribute to the total nuclear obscuration measured in the X-rays ($N_{H,X} \sim 1.5 \times 10^{24}$ cm^{-2}; G19), as found in the past for high-z obscured QSOs (e.g., D'Amato et al., 2020b).
All ALMA sources have a dust-reddened counterpart in HST images (bands i, z, H), while we do not detect any molecular gas reservoir around the known UV-bright, star-forming members discovered by MUSE, for which we derived molecular gas upper limits of $M_{H_2} \leq 2.8 - 4.8 \times 10^{10}$ M$_{\odot}$. By exploiting the Schmidt-Kennicutt relation between the SFR and molecular gas surface densities, we derived SFRs in the range ~5 – 100 $M_{\odot}$/yr for the new members discovered by ALMA. Such SFRs are consistent with those expected for main-sequence galaxies at similar redshift.
Based on velocity dispersion and galaxy overdensity arguments, we estimated a total mass of $\geq 3 - 6 \times 10^{13}$ $M_{\odot}$ for the overall system; considering the evolutionary paths presented by Chiang, Overzier & Gebhardt (2013) for both most massive dark matter halos and galaxy overdensities, we conclude that this structure will likely evolve into a $\gtrsim 10^{14}$ $M_{\odot}$ cluster at $z = 0$. We exploited the exquisite multi-wavelength coverage of the J1030 field to perform a SED-fitting of the HzRG host galaxy and measure its main physical parameters. From the best-fitting model we measured an AGN bolometric luminosity $L_{\rm bol,\,AGN} \sim 1.1 \times 10^{46}$ erg/s, a IR luminosity $L_{8-1000\,\mu\rm m} \sim 3.7 \times 10^{12}$ L$_{\odot}$ (24% of which ascribed to the AGN), and a stellar mass $M_{*} \sim 3.7 \times 10^{11}$ M$_{\odot}$. The SFR corresponding to the AGN-subtracted IR luminosity is ~570 M$_{\odot}$/yr. The HzRG is located at the center of the projected spatial distribution of the structure members and shows a velocity offset from the peak of the protocluster members' redshift distribution, which is well within the overall velocity dispersion of the structure. All of these results, coupled with the large amount of gas around the FRII, its stellar mass, SFR, and powerful radio-to-X-ray emission, suggest that this source is the likely progenitor of the future BCG.

The high sSFR = 1.5 ± 0.5 Gyr^{-1} derived for the FRII host galaxy classifies this object as a starburst galaxy when compared with other SFG at the same redshift (Schreiber et al., 2015), implying that the proto-BCG is currently being observed during the brief phase (few $\times 10^8$ yr, Lapi et al. 2018) of its major stellar mass building-up. Indeed, the high SFR implies that the molecular gas reservoir will be depleted in few 10^8 yr.
ALMA observations have also revealed the presence of 3.3 mm continuum emission associated with the HzRG core. The measured flux density nicely agrees (within 1σ) with the 3.3 mm emission expected from the best SED-fitting model, and is significantly higher ($> 4\times$) than the expected synchrotron emission, as extrapolated from the 1.5 GHz emission and assuming $\alpha = 0.7$. These findings strongly argue for a scenario in which the dust is primarily responsible for the observed flux density at 3 mm. However, we cannot rule out some contribution from synchrotron emission, when considering the large uncertainties on all the involved quantities and relations.
The results presented in this Chapter have been published in D'Amato et al. (2020a, 2021).

– In Chapter 4 we presented very deep (median rms $\sim 3.5\ \mu$Jy/b) 1.5 GHz JVLA observations of the J1030 field. Such observations are mainly aimed at investigating the morphology of the proto-BCG and the radio properties of the $z = 1.7$ overdensity members. The JVLA total intensity image revealed significantly more extended emission in both lobes of the FRII HzRG than observed in the previous shallower VLA observations. The total measured flux density is $S_{1.5\text{ GHz, obs}} \sim 28$ mJy, corresponding to $S_{1.4\text{ GHz, obs}} \sim 30$ mJy, when assuming a spectral index $\alpha = 0.7$. This value is in excellent agreement with the value reported by the NVSS (30 mJy), and slightly larger than the one measured from the previous VLA observations ($S_{1.4\text{ GHz, obs}} \sim 27$ mJy). A revised estimate of the source size can be also provided, based on the full extent of the radio emission. The RG (deconvolved) major axis is measured to be 1.3 arcmin, which corresponds to a projection-corrected physical size of ~700 kpc (to be compared with the value of ~600 kpc reported by G19, based on the old VLA data). The new extended emission detected by the JVLA is mostly co-spatial with the X-ray diffuse emission observed around the FRII radio galaxy lobes; this supports the positive feedback scenario proposed by G19, either when we assume that the X-ray emission arises from shock-heated gas (as proposed by G19) or in the case of non-thermal IC-CMB–related emission.
Thanks to the high resolution of the new JVLA observations, we can better resolve the core and the base of the approaching jet of the HzRG. Thus, we can provide a more reliable estimate of the FRII radio galaxy inclination angle on the basis of jet and counter-jet length and flux density ratios, finding a value consistent with that previously derived from the old lower-resolution VLA observations (i.e., $\theta \sim 80°$).
With the discovery of a possible positive AGN feedback scenario promoting star

formation in multiple galaxies around the FRII RG (G19), we decided to explore the polarization properties of the RG. Polarization can indeed reveal signatures of interactions between the radio galaxy plasma and the surrounding proto-cluster ICM. However, since the analysis of the HzRG polarized emission was not in the original goals of the observations, we did not observe a polarization calibrator.
We developed an ad-hoc procedure to perform the polarization calibration of the JVLA observations, that exploits the flux/bandpass calibrator and the presence of a strong polarized source in the J1030 field, detected in the NVSS. This allowed us to produce polarization fraction images of the FRII RG in the two NVSS Intermediate Frequencies (IFs; two 42 MHz bands centered at 1365 MHz – IF1 – and 1435 MHz – IF2; Condon et al. 1998). We used the leakage signal of the flux calibrator to correct for the cross–hand delay, and the (unpolarized) flux calibrator signal to correct for the leakage. As for the calibration of the polarization angle and fractional polarization, we exploited the polarization parameters of the bright NVSS source, that we used as a calibrator. This led to successful imaging of the HzRG fractional polarization and polarization angle in the two IFs. We detect polarized emission in both FRII lobes. Both Eastern and Western spots feature a fractional polarization of 10%–20% and a magnetic field perpendicular to the jet, as typically found for classical FRII RGs. In general, in the extended regions of the FRII radio galaxy lobes, we notice an increased polarization fraction in correspondence of bending morphologies in total intensity. The orientation of the magnetic field also seems to follow the observed bendings. Considering that the source is seen at almost edge-on orientation, these observational features may suggest that these regions experience a compression and an alignment of the magnetic field, possibly associated with the impact with components of the ICM. We cannot exclude, however, that peculiar motions of the source within the overdensity are at the origin of the observed bendings in the lobes.
The results presented in this Chapter have been published in D'Amato et al. (2021, polarization analysis) and will be published in D'Amato et al. (subm., total intensity analysis).

– In Chapter 5 we presented the radio source catalogue extracted from the 1.5 GHz JVLA image of the J1030 field. The reached sensitivity (median rms $\sim 3.5\ \mu$Jy/b) makes J1030 one of the deepest radio fields to date. Using the PyBDSF tool, we extracted a catalogue of 1283 radio-sources with S/N > 5. At this threshold the reliability of the catalogue is 90% and the completeness is 70%. The catalogue gets $\sim$ 100% reliable and $>$ 80% complete at S/N $\gtrsim 5.5$. We derived the source counts as a function of flux density, by taking into account systematic effects, like catalogue incompleteness, resolution bias and Eddington bias, finding excellent agreement with recent determinations from wider samples.
Thanks to the depth of our observations, we detected for the first time in the radio-

band the $z = 6.3$ QSO SDSS J1030+0524 at the center of the field, which traces the most distant spectroscopically confirmed overdensity known to date (Mignoli et al., 2020). For this source, we measured a flux density of $S_{1.5\ \mathrm{GHz,\ obs}} = 25 \pm 5\ \mu$Jy, corresponding to a 1.4 GHz rest-frame luminosity $L_{1.4\ \mathrm{GHz,\ rest}} = 4.3 \pm 0.2 \times 10^{24}$ W/Hz, assuming a radio spectral index of 0.7. Coupled with the UV-rest-frame luminosity ($L_{4400\ \mathrm{Å,\ rest}} \sim 12.91\ L_{\odot}$) reported by Bañados et al. (2015), we derived an optical radio-loudness $R_O = 0.62 \pm 0.12$, which classifies this QSO as the faintest radio-detected QSO and the second most RQ AGN at $z \gtrsim 6$, discovered to date.
In addition, we detected for the first time in the radio-band two members of the $z = 1.7$ proto-cluster, namely two of the ALMA discovered sources ($a2$ and $a3$). As for the first source ($a2$), the SFR required to produce the observed flux density is $\sim$200 M$_{\odot}$/yr (Novak et al., 2017); we performed a SED fitting of the source, and derived a SFR <43 M$_{\odot}$/yr, in agreement with the values obtained from the molecular gas mass by means of the Schmidt-Kennicutt law ($\sim$40 – 60 M$_{\odot}$/yr), that are also consistent with the SFR of main-sequence galaxies with comparable stellar mass ($\log(M_*/\mathrm{M}_{\odot}) = 10.75 \pm 0.25$) at the same redshift (Schreiber et al., 2015; Genzel et al., 2015). Our findings strongly suggest that the observed radio flux density is owed to nuclear activity. The second source $a3$ has optical/IR emission contaminated from a nearby galaxy, preventing us to perform SED fitting. However, assuming again that the measured 1.5 GHz flux density ($S_{1.5\ \mathrm{GHz,\ obs}} \sim 13\ \mu$Jy) is ascribed to star-formation activity, we expect SFR $\sim$50 M$_{\odot}$/yr, fully consistent with the values of few tens of M$_{\odot}$/yr derived from the Schmidt-Kennicutt-law.
We detected, for the first time at 1.5 GHz, one of the 21 LBGs selected by Balmaverde et al. (2017) as candidate members of the overdensity assembling around the J1030 QSO at $z = 6.3$. For this source, Balmaverde et al. (2017) measured a photometric $z_{\mathrm{phot}} = 5.62^{+0.15}_{-0.15}$; at this redshift, the expected SFR from the measured radio flux density ($S_{1.5\ \mathrm{GHz,\ obs}} \sim 27\ \mu$Jy) is $\gtrsim$1000 M$_{\odot}$/yr. Assuming this redshift, the observed 1.5 GHz flux density would imply a very large radio-based SFR ($\gtrsim$1000 M$_{\odot}$/yr), which in turn would imply flux densities of the order of 15–30 mJy at the peak of dust emission, i.e. at $\sim$160 μm rest-frame. At $z = 5.6$, this emission gets redshifted to the 1 mm band, but the source is not detected at 1.1 mm by AzTEC down to a 5σ flux limit of $\sim$2.6 mJy (Zeballos et al., 2018), suggesting the radio emission is to be ascribed to a central AGN. This source is not even detected in X-rays despite the available deep *Chandra* observations, possibly due to obscuration. These features make this source one of the most promising obscured AGN candidates at $z \gtrsim 5.6$; further spectroscopic observation aimed at securing the redshift of this source will ultimately confirm/reject this scenario.
We finally exploited the availability of deep JVLA and *Chandra* datasets to investigate the relation between the X-ray and radio luminosity on a sub-sample of the X-ray catalogue presented by Nanni et al. (2020) (253 sources). In particular, we

focused on the sub-sample of 243 sources with photometric and/or spectroscopic redshift determinations presented by Marchesi et al. (2021). For the objects with available spectroscopy, spectral classification is also available. Spectral classes are: BL-AGN, NL-AGN, ELG and ETG. We matched the 243 X-ray sources analyzed by Marchesi et al. (2021) with our radio source catalogue, finding 96 counterparts. For the remaining 147 radio-undetected X-ray sources, we derived 3σ flux density upper limits at 1.5 GHz. We then derived the rest-frame 1.4 GHz luminosities (or luminosity upper limits), on the basis of either the spectroscopic (when available) or photometric redshift, assuming a radio spectral index of 0.7. Of the 96 (147) radio-detected (undetected) sources, 56 (67) have a spectroscopic redshift (mostly in the range $0 \lesssim z \lesssim 3$).
We explored the radio/X-ray properties of the spectroscopic sub-sample, by performing survival analysis to take into proper account radio upper limits. We found that the BL-AGN, NL-AGN and ETG can be described by the following radio–X-ray luminosity correlation: $\log(L_R) = (0.79 \pm 0.12)\ \log(L_X) + 4.38$. We note that the slope of this correlation is consistent at the 1σ level with the classical fundamental plane value (Merloni, Heinz & di Matteo 2003) and with values typically found for samples of low luminosity AGN ($\sim 0.5 - 0.7$; Dong et al., 2021). This slope is commonly interpreted as signature of a radiatively inefficient accretion process. Indeed we note that the slope of our relation is strongly constrained by the X-ray faint ETG, which are most likely inefficient accretors. On the other hand, we note that X-ray luminous ($\log(L_X) \gtrsim 43.5$) AGN tend to lie above the relation defined above (Eq. 5.16), and their distribution is scattered around the steeper Panessa et al. (2015) relation (slope $\sim$1.1), found for nearby Seyfert galaxies. This suggests that in these objects an efficient accretion flow may feed the central SMBH. We point out that our sources span a much wider redshift range than Panessa et al. (2015) sample, suggesting that local Seyfert galaxies and $z \geq 1$ radio-quiet NL- and BL-AGN may have similar radio/X-ray properties.
As for the star-forming ELG, we do not find a significant radio-X-ray correlation, suggesting that the radio and X-ray emissions of these objects are likely owed to different mechanisms, i.e. star-formation and nuclear activity, respectively. As for the sources without spectroscopic classification (i.e., those with photometric redshift), we found that they are likely composed by a mixture of AGN and SFG. Finally, we found that most ($\sim$80%) of the radio-detected sources having radio emission driven by nuclear activity show a radio-to-X-ray radio-loudness $R_X \lesssim -3.5$, which classifies these objects as RQ AGN (Terashima & Wilson, 2003; Lambrides et al., 2020). The results presented in this Chapter will be published in D'Amato et al. (subm.).

6.2 Future perspectives of deep radio surveys

6.2.1 Obscured AGN at the cosmic dawn

The vast majority of accreting SMBHs in the Universe are hidden by large amounts of dust and gas, and the fraction of obscured AGN increases towards high redshifts (e.g, Vito et al. 2018; see § 1.2.3). Despite most of the accretion onto SMBHs in the Universe is obscured, and even more so at early times, no reliable example of obscured AGN has been yet detected in the first billion year of the Universe, i.e. at $z \gtrsim 6$. X-ray surveys are indeed limited by their area-sensitivity combination and can currently probe sizeable samples of obscured AGN only up to $z \sim 4 - 5$. All of our knowledge about the most distant SMBHs comes from shallow, wide area optical/NIR surveys (e.g., Bañados et al., 2016), which select, by definition, only the unobscured AGN population. A promising way to select distant obscured AGN is through radio emission which, differently from the X-rays, is largely unaffected by obscuration. Next-generation wide-area radio surveys reaching μJy depth will be able to detect sizeable samples of faint, non-jetted AGN at $z \gtrsim 6$, besides the brighter but minor population of jetted systems. In addition, the radio-to-X-ray flux ratio can be used as a proxy for the AGN obscuration degree (e.g., Lambrides et al., 2020). Thus, observations at radio-wavelengths can unveil the presence of elusive, obscured AGN up to the cosmic dawn and in distant proto-clusters, such as the one presented in this work.

6.2.2 Deep radio surveys as probes of the distant proto-cluster population

Proto-clusters are ideal laboratories to constrain galaxy evolution models and cosmological parameters. Unfortunately, the conventional methods used to identify local clusters are impractical for identifying high redshift structures. Usually, distant clusters are selected by searching for concentrations of red galaxies in optical/IR images, or looking for extended X-ray emission associated with the hot ICM ($10^8 - 10^9$ K), filling the space within the structure members (Gladders & Yee, 2000, 2005; Stanford et al., 2012; Gilbank et al., 2011). However, these methods are currently limited to z$\sim$1.5 due to limited sensitivity of the available observatories (Rosati, Borgani & Norman, 2002; Mullis et al., 2005; Stanford et al., 2006; Muzzin et al., 2013). Proto-clusters can also be identified through the so-called Sunyaev–Zeldovich (SZ) effect[1] (e.g., Carlstrom, Holder & Reese, 2002). However, the detection rate of very high-redshift clusters using blind SZ effect is still lower than those relying on more traditional methods (Venemans et al., 2007; Overzier, 2016). Another cluster-finding approach is based on the search of galaxy overdensities in the line-of-sight velocity space (Eisenhardt et al., 2008; van Breukelen & Clewley, 2009; Castignani et al., 2014; Chiang, Overzier & Gebhardt, 2014). However, this method requires the determination of spectroscopic (or at least accurate photometric) redshifts for

[1]The SZ effect is produced by an interaction between the hot plasma in a galaxy cluster and the photons from the CMB. Basically, the high-energy electrons from the ionized gas scatter the CMB photons and give them a slight energy boost. As a result, there is a measurable difference between these boosted photons and the original photons from the CMB.

large samples of galaxies, implying the need for extensive spectroscopy or dense multi-band observations.

A promising approach to identify proto-cluster candidates consists in searching for biased tracer, i.e. source types that are known to be signpost of proto-clusters. HzRG are considered one of the best tracers, since there is strong evidence that they are progenitors of the very massive BCGs that populate the center of local clusters (e.g. Venemans et al., 2007; Chiaberge et al., 2010). Thus, coupling deep radio observations with multi-band ancillary data (aimed, for example, at detecting LAEs and LBGs) can significantly speed-up the search for early structures, from cosmic noon to cosmic dawn. In this Thesis work we detected in the radio-band the central QSO of the first confirmed overdensity at $z > 6$, mainly composed by LAEs and LBGs, and tentatively detected the first $z \sim 6$ obscured QSO, possibly member of such an overdensity. In addition, we detected three objects (including the proto-BCG) in a proto-cluster at $z \sim 1.7$. These findings highlight the potential of next-generation radio surveys in detecting and studying LSSs at high redshift ($z \sim 2 - 6$).

As a final remark, we note that Daddi et al. (2017) exploited the deep VLA observations at 3 GHz of the VLA-Cosmic Evolution Survey (COSMOS) field to demonstrate that distant proto-clusters can be efficiently selected just on the basis of radio-source clustering: they found that one of the most distant X-ray-detected clusters (Cl J1001 at $z = 2.5$, Wang et al., 2016) hosts a strong overdensity of radio sources. Considering that ongoing and planned radio surveys with SKA Observatory precursors and pathfinders will cover large areas of the sky with unprecedented depth, radio-based proto-cluster selection techniques will potentially allow to find hundreds of high-redshift systems Overzier et al. (2006); Chiang, Overzier & Gebhardt (2013), that can be exploited to constrain cosmological parameters and test galaxy evolution paradigms.

Bibliography

Abell G. O., 1958, ApJS, 3, 211

Abell G. O., 1965, ARA&A, 3, 1

Alexander D. M., Hickox R. C., 2012, New Astronomy Reviews, 56, 93

Álvarez-Márquez J. et al., 2016, A&A, 587, A122

Annunziatella M. et al., 2018, PASP, 130, 124501

Antonucci R., 1993, ARA&A, 31, 473

Bañados E. et al., 2016, ApJS, 227, 11

Bañados E. et al., 2015, ApJ, 804, 118

Baldwin J. A., Phillips M. M., Terlevich R., 1981, PASP, 93, 5

Balmaverde B. et al., 2017, A&A, 606, A23

Baloković M., Smolčić V., Ivezić Ž., Zamorani G., Schinnerer E., Kelly B. C., 2012, ApJ, 759, 30

Bañados E., Carilli C., Walter F., Momjian E., Decarli R., Farina E. P., Mazzucchelli C., Venemans B. P., 2018, The Astrophysical Journal, 861, L14

Becker R. H. et al., 2001, AJ, 122, 2850

Becker R. H., White R. L., Helfand D. J., 1995, ApJ, 450, 559

Beckmann V., Shrader C. R., 2012, Active Galactic Nuclei

Beers T. C., Flynn K., Gebhardt K., 1990, AJ, 100, 32

Behroozi P. S., Wechsler R. H., Conroy C., 2013, ApJ, 770, 57

Beifiori A., Courteau S., Corsini E. M., Zhu Y., 2012, MNRAS, 419, 2497

Belsole E., Worrall D. M., Hardcastle M. J., Birkinshaw M., Lawrence C. R., 2004, MNRAS, 352, 924

Best P. N., Kauffmann G., Heckman T. M., Brinchmann J., Charlot S., Ivezić Ž., White S. D. M., 2005, MNRAS, 362, 25

Bianchi S., Maiolino R., Risaliti G., 2012, Advances in Astronomy, 2012, 782030

Bicknell G. V., Sutherland R. S., van Breugel W. J. M., Dopita M. A., Dey A., Miley G. K., 2000, ApJ, 540, 678

Biggs A. D., Ivison R. J., 2006, MNRAS, 371, 963

Bîrzan L., Rafferty D. A., McNamara B. R., Wise M. W., Nulsen P. E. J., 2004, ApJ, 607, 800

Blain A. W., Smail I., Ivison R. J., Kneib J.-P., Frayer D. T., 2002, Physics Reports, 369, 111

Blanc G. A. et al., 2008, ApJ, 681, 1099

Blandford R. D., Znajek R. L., 1977, MNRAS, 179, 433

Bock D. C. J., Large M. I., Sadler E. M., 1999, AJ, 117, 1578

Boehringer H., Voges W., Fabian A. C., Edge A. C., Neumann D. M., 1993, MNRAS, 264, L25

Bolatto A. D., Wolfire M., Leroy A. K., 2013, ARA&A, 51, 207

Bolzonella M., Miralles J. M., Pelló R., 2000, A&A, 363, 476

Bonaldi A., Bonato M., Galluzzi V., Harrison I., Massardi M., Kay S., De Zotti G., Brown M. L., 2019, MNRAS, 482, 2

Bonchi A., La Franca F., Melini G., Bongiorno A., Fiore F., 2013, MNRAS, 429, 1970

Bondi M., Ciliegi P., Schinnerer E., Smolčić V., Jahnke K., Carilli C., Zamorani G., 2008, ApJ, 681, 1129

Bondi M. et al., 2003, A&A, 403, 857

Bonzini M. et al., 2015, MNRAS, 453, 1079

Bonzini M., Padovani P., Mainieri V., Kellermann K. I., Miller N., Rosati P., Tozzi P., Vattakunnel S., 2013, MNRAS, 436, 3759

Bourne M. A., Sijacki D., Puchwein E., 2019, MNRAS, 490, 343

Bower R. G. et al., 2004, MNRAS, 351, 63

Boylan-Kolchin M., Springel V., White S. D. M., Jenkins A., Lemson G., 2009, MNRAS, 398, 1150

Bridle A. H., Hough D. H., Lonsdale C. J., Burns J. O., Laing R. A., 1994, AJ, 108, 766

Bridle A. H., Schwab F. R., 1999, in Astronomical Society of the Pacific Conference Series, Vol. 180, Synthesis Imaging in Radio Astronomy II, Taylor G. B., Carilli C. L., Perley R. A., eds., p. 371

Brienza M. et al., 2021, Nature Astronomy

Brinkmann W., Laurent-Muehleisen S. A., Voges W., Siebert J., Becker R. H., Brotherton M. S., White R. L., Gregg M. D., 2000, A&A, 356, 445

Brodie J. P., Bowyer S., McCarthy P., 1985, ApJ, 293, L59

Brunetti G., Jones T. W., 2014, International Journal of Modern Physics D, 23, 1430007

Brusa M. et al., 2018, A&A, 612, A29

Buckley J., James I., 1979, Biometrika, 66, 429

Burlon D., Ajello M., Greiner J., Comastri A., Merloni A., Gehrels N., 2011, ApJ, 728, 58

Burtscher L. et al., 2013, A&A, 558, A149

Calura F., Gilli R., Vignali C., Pozzi F., Pipino A., Matteucci F., 2014, MNRAS, 438, 2765

Canosa C. M., Worrall D. M., Hardcastle M. J., Birkinshaw M., 1999, MNRAS, 310, 30

Capetti A. et al., 2021, arXiv e-prints, arXiv:2111.01615

Carilli C. L., Harris D. E., Pentericci L., Röttgering H. J. A., Miley G. K., Kurk J. D., van Breugel W., 2002, ApJ, 567, 781

Carilli C. L., Perley R. A., Harris D. E., 1994, MNRAS, 270, 173

Carilli C. L., Röttgering H. J. A., van Ojik R., Miley G. K., van Breugel W. J. M., 1997, ApJS, 109, 1

Carilli C. L., Walter F., 2013, ARA&A, 51, 105

Carlstrom J. E., Holder G. P., Reese E. D., 2002, ARA&A, 40, 643

Carniani S. et al., 2019, MNRAS, 489, 3939

Casasola V., Magrini L., Combes F., Mignano A., Sani E., Paladino R., Fontani F., 2013, A&A, 558, A60

Casey C. M., 2016, ApJ, 824, 36

Castignani G., Chiaberge M., Celotti A., Norman C., 2014, ApJ, 792, 113

Castignani G., Combes F., Salomé P., 2020, A&A, 635, L10

Chiaberge M., Capetti A., Celotti A., 2000, A&A, 355, 873

Chiaberge M., Capetti A., Macchetto F. D., Rosati P., Tozzi P., Tremblay G. R., 2010, ApJ, 710, L107

Chiaberge M., Macchetto F. D., Sparks W. B., Capetti A., Allen M. G., Martel A. R., 2002, ApJ, 571, 247

Chiang Y.-K., Overzier R., Gebhardt K., 2013, ApJ, 779, 127

Chiang Y.-K., Overzier R., Gebhardt K., 2014, ApJ, 782, L3

Ciesla L. et al., 2015, A&A, 576, A10

Ciliegi P. et al., 1999, MNRAS, 302, 222

Circosta C. et al., 2019, A&A, 623, A172

Cohen M. H., Lister M. L., Homan D. C., Kadler M., Kellermann K. I., Kovalev Y. Y., Vermeulen R. C., 2007, ApJ, 658, 232

Combes F., 2017, Frontiers in Astronomy and Space Sciences, 4, 10

Condon J. J., 1992, ARA&A, 30, 575

Condon J. J., 1997, PASP, 109, 166

Condon J. J. et al., 2012, ApJ, 758, 23

Condon J. J., Cotton W. D., Greisen E. W., Yin Q. F., Perley R. A., Taylor G. B., Broderick J. J., 1998, AJ, 115, 1693

Condon J. J., Cotton W. D., Yin Q. F., Shupe D. L., Storrie-Lombardi L. J., Helou G., Soifer B. T., Werner M. W., 2003, AJ, 125, 2411

Conley A. et al., 2011, ApJl, 732, L35

Coriat M. et al., 2011, MNRAS, 414, 677

Cresci G. et al., 2015, A&A, 582, A63

Croft S. et al., 2006, ApJ, 647, 1040

Croston J. H., Hardcastle M. J., Harris D. E., Belsole E., Birkinshaw M., Worrall D. M., 2005, ApJ, 626, 733

Cucciati O. et al., 2018, A&A, 619, A49

Cucciati O. et al., 2014, A&A, 570, A16

Daddi E. et al., 2015, A&A, 577, A46

Daddi E. et al., 2009, ApJ, 694, 1517

Daddi E. et al., 2017, ApJ, 846, L31

D'Amato Q. et al., 2020a, A&A, 641, L6

D'Amato Q. et al., 2020b, A&A, 636, A37

D'Amato Q. et al., 2021, arXiv e-prints, arXiv:2112.03658

D'Amato et al., subm., A&A, http://j1030-field.oas.inaf.it/QD_JVLA.pdf

Dannerbauer H., Daddi E., Riechers D. A., Walter F., Carilli C. L., Dickinson M., Elbaz D., Morrison G. E., 2009, ApJ, 698, L178

Dannerbauer H. et al., 2014, A&A, 570, A55

De Breuck C., Röttgering H., Miley G., van Breugel W., Best P., 2000, A&A, 362, 519

De Lucia G., Blaizot J., 2007, MNRAS, 375, 2

de Ruiter H. R., Parma P., Fanti C., Fanti R., 1990, A&A, 227, 351

de Vries W. H., Morganti R., Röttgering H. J. A., Vermeulen R., van Breugel W., Rengelink R., Jarvis M. J., 2002, AJ, 123, 1784

Debye P., 1909, Annalen der Physik, 335, 57

Decarli R. et al., 2019, ApJ, 882, 138

Decarli R. et al., 2018, ApJ, 854, 97

Delvecchio I. et al., 2021, A&A, 647, A123

Delvecchio I. et al., 2017, A&A, 602, A3

Dey A., van Breugel W., Vacca W. D., Antonucci R., 1997, ApJ, 490, 698

Di Matteo T., Quataert E., Allen S. W., Narayan R., Fabian A. C., 2000, MNRAS, 311, 507

Díaz C. G., Koyama Y., Ryan-Weber E. V., Cooke J., Ouchi M., Shimasaku K., Nakata F., 2014, MNRAS, 442, 946

Dong A.-J., Ge K., Liu X., Zhi Q.-J., 2021, Astronomische Nachrichten, 342, 191

Dong A.-J., Wu Q., Cao X.-F., 2014, ApJ, 787, L20

Draine B. T., Li A., 2007, ApJ, 657, 810

Draine B. T., Li A., Hensley B. S., Hunt L. K., Sandstrom K., Smith J. D. T., 2021, ApJ, 917, 3

Drouart G. et al., 2014, A&A, 566, A53

Duncan K. J. et al., 2018a, MNRAS, 473, 2655

Duncan K. J., Jarvis M. J., Brown M. J. I., Röttgering H. J. A., 2018b, MNRAS, 477, 5177

Dunlop J. S., Peacock J. A., 1990, MNRAS, 247, 19

Duras F. et al., 2020, A&A, 636, A73

Eddington A. S., 1913, MNRAS, 73, 359

Eisenhardt P. R. M. et al., 2008, ApJ, 684, 905

Eke V. R., Navarro J. F., Frenk C. S., 1998, ApJ, 503, 569

Elmegreen B. G., Elmegreen D. M., 2006, ApJ, 650, 644

Emonts B. H. C. et al., 2018, MNRAS, 477, L60

Emonts B. H. C. et al., 2016, Science, 354, 1128

Emonts B. H. C. et al., 2014, MNRAS, 438, 2898

Erlund M. C., Fabian A. C., Blundell K. M., Celotti A., Crawford C. S., 2006, MNRAS, 371, 29

Event Horizon Telescope Collaboration et al., 2019, ApJ, 875, L1

Fabian A. C., 2012, ARA&A, 50, 455

Fabian A. C., Celotti A., Johnstone R. M., 2003, MNRAS, 338, L7

Fabian A. C., Lohfink A., Kara E., Parker M. L., Vasudevan R., Reynolds C. S., 2015, MNRAS, 451, 4375

Falcke H., Körding E., Markoff S., 2004, A&A, 414, 895

Fan X. et al., 2001, AJ, 122, 2833

Fanaroff B. L., Riley J. M., 1974, MNRAS, 167, 31P

Farrah D., Priddey R., Wilman R., Haehnelt M., McMahon R., 2004, ApJ, 611, L13

Feigelson E. D., Nelson P. I., 1985, ApJ, 293, 192

Feltre A., Hatziminaoglou E., Fritz J., Franceschini A., 2012, MNRAS, 426, 120

Fomalont E. B., Kellermann K. I., Cowie L. L., Capak P., Barger A. J., Partridge R. B., Windhorst R. A., Richards E. A., 2006, ApJS, 167, 103

Foreman-Mackey D., Hogg D. W., Lang D., Goodman J., 2013, PASP, 125, 306

Fragile P. C., Anninos P., Croft S., Lacy M., Witry J. W. L., 2017, ApJ, 850, 171

Fritz J., Franceschini A., Hatziminaoglou E., 2006, MNRAS, 366, 767

Fu H. et al., 2012, ApJ, 753, 134

Gallagher S. C., Abado M. M., Everett J. E., Keating S., Deo R. P., 2013, ArXiv e-prints

Galluzzi V. et al., 2017, MNRAS, 465, 4085

Garrington S. T., Conway R. G., 1991, MNRAS, 250, 198

Genzel R. et al., 2015, ApJ, 800, 20

George S. J., Stil J. M., Keller B. W., 2012, Publ. Astron. Soc. Australia, 29, 214

Ghisellini G., Tavecchio F., Maraschi L., Celotti A., Sbarrato T., 2014, Nature, 515, 376

Gilbank D. G., Gladders M. D., Yee H. K. C., Hsieh B. C., 2011, AJ, 141, 94

Gilli R., Calura F., D'Ercole A., Norman C., 2017, A&A, 603, A69

Gilli R., Comastri A., Hasinger G., 2007, A&A, 463, 79

Gilli R. et al., 2019, A&A, 632, A26

Gilli R. et al., 2014, A&A, 562, A67

Ginolfi M. et al., 2017, MNRAS, 468, 3468

Giommi P., Padovani P., Polenta G., 2013, MNRAS, 431, 1914

Giovannini G., Cotton W. D., Feretti L., Lara L., Venturi T., 1998, ApJ, 493, 632

Giovannini G., Cotton W. D., Feretti L., Lara L., Venturi T., 2001, ApJ, 552, 508

Gladders M. D., Yee H. K. C., 2000, AJ, 120, 2148

Gladders M. D., Yee H. K. C., 2005, ApJS, 157, 1

Graham J. A., 1998, ApJ, 502, 245

Gruppioni C. et al., 1999, MNRAS, 305, 297

Gruppioni C., Pozzi F., Zamorani G., Vignali C., 2011, MNRAS, 416, 70

Gruppioni C., Zamorani G., de Ruiter H. R., Parma P., Mignoli M., Lari C., 1997, MNRAS, 286, 470

Gunn J. E., Peterson B. A., 1965, ApJ, 142, 1633

Haas M., 2003, in ESA Special Publication, Vol. 511, Exploiting the ISO Data Archive. Infrared Astronomy in the Internet Age, Gry C., Peschke S., Matagne J., Garcia-Lario P., Lorente R., Salama A., eds., p. 257

Hales C. A., Norris R. P., Gaensler B. M., Middelberg E., 2014a, MNRAS, 440, 3113

Hales C. A. et al., 2014b, MNRAS, 441, 2555

Hardcastle M. J., Evans D. A., Croston J. H., 2007, MNRAS, 376, 1849

Harrington K. C. et al., 2021, ApJ, 908, 95

Harris D. E., Grindlay J. E., 1979, MNRAS, 188, 25

Harrison C., 2014, PhD thesis, Durham University

Harrison C. M., 2017, Nature Astronomy, 1, 0165

Harwood J. J. et al., 2017, MNRAS, 469, 639

Hatch N. A., Overzier R. A., Kurk J. D., Miley G. K., Röttgering H. J. A., Zirm A. W., 2009, MNRAS, 395, 114

Hatch N. A., Overzier R. A., Röttgering H. J. A., Kurk J. D., Miley G. K., 2008, MNRAS, 383, 931

Heckman T. M., Best P. N., 2014, ARA&A, 52, 589

Heinz S., Sunyaev R. A., 2003, MNRAS, 343, L59

Herrera Ruiz N. et al., 2017, A&A, 607, A132

Herrera Ruiz N., Middelberg E., Norris R. P., Maini A., 2016, A&A, 589, L2

Heywood I. et al., 2016, MNRAS, 460, 4433

Heywood I. et al., 2021, ApJ, 910, 105

Hodge J. A., Becker R. H., White R. L., Richards G. T., Zeimann G. R., 2011, AJ, 142, 3

Hopkins A. M., Afonso J., Chan B., Cram L. E., Georgakakis A., Mobasher B., 2003, AJ, 125, 465

Hopkins A. M., Mobasher B., Cram L., Rowan-Robinson M., 1998, MNRAS, 296, 839

Huynh M. T., Jackson C. A., Norris R. P., Prandoni I., 2005, AJ, 130, 1373

Ibar E., Ivison R. J., Biggs A. D., Lal D. V., Best P. N., Green D. A., 2009, MNRAS, 397, 281

Ichimaru S., 1977, Apj), 214, 840

Ineson J., Croston J. H., Hardcastle M. J., Mingo B., 2017, MNRAS, 467, 1586

Isobe N., Seta H., Tashiro M. S., 2011, PASJ, 63, S947

Isobe T., Feigelson E. D., Nelson P. I., 1986, ApJ, 306, 490

Ivison R. J. et al., 2007, ApJ, 660, L77

Jaffe D. T., Marsh J. P., Tokunaga A., 2004, in Bulletin of the American Astronomical Society, Vol. 36, American Astronomical Society Meeting Abstracts, p. 1568

Jiang L., Fan X., Ivezić Ž., Richards G. T., Schneider D. P., Strauss M. A., Kelly B. C., 2007, ApJ, 656, 680

Johnson O., Almaini O., Best P. N., Dunlop J., 2007, MNRAS, 376, 151

Kaasinen M. et al., 2019, ApJ, 880, 15

Kaiser C. R., Schoenmakers A. P., Röttgering H. J. A., 2000, MNRAS, 315, 381

Kalfountzou E. et al., 2017, MNRAS, 471, 28

Kamenetzky J., Rangwala N., Glenn J., Maloney P. R., Conley A., 2016, ApJ, 829, 93

Kataoka J., Stawarz Ł., 2005, ApJ, 622, 797

Kellermann K. I., Sramek R., Schmidt M., Shaffer D. B., Green R., 1989, AJ, 98, 1195

Kennicutt, Robert C. J., 1998, ApJ, 498, 541

Kim S. et al., 2009, ApJ, 695, 809

King A., 2003, ApJ, 596, L27

King A., 2005, ApJ, 635, L121

Kirkpatrick A., Sharon C., Keller E., Pope A., 2019, ApJ, 879, 41

Kollgaard R. I., Brinkmann W., Chester M. M., Feigelson E. D., Hertz P., Reich P., Wielebinski R., 1994, ApJS, 93, 145

Kormendy J., Ho L. C., 2013, ARA&A, 51, 511

Kurk J. D., Pentericci L., Röttgering H. J. A., Miley G. K., 2004, A&A, 428, 793

La Franca F., Melini G., Fiore F., 2010, ApJ, 718, 368

Lacy M., Baum S. A., Chandler C. J., Chatterjee S., Murphy E. J., Myers S. T., VLASS Survey Science Group, 2016, in American Astronomical Society Meeting Abstracts, Vol. 227, American Astronomical Society Meeting Abstracts #227, p. 324.09

Lacy M., Croft S., Fragile C., Wood S., Nyland K., 2017, ApJ, 838, 146

Lacy M., Rawlings S., Blundell K. M., Ridgway S. E., 1998, MNRAS, 298, 966

Lahav O., Lilje P. B., Primack J. R., Rees M. J., 1991, MNRAS, 251, 128

Laing R. A., 1980, MNRAS, 193, 439

Laing R. A., 1988, Nature, 331, 149

Lambrides E. L., Chiaberge M., Heckman T., Gilli R., Vito F., Norman C., 2020, ApJ, 897, 160

Lapi A. et al., 2018, ApJ, 857, 22

Lavalley M., Isobe T., Feigelson E., 1992, in Astronomical Society of the Pacific Conference Series, Vol. 25, Astronomical Data Analysis Software and Systems I, Worrall D. M., Biemesderfer C., Barnes J., eds., p. 245

Leipski C. et al., 2014, ApJ, 785, 154

Lemaux B. C. et al., 2012, ApJ, 745, 106

Lidman C. et al., 2012, MNRAS, 427, 550

Lin L. et al., 2012, ApJ, 756, 71

Liu Y. et al., 2021, ApJ, 908, 124

Lusso E. et al., 2012, MNRAS, 425, 623

Lynden-Bell D., 1996, MNRAS, 279, 389

Macconi D., Torresi E., Grandi P., Boccardi B., Vignali C., 2020, MNRAS, 493, 4355

Madau P., Dickinson M., 2014, ARA&A, 52, 415

Magdis G. E. et al., 2012, ApJ, 760, 6

Magorrian J. et al., 1998, AJ, 115, 2285

Maini A., Prandoni I., Norris R. P., Giovannini G., Spitler L. R., 2016, A&A, 589, L3

Mancuso C. et al., 2017, ApJ, 842, 95

Mandal S. et al., 2021, A&A, 648, A5

Marchesi S. et al., 2021, accepted for publication on A&A, arXiv:2109.08162

Marconi A., Risaliti G., Gilli R., Hunt L. K., Maiolino R., Salvati M., 2004, MNRAS, 351, 169

Mathis J. S., Rumpl W., Nordsieck K. H., 1977, ApJ, 217, 425

Matthews A. M., Condon J. J., Cotton W. D., Mauch T., 2021, ApJ, 909, 193

McCarthy P. J., 1993, ARA&A, 31, 639

McConnell D. et al., 2020, Publ. Astron. Soc. Australia, 37, e048

McDonald M. et al., 2016, ApJ, 817, 86

McMullin J. P., Waters B., Schiebel D., Young W., Golap K., 2007, in Astronomical Society of the Pacific Conference Series, Vol. 376, Astronomical Data Analysis Software and Systems XVI, Shaw R. A., Hill F., Bell D. J., eds., p. 127

McNamara B. R., Nulsen P. E. J., 2007, ARA&A, 45, 117

McNamara B. R. et al., 2000, ApJ, 534, L135

Meijerink R., Spaans M., 2005, A&A, 436, 397

Meijerink R., Spaans M., Israel F. P., 2007, A&A, 461, 793

Merloni A., Heinz S., di Matteo T., 2003, MNRAS, 345, 1057

Mie G., 1908, Annalen der Physik, 330, 377

Migliori G., Grandi P., Palumbo G. G. C., Brunetti G., Stanghellini C., 2007, ApJ, 668, 203

Mignano A., Prandoni I., Gregorini L., Parma P., de Ruiter H. R., Wieringa M. H., Vettolani G., Ekers R. D., 2008, A&A, 477, 459

Mignoli M. et al., 2020, A&A, 642, L1

Miley G., 1980, ARA&A, 18, 165

Miley G., De Breuck C., 2008, A&ARv, 15, 67

Miley G. K. et al., 2006, ApJ, 650, L29

Miller N. A. et al., 2013, ApJS, 205, 13

Mineo S., Gilfanov M., Lehmer B. D., Morrison G. E., Sunyaev R., 2014, MNRAS, 437, 1698

Mingo B. et al., 2019, MNRAS, 488, 2701

Mingozzi M. et al., 2018, MNRAS, 474, 3640

Mohan N., Rafferty D., 2015, PyBDSF: Python Blob Detection and Source Finder

Morganti R., Garrett M. A., Chapman S., Baan W., Helou G., Soifer T., 2004, A&A, 424, 371

Morrison G. E., Owen F. N., Dickinson M., Ivison R. J., Ibar E., 2010, ApJS, 188, 178

Morselli L. et al., 2014, A&A, 568, A1

Mould J. R. et al., 2000, ApJ, 536, 266

Muldrew S. I., Hatch N. A., Cooke E. A., 2015, MNRAS, 452, 2528

Mullis C. R., Rosati P., Lamer G., Böhringer H., Schwope A., Schuecker P., Fassbender R., 2005, ApJ, 623, L85

Murray N., Quataert E., Thompson T. A., 2005, ApJ, 618, 569

Muxlow T. W. B., Garrington S. T., 1991, Observations of large scale extragalactic jets, Vol. 19, p. 52

Muxlow T. W. B. et al., 2020, MNRAS, 495, 1188

Muzzin A., Wilson G., Demarco R., Lidman C., Nantais J., Hoekstra H., Yee H. K. C., Rettura A., 2013, ApJ, 767, 39

Nanni R. et al., 2018, A&A, 614, A121

Nanni R. et al., 2020, A&A, 637, A52

Narayan R., Yi I., 1994, ApJ, 428, L13

Nesvadba N. P. H., Lehnert M. D., Eisenhauer F., Gilbert A., Tecza M., Abuter R., 2006, ApJ, 650, 693

Netzer H., 2013, The Physics and Evolution of Active Galactic Nuclei

Noble A. G. et al., 2017, ApJ, 842, L21

Noll S., Burgarella D., Giovannoli E., Buat V., Marcillac D., Muñoz-Mateos J. C., 2009, A&A, 507, 1793

Norris R. P. et al., 2006, AJ, 132, 2409

Norris R. P. et al., 2021, arXiv e-prints, arXiv:2108.00569

Novak M. et al., 2017, A&A, 602, A5

Ocran E. F., Taylor A. R., Vaccari M., Green D. A., 2017, MNRAS, 468, 1156

Ocran E. F., Taylor A. R., Vaccari M., Ishwara-Chandra C. H., Prandoni I., 2020, MNRAS, 491, 1127

O'Dea C. P., Saikia D. J., 2021, A&ARv, 29, 3

Ohsuga K., Mineshige S., 2011, ApJ, 736, 2

Osterbrock D. E., Ferland G. J., 2006, Astrophysics of gaseous nebulae and active galactic nuclei

Overzier R. A., 2016, A&ARv, 24, 14

Overzier R. A. et al., 2006, ApJ, 637, 58

Overzier R. A., Nesvadba N. P. H., Dijkstra M., Hatch N. A., Lehnert M. D., Villar-Martín

M., Wilman R. J., Zirm A. W., 2013, ApJ, 771, 89

Owen F. N., Dwarakanath K. S., Smith C. C., Ledlow M. J., Keel W. C., Morrison G. E., Voges W., Burns J. O., 1996, in Astronomical Society of the Pacific Conference Series, Vol. 100, Energy Transport in Radio Galaxies and Quasars, Hardee P. E., Bridle A. H., Zensus J. A., eds., p. 353

Owen F. N., Morrison G. E., 2008, AJ, 136, 1889

Oyabu S. et al., 2005, AJ, 130, 2019

Pacholczyk A. G., 1970, Radio astrophysics. Nonthermal processes in galactic and extragalactic sources

Padovani P., 2011, MNRAS, 411, 1547

Padovani P., 2016, A&ARv, 24, 13

Padovani P., 2017, Nature Astronomy, 1, 0194

Padovani P. et al., 2017, A&AR, 25, 2

Padovani P., Bonzini M., Kellermann K. I., Miller N., Mainieri V., Tozzi P., 2015, MNRAS, 452, 1263

Panessa F., Barcons X., Bassani L., Cappi M., Carrera F. J., Ho L. C., Pellegrini S., 2007, A&A, 467, 519

Panessa F. et al., 2015, MNRAS, 447, 1289

Papadopoulos P. P., Feain I. J., Wagg J., Wilner D. J., 2008, ApJ, 684, 845

Papadopoulos P. P., van der Werf P., Xilouris E., Isaak K. G., Gao Y., 2012, ApJ, 751, 10

Parma P., Morganti R., Capetti A., Fanti R., de Ruiter H. R., 1993, A&A, 267, 31

Peacock J. A., Miller L., Longair M. S., 1986, MNRAS, 218, 265

Peca A. et al., 2021, ApJ, 906, 90

Pentericci L. et al., 2002, AJ, 123, 2151

Pentericci L., Roettgering H. J. A., Miley G. K., Carilli C. L., McCarthy P., 1997, A&A, 326, 580

Pentericci L., Van Reeven W., Carilli C. L., Röttgering H. J. A., Miley G. K., 2000, A&AS, 145, 121

Perley R. A., Butler B. J., 2017, The Astrophysical Journal Supplement Series, 230, 7

Perley R. A., Willis A. G., Scott J. S., 1979, Nature, 281, 437

Perna M. et al., 2018, A&A, 619, A90

Peterson B. M., 1997, An Introduction to Active Galactic Nuclei

Petric A. O., Carilli C. L., Bertoldi F., Fan X., Cox P., Strauss M. A., Omont A., Schneider D. P., 2003, AJ, 126, 15

Petrucci P. O., Ursini F., De Rosa A., Bianchi S., Cappi M., Matt G., Dadina M., Malzac J., 2018, A&A, 611, A59

Piconcelli E., Jimenez-Bailón E., Guainazzi M., Schartel N., Rodríguez-Pascual P. M., Santos-Lleó M., 2005, A&A, 432, 15

Pier E. A., Krolik J. H., 1992, ApJ, 401, 99

Pier E. A., Krolik J. H., 1993, ApJ, 418, 673

Pillepich A. et al., 2018, MNRAS, 475, 648

Planck Collaboration et al., 2016, A&A, 594, A13

Plotkin R. M., Markoff S., Kelly B. C., Körding E., Anderson S. F., 2012, MNRAS, 419, 267

Pozzi F., Vallini L., Vignali C., Talia M., Gruppioni C., Mingozzi M., Massardi M., Andreani P., 2017, MNRAS, 470, L64

Prandoni I., 2018, in Peering towards Cosmic Dawn, Jelić V., van der Hulst T., eds., Vol. 333, pp. 175–182

Prandoni I., Gregorini L., Parma P., de Ruiter H. R., Vettolani G., Wieringa M. H., Ekers R. D., 2000, A&AS, 146, 41

Prandoni I., Gregorini L., Parma P., de Ruiter H. R., Vettolani G., Wieringa M. H., Ekers R. D., 2001a, A&A, 365, 392

Prandoni I., Gregorini L., Parma P., de Ruiter H. R., Vettolani G., Zanichelli A., Wieringa M. H., Ekers R. D., 2001b, A&A, 369, 787

Prandoni I., Guglielmino G., Morganti R., Vaccari M., Maini A., Röttgering H. J. A., Jarvis M. J., Garrett M. A., 2018, MNRAS, 481, 4548

Quadri R. et al., 2007, AJ, 134, 1103

Rangwala N. et al., 2011, ApJ, 743, 94

Rawle T. D. et al., 2012, ApJ, 747, 29

Rees M. J., 1989, MNRAS, 239, 1P

Rees M. J., Begelman M. C., Blandford R. D., Phinney E. S., 1982, Nature, 295, 17

Regener V. H., 1951, Physical Review, 84, 161

Rejkuba M., Minniti D., Courbin F., Silva D. R., 2002, ApJ, 564, 688

Retana-Montenegro E., Röttgering H. J. A., Shimwell T. W., van Weeren R. J., Prandoni I., Brunetti G., Best P. N., Brüggen M., 2018, A&A, 620, A74

Reuland M. et al., 2003, ApJ, 592, 755

Richards E. A., 2000, ApJ, 533, 611

Richards G. T. et al., 2006, ApJS, 166, 470

Riechers D. A. et al., 2013, Nature, 496, 329

Risaliti G., 2008, in American Institute of Physics Conference Series, Vol. 1053, American Institute of Physics Conference Series, Chakrabarti S. K., Majumdar A. S., eds., pp. 59–62

Risaliti G., Elvis M., 2004, in Astrophysics and Space Science Library, Vol. 308, Supermassive Black Holes in the Distant Universe, Barger A. J., ed., p. 187

Rosati P., 1998, in Wide Field Surveys in Cosmology, Colombi S., Mellier Y., Raban B., eds., Vol. 14, p. 219

Rosati P., Borgani S., Norman C., 2002, ARA&A, 40, 539

Rosenberg M. J. F. et al., 2015, ApJ, 801, 72

Ruffa I. et al., 2019, MNRAS, 484, 4239

Saikia D. J., Salter C. J., 1988, ARA&A, 26, 93

Salomé Q., Salomé P., Combes F., 2015, A&A, 574, A34

Salomé Q., Salomé P., Combes F., Hamer S., 2016, A& A, 595, A65

Saro A., Borgani S., Tornatore L., De Lucia G., Dolag K., Murante G., 2009, MNRAS, 392, 795

Sbarrato T., Ghisellini G., Giovannini G., Giroletti M., 2021, A&A, 655, A95

Scharf C., Smail I., Ivison R., Bower R., van Breugel W., Reuland M., 2003, ApJ, 596, 105

Schartmann M., Meisenheimer K., Klahr H., Camenzind M., Wolf S., Henning T., 2009, MNRAS, 393, 759

Schinnerer E. et al., 2007, ApJS, 172, 46

Schmidt M., 1970, ApJ, 162, 371

Schreiber C. et al., 2015, A&A, 575, A74

Scoville N. et al., 2014, ApJ, 783, 84

Scoville N. et al., 2016, Apj, 820, 83

Seyfert C. K., 1943, ApJ, 97, 28

Seymour N. et al., 2012, ApJ, 755, 146

Seymour N. et al., 2008, MNRAS, 386, 1695

Seymour N., McHardy I. M., Gunn K. F., 2004, MNRAS, 352, 131

Shakura N. I., Sunyaev R. A., 1973, A&A, 500, 33

Silk J., Rees M. J., 1998, A&A, 331, L1

Simpson C. et al., 2006, MNRAS, 372, 741

Simpson C., Rawlings S., 2002, MNRAS, 334, 511

Smolčić V. et al., 2017a, A&A, 602, A2

Smolčić V. et al., 2017b, A&A, 602, A1

Smolčić V. et al., 2008, ApJS, 177, 14

Solomon P. M., Downes D., Radford S. J. E., 1992, ApJ, 398, L29

Solomon P. M., Vanden Bout P. A., 2005, ARA&A, 43, 677

Spearman C., 1904, The American Journal of Psychology, 15, 72

Stalevski M., Fritz J., Baes M., Nakos T., Popović L. Č., 2012, MNRAS, 420, 2756

Stanford S. A. et al., 2012, ApJ, 753, 164

Stanford S. A. et al., 2006, ApJ, 646, L13

Stanley F. et al., 2017, MNRAS, 472, 2221

Steidel C. C., Adelberger K. L., Dickinson M., Giavalisco M., Pettini M., Kellogg M., 1998, ApJ, 492, 428

Steidel C. C., Giavalisco M., Pettini M., Dickinson M., Adelberger K. L., 1996, ApJ, 462, L17

Steinbring E., 2014, AJ, 148, 10

Stevens J. A. et al., 2003, Nature, 425, 264

Stiavelli M. et al., 2005, ApJ, 622, L1

Stockman H. S., Angel J. R. P., 1978, ApJ, 220, L67

Strazzullo V. et al., 2015, A&A, 576, L6

Tacconi L. J. et al., 2018, ApJ, 853, 179

Taylor A. R., Stil J. M., Sunstrum C., 2009, ApJ, 702, 1230

Terashima Y., Wilson A. S., 2003, ApJ, 583, 145

Trebitsch M., Volonteri M., Dubois Y., 2019, MNRAS, 487, 819

Turner R. J., Shabala S. S., Krause M. G. H., 2018, MNRAS, 474, 3361

Urry C. M., Padovani P., 1995, PASP, 107, 803

Valentino F. et al., 2021, A&A, 654, A165

Vallini L., Tielens A. G. G. M., Pallottini A., Gallerani S., Gruppioni C., Carniani S., Pozzi F., Talia M., 2019, MNRAS, 490, 4502

van Breugel W., Filippenko A. V., Heckman T., Miley G., 1985, ApJ, 293, 83

van Breugel W. J. M., Dey A., 1993, ApJ, 414, 563

van Breukelen C., Clewley L., 2009, MNRAS, 395, 1845

van der Werf P. P. et al., 2010, A&A, 518, L42

van Ojik R., Roettgering H. J. A., Carilli C. L., Miley G. K., Bremer M. N., Macchetto F., 1996, A&A, 313, 25

van Ojik R., Roettgering H. J. A., Miley G. K., Hunstead R. W., 1997, A&A, 317, 358

Veilleux S., Osterbrock D. E., 1987, ApJS, 63, 295

Venemans B. P. et al., 2007, A&A, 461, 823

Verdoes Kleijn G. A., de Zeeuw P. T., 2005, A&A, 435, 43

Villar-Martín M., Humphrey A., De Breuck C., Fosbury R., Binette L., Vernet J., 2007, MNRAS, 375, 1299

Vito F. et al., 2018, MNRAS, 473, 2378

Vito F. et al., 2016, MNRAS, 463, 348

Vito F., Gilli R., Vignali C., Comastri A., Brusa M., Cappelluti N., Iwasawa K., 2014, MNRAS, 445, 3557

Wagg J. et al., 2012, ApJ, 752, 91

Wainer H., Thyssen D., 1976, Psychometrika, 41, 9

Wang T. et al., 2016, ApJ, 828, 56

Wang Z., Wiita P. J., Hooda J. S., 2000, ApJ, 534, 201

Weaver R., McCray R., Castor J., Shapiro P., Moore R., 1977, ApJ, 218, 377

Webb T. M. A. et al., 2017, ApJ, 844, L17

Webb T. M. A. et al., 2015, ApJ, 814, 96

Weiß A., Walter F., Scoville N. Z., 2005, A&A, 438, 533

Weiß A., Downes D., Walter F., Henkel C., 2007, in Astronomical Society of the Pacific Conference Series, Vol. 375, From Z-Machines to ALMA: (Sub)Millimeter Spectroscopy of Galaxies, Baker A. J., Glenn J., Harris A. I., Mangum J. G., Yun M. S., eds., p. 25

White G. J. et al., 2012, MNRAS, 427, 1830

White G. J. et al., 2010, A&A, 517, A54

White R. L., Becker R. H., Helfand D. J., Gregg M. D., 1997, ApJ, 475, 479

Wiita P. J., Wang Z., Hooda J. S., 2002, New Astron. Rev., 46, 439

Willott C. J., Rawlings S., Blundell K. M., Lacy M., 1999, MNRAS, 309, 1017

Willott C. J., Rawlings S., Blundell K. M., Lacy M., Eales S. A., 2001, MNRAS, 322, 536

Wilman R. J., Jarvis M. J., Mauch T., Rawlings S., Hickey S., 2010, MNRAS, 405, 447

Wilman R. J. et al., 2008, MNRAS, 388, 1335

Windhorst R., Mathis D., Neuschaefer L., 1990, in Astronomical Society of the Pacific Conference Series, Vol. 10, Evolution of the Universe of Galaxies, Kron R. G., ed., pp. 389–403

Windhorst R. A., van Heerde G. M., Katgert P., 1984, A&AS, 58, 1

Zeballos M. et al., 2018, MNRAS, 479, 4577

Zhang Y. et al., 2016, ApJ, 816, 98

Zheng W. et al., 2006, ApJ, 640, 574

Zinn P. C., Middelberg E., Ibar E., 2011, A&A, 531, A14

Zovaro H. R. M. et al., 2020, MNRAS, 499, 4940

List of Figures

1.1 Schematic representation of the Unified Models paradigm, where the principal components of the AGN are indicated. The various types of AGN result from different orientation angles with respect to the line of sight. Image adapted from Beckmann & Shrader (2012). 4

1.2 *Top*: a schematic view of the spectral energy distribution of AGN, showing the emission of the various components as labeled. The black solid curve represents the total emission of "non-jetted" AGN, while the "jetted" emission is reported for the HSP and LSP Blazar sub-classes (see § 1.1.5). From Padovani et al. (2017), adapted from Harrison (2014). *Center:* X-rays spectrum of an AGN with labeled main components presented in the text (image taken from http://www.isdc.unige.ch/~ricci/Website/AGN_in_the_X-ray_band.html). *Bottom:* Examples of AGN mock SED in the IR band, for Type I, intermediate Type and Type II classes (left to right, blue points), and best fits obtained by Code Investigating GALaxy Emission (CIGALE Noll et al., 2009). The main components of the IR emission are also reported. Adapted from Ciesla et al. (2015). 6

1.3 *Top*: observed Radio/X-ray radio-loudness (R_X) distribution for a sample of X-ray-selected obscured AGN (violet histogram). The grey histogram represents upper limits. The black open histogram is the distribution for X-ray detected galaxies at $z > 0.5$, originally classified as normal galaxies. The vertical red dashed line marks the RQ/RL AGN threshold defined by Terashima & Wilson (2003), while the blue solid line shows the mean value for a sample of bright bona-fide RL sources. *Bottom*: same R_X distribution after correcting the X-ray luminosity for the obscuration, showing that a large fraction of the sample was misclassified as RL AGN and normal galaxies. From Lambrides et al. (2020). 10

1.4 Examples of a classical FRI (top image, Perley, Willis & Scott, 1979) and a classical FRII (bottom image, Bridle et al., 1994) radio-galaxy. 12

1.5 CO-SLED (also know as CO excitation ladder) for different classes of objects where the average CO(1→0) luminosities have been derived from available samples in the literature. The object classes are: Quasars (QSO), submillimeter galaxies (SMG), Lyman-break galaxies (LBG), color-selected galaxies (CSG), radio-galaxies (RG) (see Carilli & Walter 2013 for details). The CO-SLED of the Milky Way (MW) and M82 are also shown, along with the expected one for a constant brightness temperature object following the Rayleigh-Jeans law (valid for low-J, $S_\nu \propto \nu^2$). From Carilli & Walter (2013). 15

1.6 *Left*: fraction of obscured AGN with $\log N_H > 23$ vs. intrinsic X-ray luminosity as measured in the Chandra Deep Field North and South at z~4 (red and black points) and compared with other similar estimates at high-z (grey shaded areas, z ~3-5, see Vito et al. 2018 for further details) and in the local Universe (grey open circles, Burlon et al., 2011), showing an increasing of the obscured fraction with redshift. From Vito et al. (2018). *Right:* column density of the simulated galaxy gas distribution at the end of the cosmological hydro-dynamics simulation (z~5.7) performed by Trebitsch, Volonteri & Dubois (2019), showing that at high redshift the ISM can produce column densities up to $\log(N_H) \gtrsim 23$. . . . 18

1.7 X-ray derived column densities (x-axis) vs. ISM column densities derived from ALMA data using different methods (y-axis) for a sample of obscured AGN at z = 2.5 - 4.7 in the CDF-S (D'Amato et al., 2020b). The values related to the SMG CO–SLED, the QSO CO–SLED, and the continuum emission method are indicated by the red circles, blue circles, and green diamonds, respectively. We also report on the y-axis (black open squares) the column densities derived from the SED fitting by Circosta et al. (2019). The source IDs are reported in orange. The black dashed line represents the 1:1 relation. ISM densities can reach values as high as $\log N_H \sim 24$, which suggests that the increase in the AGN obscured fraction with redshift can be linked to off-nuclear absorption. 19

1.8 *Left*: evolution of the dark matter distribution for a massive cluster $M_{z=0} \sim 10^{15}\ M_\odot$ in the Millennium II simulation (adapted from Boylan-Kolchin et al., 2009). *Right*: Evolution of the baryonic matter for comparable scale and cluster mass of left panel, in which each dot is a galaxy with mass $\geq 10^8\ M_\odot$ (adapted from Muldrew, Hatch & Cooke, 2015). 22

1.9 *Left*: X-ray emission from the HzRG at the center of the Spiderweb protocluster at z=2.2 (black contours), superimposed on the radio image at 5 GHz, showing the alignment of the X-ray emission along the radio-jets (adapted from Carilli et al., 2002). *Right*: Ly-α emission (blue contours) superimposed on the HST ACS composite ($g_{475} + I_{814}$) image showing the huge amount of satellite galaxies surrounding the HzRG. The contours of the emission at 8 GHz are marked in red (from Miley et al., 2006). 25

2.1 *Left:* Combined optical/NIR spectrum of SDSS 1030+0524 (solid line). The main spectral features are labeled, while the powerlaw reproducing the continuum emission and parameterized as $f_\nu \propto \nu^{-0.5}$ is indicated by the dashed line. From Fan et al. (2001). *Right:* Long-time light-curve of the QSO, where the variation of the emission between the XMM-Newton observations in 2003 and the *Chandra* observations in 2017 is visible. From Nanni et al. (2018). 28

2.2 Broad-band multi-wavelength SED of SDSS J1030+0524. References to the points are labeled. The combined SED of luminous QSOs at lower redshift is marked by the green curve (Richards et al., 2006). The drop of the flux at $\lambda < 1$ is produced by the Ly-α forest. From Nanni et al. (2018). 29

2.3 *Left:* Smoothed 0.5–7 keV *Chandra* image of the J1030 field. Overlaid in colors are the regions covered by the available photometric surveys/catalogs. From Marchesi et al. (2021). *Right:* LBT/LBC z-band image of the J1030 field, showing the position of $z \sim 6$ LBG candidates (red dots). Spectroscopically confirmed members of the LSS at z=6.3 are marked in blue and labeled with their ID in the multi-band photometric catalogue. Two additional members of the LSS have been discovered in a MUSE field centered on the QSO (see brown square). The position of these two LAEs is indicated by the green circles. The inset shows a zoom of the sky region around the MUSE field. From Mignoli et al. (2020). . . 30

2.4 HST/ACS $F850LP$ image of the overdensity at $z = 1.7$. Overlaid in white are the VLA radio contours (based on Nanni et al. 2018 re-analysis of the Petric et al. 2003 observations). The main radio morphological features are labeled. Also shown is the *Chandra* smoothed point-source-subtracted image of diffuse X-ray emission (violet; 0.5–7 keV). North is up and east is to the left. The dark strip running across the bright star is the gap between the two ACS CCDs. The MUSE field of view is marked by the dashed white line. The position of the FRII host and its redshift are shown in yellow. Green circles mark MUSE galaxies in the overdensity with their redshifts labeled. An additional radio source may be part of the overdensity (labeled in white). The position of the $z = 6.3$ QSO at the center of the J1030 field is indicated in magenta. From G19. 33

2.5 *Left:* Point-source subtracted and smoothed Chandra X-ray composite image, showing the X-ray diffuse emission (down to $\sim 2.5\sigma$) around the FRII galaxy (white contours). The red (blue) channels show the soft (hard) emission. *Right:* specific star formation rate of MUSE galaxies $m1 - m6$ (green circles) plotted against the specific star formation rate vs. redshift relation derived for field galaxies with $\log(M_*/\mathrm{M}_\odot) = 9.5 - 10$ (from different samples as labeled). From G19. 36

3.1 *Left:* Composed r-g-b image of the field around the FRII radio-galaxy. Red, green and blue channels are the HST F160w, F850lp and F775w filters. Green and red circles mark the MUSE ($m1$-$m6$) and ALMA ($a0$-$a3$) sources, respectively. Source $a0$ (the FRII host) corresponds to the LUCI source $l1$, marked in yellow. A second LUCI source, $l2$, is located ~ 1.5 arcmin southeast from $a0$, outside the image. VLA contours at 1.4 GHz are overlaid in white, starting from a $\sim 3\sigma$ flux density threshold and increasing with a $\sqrt{3}$ geometric progression (Petric et al., 2003; Nanni et al., 2018). The orange contours marks the $\sim 2.5\sigma$ level of the diffuse X-ray emission (0.5-7 keV) discussed in G19. The green solid polygon delimits the region covered simultaneously by all HST filters. The solid magenta line and cyan box are the ALMA >50% response area and MUSE FoV, respectively. The white horizontal line at the bottom left indicates the angular and physical scale. *Right*: $\sim 7 \times 7$ arcsec^2 ($\sim 60 \times 60$ kpc^2) cut-outs of the composed HST r-g-b image, centered on the ALMA detected sources (named as labeled). The cyan contours represent the 3σ-moment 0 map of our observations (see Sect. 3.2.4), starting from a $\sim 3\sigma$ flux density threshold and increasing with a $\sqrt{3}$ geometric progression. The white ellipse in the bottom right corners represents the restoring beam. From D'Amato et al. (2020a). 44

3.2 ALMA spectra of the four detected sources (channel width of 30 km/s). For each spectrum, the top panel shows the data extracted from the datacubes (black solid line) as a function of the radial velocity offset (increasing with redshift) from the detected line center. The grey bars represent the relative error per channel measured on the noise-map. The solid magenta line marks the total model, i.e. the sum of the two components (red and blue dashed lines). The rest-frame zero-velocity is set to the central frequency of the fitted line (black dotted vertical line). For two-component fits, the central frequency of the line is set to the mean of the two components' central frequencies. The brown vertical dotted lines delimit the velocity range within which we computed the moments. For the two-component fits, the range spans from the low-velocity side of the blue-shifted component to the high-velocity side of the red-shifted one. The source ID is reported in the top left corner. Bottom panels: residuals when subtracting the total model from the data. The grey shaded region shows the rms per channel, indicating the 1σ range. From D'Amato et al. (2020a). 46

3.3 FRII host galaxy ($a0$) line velocity map (moment 1), with respect to the line central frequency of the fit marked by the vertical black dotted line in Fig. 3.2). North is up and east to the left. The black open ellipse is the restoring beam. The VLA contours, drawn as in Fig. 3.1, are shown in black. From D'Amato et al. (2020a). 48

3.4 Velocity distribution of all the known members of the overdensity with respect to the mean redshift z=1.694, color coded by the discovery instrument. The velocity bins are 30 km/s wide, equal to the mean uncertainty of the sources' redshift. $a0$ and $l1$ correspond to the same source, the FRII galaxy. From D'Amato et al. (2020a). 50

3.5 *Left*: Evolution of the most massive halo mass as a function of redshift, color-coded by the final cluster mass, as labeled in the figure. Results are based on WMAP1 (solid) and WMAP7 (dotted) simulations. The lines and error bars indicate the medians and 1σ error. The horizontal dashed line marks the final mass threshold (10^{14} $M_\odot$) above which a structure is considered a cluster. *Right*: Correlation between the galaxy overdensity δ_{gal} at $z = 2$, and the $z = 0$ descendant cluster mass $M_{z=0}$, calculated for a volume of 15 Mpc^3 and considering galaxies with SFR > 1 $M_\odot$/yr. In both panels the green dot marks the position of our object. Adapted from Chiang, Overzier & Gebhardt (2013). 52

3.6 ALMA continuum emission at 92.04 GHz, blanked at the 3σ level. The black contours indicate the VLA contours at 1.4 GHz, starting from a $\sim 3\sigma$ flux density threshold and increasing with a $\sqrt{3}$ geometric progression (see Sect. 2.1). Blue (dashed) and red (solid) contours indicate the 2σ hard and soft X-ray diffuse emission, respectively. The four major components of such emission are labeled in black (A–D; see § 2.2.1). The positions of five of the sources discovered by MUSE ($m1 - m5$) are indicated by the green circles (a sixth source is located outside the image, $\sim$45 arcsec north-east from the FRII core). The positions of the proto-cluster members discovered by ALMA ($a1 - a3$) are marked by the magenta boxes. The Eastern and Western lobes are labeled as E-lobe and W-lobe, respectively. The light blue circle indicates the $z = 6.3$ QSO (at the center of the J1030 field). The solid black line at the bottom-left corner indicates the angular and physical scale, while the dashed ellipse at the bottom-right corner is the restoring beam of the ALMA image. Adapted from D'Amato et al. (2021). 54

3.7 SED fitting of the FRII host galaxy. Photometric points are marked by the filled red circles, while the total fitting model is indicated by the solid black line. In both panels the ALMA point is not included during the fitting and is marked by the filled cyan circle. *Left*: The model includes three components: stellar emission (indicated by the red dotted line), the reprocessed emission of the dusty torus surrounding the AGN (blue dashed line), and emission by the cold dust of the host galaxy, heated by starburst activity (green dashed line). *Right:* same as the left panel, except for the cold dust template that has been substituted by a gray-body model with $\beta = 2$. From D'Amato et al. (2021). 55

4.1 Cut-out of the 1.5 GHz JVLA image centered on the HzRG at $z = 1.7$. The old VLA contours at 1.4 GHz (Petric et al., 2003; Nanni et al., 2018) are reported in orange, starting from a 3σ threshold and increasing with a $\sqrt{3}$ geometric progression. Blue and red contours are the $\sim 2\sigma$ hard and soft X-ray diffuse emission, respectively. The four major components of such emission are labeled in black (A, B C and D). The positions of five of proto-cluster members discovered by MUSE ($m1 - m5$) are indicated by the green circles (a sixth source is located outside the cut-out, ~45 arcsec North-East from the FRII galaxy core). The positions of the proto-cluster members discovered by ALMA ($a1 - a3$) are marked by the magenta boxes. We note that $a2$ and $a3$ are detected in the JVLA image (they will be discussed in Chapter 5). The Eastern and Western lobes are labeled as E-lobe and W-lobe, respectively. The main morphological features of the lobes are also reported, indicated by the black arrows. The light blue circle indicates the z=6.3 QSO at the center of the J1030 field, which is detected for the first time in the radio-band (see Chapter 5 for a more in-depth discussion of this source). The solid black line at the bottom-left corner indicates the angular and physical scale, while the dashed ellipse at the bottom-right corner is the restoring beam of the JVLA image. . . . 61

4.2 Fractional polarization images of the FRII HzRG in the two 42 MHz wide IFs: IF1 (1365 MHz, top panel) and IF2 (1435 MHz, bottom panel). The images are blanked at a 3σ threshold. The black contours indicate the total intensity emission from the full-band JVLA image, starting from a $\sim 3\sigma$ threshold and increasing with a $\sqrt{3}$ geometric progression. The magenta dashes indicate the orientation of the magnetic field. The dashed ellipse in the bottom left corner represents the restoring beam. The solid black lines in the bottom of the two panels indicate the angular and physical scales. For clarity, in the IF1 image we indicated the Eastern and Western lobes as E-lobe and W-lobe, respectively, and specify that the E-jet is the approaching one. From D'Amato et al. (2021). 63

5.1 *Left*: 1.5 GHz JVLA image of the J1030 field. The field considered here has a diameter of 30', and corresponds to the region where the source catalogue has been extracted. The *HPBW* for the JVLA at 1.5 GHz is ~27' and is indicated by the green dashed circle. The region covered by the *Chandra* mosaic is marked by the solid cyan line. *Right*: Visibility area of the JVLA field (black solid line). The median noise is 3.5 μJy/b, and is indicated by the red vertical dashed line. 67

5.2 Sky coverage vs. sensitivity limit (5σ) for available radio survey at cm wavelengths, color-coded by the instrument as in the legend. The flux densities refer to 1.4 GHz; the surveys at other frequencies have been rescaled to 1.4 GHz assuming a radio spectral index of 0.7. The large red square indicates the J1030 field presented in this work. The reported surveys are as follows: LBDS (Windhorst, van Heerde & Katgert, 1984), NEP (VLA, Kollgaard et al., 1994), FIRST (White et al., 1997), MF (Gruppioni et al., 1997), NVSS (Condon et al., 1998), PDF (Hopkins et al., 1998), ELAIS–S (Gruppioni et al., 1999), ELAIS–N (Ciliegi et al., 1999), SUMSS (Bock, Large & Sadler, 1999), ATESP (Prandoni et al., 2000), BOOTES (de Vries et al., 2002), VVDS (Bondi et al., 2003), FLS (VLA, Condon et al., 2003), FLS (WSRT, Morganti et al., 2004), 13h (Seymour, McHardy & Gunn, 2004), HDFN (Huynh et al., 2005), LHEX (Oyabu et al., 2005), SXDF (Simpson et al., 2006), ELAIS–N2, LH–XMM and HDFN (Biggs & Ivison, 2006), SSA13 (Fomalont et al., 2006), ATLAS (Norris et al., 2006), COSMOS (Schinnerer et al., 2007), AEGIS (Ivison et al., 2007), SWIRE (Owen & Morrison, 2008), LH (VLA, Ibar et al., 2009), NEP (WSRT, White et al., 2010), GOODS–N (Morrison et al., 2010), SDSS–82 (Hodge et al., 2011), JVLA–SWIRE (Condon et al., 2012), SEP (White et al., 2012), CDFS (Miller et al., 2013), COSMOS–S (Smolčić et al., 2017a), LH (WSRT, Prandoni et al., 2018), RACS–DR1 (McConnell et al., 2020), MIGHTEE–ES (Heywood et al., 2021), EMU–Pilot (Norris et al., 2021), VLASS (ongoing, Lacy et al., 2016), eMERGE–DR1 (ongoing, Muxlow et al., 2020), SPT (ongoing, PI: N. Tothill), XXL–S (ongoing as part of SPT, PI: V. Smolčić). . 68

5.3 *Left*:Reliability function of the catalogue (black solid line) with the 1-σ uncertainty (grey shades) as a function of the S/N. The red vertical dashed line marks the detection threshold (S/N=5), corresponding to a reliability value of 90%. *Right:* Mean detection fraction of the simulated point-like sources (black solid line) with the 1-σ uncertainty (grey shades) as a function of the S/N. The red vertical dashed line marks the detection threshold (S/N=5). The blue dashed line indicates the S/N completeness function (see text for more details). 69

5.4 *Left*: Ratio between total (S_T) and peak (S_P) flux density as a function of S/N. The red vertical dashed line marks the detection threshold (S/N=5). The black solid line divides resolved sources (above the line, blue points) from unresolved sources (below the line, black points). *Right:* Deconvolved source size as a function of total flux density. Unresolved source have deconvolved size set to 0. The red circles mark the median deconvolved size in bins of S_T with 1σ error indicated by the grey bars. The red dashed line indicates the maximum deconvolved size ($\Theta_{\rm max}$, Eq. 5.8), the green dash-dotted line represents the median size relation of Windhorst, Mathis & Neuschaefer (1990) ($\Theta_{\rm med}$, Eq. 5.11), calculated assuming a flux-dependent exponent m (Eq. 5.12). The solid black line is the minimum deconvolved size ($\Theta_{\rm min}$, Eq. 5.9). 74
5.5 Cumulative size distribution of our source sample (black solid line) in six bins of flux density. The red dashed line represents the minimum deconvolved size (Eq. 5.9), while the green and blue dash-dotted lines represent the source size cumulative distribution function described by Eq. 5.10, setting $q = 0.62$ and $q = 1$ respectively. All lines are calculated at the geometric mean of each flux bin. 75
5.6 Normalized differential source counts derived from the J1030 radio source catalogue (blue squares bordered in black). The counts have been rescaled from 1.5 GHz to 1.4 GHz by assuming $\alpha = 0.7$. Vertical bars represent the squared sum of Poissonian errors (computed following Regener 1951) and systematic errors on the normalized counts. Also shown for comparison are the counts derived from a number of wide-field (>> 1 deg^2) surveys. All the surveys shown in this plot are taken at 1.4 GHz or at frequencies not far from 1.4 GHz, to minimize systematic errors introduced when rescaling the counts to 1.4 GHz. Unless stated differently, the rescaling has been done by assuming $\alpha = 0.7$, as for the J1030 survey. The surveys are listed in the legend and in the text. The yellow and light blue shaded areas illustrate the predicted cosmic variance effects for survey coverages of 5 and 10 sq deg respectively. They have been obtained by splitting the S3-SEX simulation of Wilman et al. (2008) (covering 1×200 deg^2, see black line) in forty 5-deg^2 and twenty 10-deg^2 fields respectively. The 25 deg^2 medium tier of the more recent T-RECS simulations (Bonaldi et al. 2019) is represented by the violet shaded area. Finally, the counts derived from the Mancuso et al. (2017) radio source evolutionary model are indicated by the light green solid line. 78

5.7 Rest-frame optical luminosity at 4400 Å vs. rest-frame radio luminosity at 5 GHz for known quasars at z~6 (Bañados et al. 2015 and references therein; Bañados et al. 2018; Liu et al. 2021; Sbarrato et al. 2021). Black points mark radio detected sources, while blue points indicate radio undetected ones, for which 3σ upper limits are reported. The red point marks the position of the SDSS J1030+0524 QSO, based on our JVLA detection. The black dashed line indicates the radio-loudness value $R_O = 10$, set as a threshold between radio-quiet and radio-loud AGN (Jiang et al., 2007). The inset shows the JVLA emission, with cyan contours starting at the 3σ level and increasing with a $\sqrt{3}$ geometric progression. The black bar indicates the angular scale of the image. 80

5.8 Multi-λ cutouts (15”x15” each) centered on source ID 24071 (cyan circle). See Table 2.1 for references. 82

5.9 Redshift distribution of the 243 X-ray sources (black solid line) used for our radio/X-ray analysis, in redshift bins of 0.35. The distribution of the 123 sources having spectroscopic classification (and redshift) is shown in red. 83

5.10 *Left*: X-ray intrinsic luminosity in the 2–10 keV band vs. rest -frame 1.4 GHz radio luminosity for our sample. NL-AGN, BL-AGN, ETG and ELG are indicated by blue, red, orange and green symbols, respectively. The light-grey symbols mark the sources without a spectroscopic classification. Circles mark radio-detected sources, while triangles represent 3σ upper limits for the undetected ones. Typical uncertainties on the radio (X-ray) luminosity is indicated by the vertical (horizontal) errorbar in the bottom-right corner. The solid black line is the correlation presented in this work (slope ~ 0.8; see text for more details). The magenta line is the Panessa et al. (2015) correlation found for local Syefert galaxies (slope ~ 1.1), while the blue line is the relation for $0 \lesssim z \lesssim 1.3$ SFG (Mineo et al., 2014). The green line is the relation found for local radio-loud AGN by Canosa et al. (1999). The solid part of the lines represent the X-ray luminosity range in which they have been derived; the dashed part of the lines represent extrapolations to the entire luminosity range covered of our sample. Notable sources, i.e. the $z = 6.3$ QSO and the $z = 1.7$ FRII galaxy, are labeled in the figure. *Right:* Same as in left panel, but sources are color-coded based on their redshift (right color-bar): 123 sources have spectroscopic redshifts, the other 120 source have photometric redshift. . 85

5.11 *Left*: Radio-loudness distribution of the radio-detected X-ray sources, color-coded by their spectral classification. The $R_X = 3.5$ threshold separating RQ from RL AGN (Lambrides et al., 2020) is indicated by the red dashed vertical line. The radio-loudest source is the FRII galaxy at $z = 1.7$. *Right:* Radio-loudness of the radio-detected X-ray sources as a function of 1.4 GHz rest-frame luminosity, color-coded by object class. . 86

List of Tables

2.1 Photometric (*Top*) and spectroscopic (*Bottom*) datasets available for the J1030 field. From left to right: Band, instrument or survey, 5σ sensitivity. 32

2.2 (1) Source ID. Sources discovered by MUSE are labeled as m, while sources discovered by LUCI are labeled by l. The $l1$ source correspond to the FRII RG. (2) Source right ascension (RA) and (3) declination (DEC). (4) Spectroscopic redshift of the source. 35

3.1 (1) Source ID. (2) Source right ascension (RA) and (3) declination (DEC). (4) HST H-band (typical 1-σ uncertainty: 0.02) and (5) $z-H$ color index (typical 1-σ uncertainty: 0.25). We note that $a3$ appears as a blend of two galaxies at the high spatial resolution of the HST images (see Fig. 3.1, right panel). In this case we report the magnitude and color index of the source corresponding to the bulk of CO emission (that to the East) and in parentheses the values of the other source (that to the West). 44

3.2 Summary of the fit results and molecular masses. (1) ID of the source. (2) Redshift of the line, set equal to the mean of the blue- and red-shifted components for the two-component fits. (3) and (4) *FWHM* of the red- and blue-shifted component, respectively. (5) and (6) Flux density peak of the red- and blue-shifted components, respectively. (7) Integrated flux of the line. (8) Line luminosity. (9) Molecular gas mass. For $a1$ and $a2$ we performed a single-component fit. 47

3.3 Photometric data-points used to perform the SED fitting. (1) Observing wavelength. (2) Observed flux density. (3) Observing instrument. (4) Reference publications, where we specify whether the data have been re-analyzed. 53

5.1 The first ten entries of the radio-source catalogue. Columns are described in the text (§ 5.2.1). A complete version of the catalogue will be available at the CDS site. 72

5.2 1.5 GHz source counts as derived from our survey. (1) Flux density interval. (2) Flux density geometric mean. (3) Number of detected sources. (4) Differential counts normalized to a non evolving Euclidean model. (5) and (6) Poissonian errors on the normalized counts. (7) and (8) Systematic errors, accounting for different modeling of resolution and Eddington bias corrections (see § 5.4.1 and 5.4.2 for more details). 77

5.3 Optical/IR photometry of $a2$. (1) Observed band. (2) AB magnitude. The upper limits are given at the 5σ level. (3) Observing instrument. (4) Reference of the measurements. 81